Monthly Notices
of the
ROYAL ASTRONOMICAL SOCIETY

MNRAS **476,** 5127–5188 (2018)
Advance Access publication 2018 February 24

doi:10.1093/mnras/sty514

Baryonic distributions in galaxy dark matter haloes – II. Final results

Emily E. Richards,[1★] L. van Zee,[1★] K. L. Barnes,[1] S. Staudaher,[2] D. A. Dale,[2]
T. T. Braun,[1] D. C. Wavle,[1] J. J. Dalcanton,[3] J. S. Bullock[4] and R. Chandar[5]

[1] *Indiana University, 727 East 3rd Street, Swain West 318, Bloomington, IN 47405, USA*
[2] *University of Wyoming, 1000 E. University, Dept 3905, Laramie, WY 82071, USA*
[3] *University of Washington, Box 351580, U.W., Seattle, WA 98195, USA*
[4] *University of California, Irvine, Department of Physics & Astronomy, 4129 Frederick Reines Hall, Irvine, CA 92697, USA*
[5] *University of Toledo, 2801 West Bancroft Street, Toledo, OH 43606, USA*

Accepted 2018 February 22. Received 2018 February 20; in original form 2017 February 23

ABSTRACT

Re-creating the observed diversity in the organization of baryonic mass within dark matter haloes represents a key challenge for galaxy formation models. To address the growth of galaxy discs in dark matter haloes, we have constrained the distribution of baryonic and non-baryonic matter in a statistically representative sample of 44 nearby galaxies defined from the Extended Disk Galaxy Exploration Science (EDGES) Survey. The gravitational potentials of each galaxy are traced using rotation curves derived from new and archival radio synthesis observations of neutral hydrogen (H I). The measured rotation curves are decomposed into baryonic and dark matter halo components using 3.6 μm images for the stellar content, the H I observations for the atomic gas component, and, when available, CO data from the literature for the molecular gas component. The H I kinematics are supplemented with optical integral field spectroscopic (IFS) observations to measure the central ionized gas kinematics in 26 galaxies, including 13 galaxies that are presented for the first time in this paper. Distributions of baryonic-to-total mass ratios are determined from the rotation curve decompositions under different assumptions about the contribution of the stellar component and are compared to global and radial properties of the dominant stellar populations extracted from optical and near-infrared photometry. Galaxies are grouped into clusters of similar baryonic-to-total mass distributions to examine whether they also exhibit similar star and gas properties. The radial distribution of baryonic-to-total mass in a galaxy does not appear to correlate with any characteristics of its star formation history.

Key words: galaxies: kinematics and dynamics.

1 INTRODUCTION

The ability of simulations to reproduce observed structural and dynamical scaling relations is a crucial test of galaxy formation models. Yet, only recently have state-of-the-art hydrodynamical simulations using Λ cold dark matter (CDM) cosmology been able to reproduce and explain one of the most fundamental empirical relations between baryonic mass and disc circular rotation velocity, or Baryonic Tully–Fisher Relation (BTFR; McGaugh et al. 2000). Interpretation of the BTFR in the context of galaxy formation in ΛCDM cosmology has been challenging in large part due to the translation from virial mass to baryonic mass and the low galaxy formation efficiencies it implies. The small fraction of available baryons that end up in galaxies has often been explained through the effects of feedback from stellar and supermassive black hole evolution, but these chaotic mechanisms are expected to create significant scatter at odds with the observed tightness in the BTFR (e.g. McGaugh 2012; Lelli, McGaugh & Schombert 2016b).

More recently, it has been demonstrated that the BTFR as well as the anticorrelation between the acceleration due to baryons and ratio of total-to-baryonic mass at a given radius, or mass discrepancy acceleration relation (MDAR; McGaugh 2004), can be reproduced in simulations that match other observed scaling relations, specifically the number and sizes of galaxies as a function of stellar mass (e.g. Di Cintio & Lelli 2016; Ferrero et al. 2017; Sales et al. 2017). Given the importance of the size–mass relation in explaining these dynamical relations in a cosmological context, exploring potential correlations between the distribution of mass and properties of the gas and stars in galaxies could provide insight into how baryons settle in dark matter haloes. We have undertaken a project to investigate whether galaxies with similar distributions of mass have

---

★ E-mail: er7@indiana.edu (EER); lvanzee@indiana.edu (LvZ)

Published by Oxford University Press on behalf of the Royal Astronomical Society

similar star formation histories, as probed through global and radial characteristics of their stellar and gas content.

We employ the method of rotation curve decomposition to constrain the radial distributions of baryonic and non-baryonic mass components and utilize a statistically representative sample of 44 nearby galaxies defined from the Extended Disk Galaxy Exploration Science (EDGES) Survey (van Zee et al. 2012). Data for the EDGES Survey includes deep 3.6 µm observations from the *Spitzer Space Telescope* of 92 galaxies spanning a wide range of morphology, luminosity, and environment. Galaxies were selected to have distances between 2–20 Mpc and include the Ursa Major Cluster, but exclude the Virgo Cluster due to source confusion and the complex dynamics of galaxies in that high-density region. We have defined a kinematic sample from the EDGES Survey that includes all galaxies that have intermediate inclination angles (between 30° and 68°) estimated from optical axial ratios so that both accurate rotation curves and surface density profiles may be determined.

Detailed descriptions of the data acquisition and analysis for 17 of the 44 galaxies in the complete EDGES kinematic sample are provided in Richards et al. (2015) and Richards et al. (2016). This paper presents results for the remaining 27 galaxies and final analysis of the complete EDGES kinematic sample. It is organized as follows. A brief summary of the data products used in the analysis and presentation of new observations is provided in Section 2. Rotation curve decompositions for the complete EDGES kinematic sample and analyses of the final results are described in Sections 3 and 4, respectively. Section 5 summarizes and discusses the synthesized results of the analysis. Notes on individual galaxies with brief summaries of existing data and observational summary figures can be found in Appendix A. Tables presenting observed and corrected properties are shown in Appendix B and rotation curves can be found in Appendix C. Position–velocity diagrams and rotation curve decompositions for the complete kinematic sample are presented in Appendixes D and E.

2 SUMMARY OF DATA PRODUCTS

New (12) and archival (32) H I synthesis observations from the Very Large Array (VLA)[1] and the Westerbork Synthesis Radio Telescope (WSRT)[2] are used to trace the neutral gas kinematics and gas mass surface density distributions of 44 galaxies in the complete EDGES kinematic sample. For 26 of the galaxies, the H I kinematics are supplemented with integral field spectroscopic (IFS) observations from SparsePak on the WIYN 3.5 m telescope to constrain the central ionized gas kinematics. Archival CO data are used to probe the molecular gas mass surface density component in 20 of the galaxies. Near-infrared observations at 3.6 µm from the *Spitzer Space Telescope* constrain the stellar distributions, while optical broad-band B and R and narrow-band H α observations from the WIYN 0.9 m telescope reveal properties of the dominant stellar populations. Acquisition and processing of these data products is briefly summarized below.

2.1 H I synthesis data

New H I synthesis observations have been acquired for three galaxies, NGC 4068, NGC 4096, and NGC 4102, in 2016 February and April with the VLA in C configuration (Figs A13, A15, and A16). The new VLA data for NGC 4096 had an initial frequency resolution of 7.8125 kHz channel^{-1} (1.65 km s^{-1} channel^{-1}) with 1024 channels. NGC 4068 and NGC 4102 were observed in the same field using a set-up that provided an initial velocity resolution of ∼0.825 km s^{-1} with 2048 channels. These observations were obtained with a higher velocity resolution to enable a science case unrelated to this paper.

All new and archival VLA data were loaded into AIPS[3] and processed following the methods outlined in Richards et al. (2016) with the exception of one data set that was processed in CASA (McMullin et al. 2007). Solar RFI was flagged on all channels simultaneously, but was mostly not a problem. Three data cubes were created for each galaxy with different robust weighting parameters for varying sensitivity and spatial resolution, and a channel averaging of three (six for NGC 4068/4102) for a resulting velocity resolution of ∼5 km s^{-1} channel^{-1}. Separate data cubes were created for NGC 4068 and NGC 4102 centred on their H I emission frequencies and spatial locations.

H I data for 21 of the 27 galaxies have been previously published, including six galaxies that are part of the Westerbork Survey of H I in Spiral Galaxies (WHISP; van der Hulst, van Albada & Sancisi 2001). Processed WSRT data products were kindly provided by Marc Verheijen (IC 0749 and UGC 06983; Verheijen & Sancisi 2001) and Adrick Broeils (UGC 06955 and UGC 08320; Broeils 1992) for an additional four galaxies. Processed data were also used for UGC 06900 (LITTLE THINGS; Hunter et al. 2012) and NGC 7793 (THINGS; Walter et al. 2008). H I data sources and synthesis imaging parameters for the data cubes used to derive the rotation curves for these 27 galaxies are summarized in Table B4. Finally, H I moment maps for the 27 galaxies are presented in Appendix A (Figs A1–A26).

2.2 Ionized gas kinematics

New SparsePak-ionized gas IFS observations for 13 galaxies were obtained on 2014 April, 2015 December, and 2016 April, using the same observational set-up as described in detail in Richards et al. (2016). Three exposures were taken for each of the three pointings used in the dither pattern to spatially fill in gaps between fibres. NGC 4151 required three separate pointings to cover the full extent of the central region on the sky, while NGC 4068 and NGC 4102 required two separate pointings. Observations of blank sky were also taken to remove sky line contamination more accurately, as all of the galaxies are much more extended than the SparsePak field of view (see Fig. 1). The SparsePak data were processed using standard tasks in the HYDRA package within IRAF[4] following the procedures outlined in Richards et al. (2016). Individual images were sky subtracted using a separate sky pointing scaled to the strength of the 6577 Å sky line. Although the nights were non-photometric, a flux calibration using observations of spectrophotometric standards from Oke (1990) was applied to remove instrumental signatures.

---

[1] The VLA is operated by the National Radio Astronomy Observatory, which is a facility of the National Science Foundation operated under cooperative agreement by Associated Universities, Inc.

[2] The WSRT is operated by the ASTRON (Netherlands Institute for Radio Astronomy) with support from the Netherlands Foundation for Scientific Research (NWO).

[3] The Astronomical Image Processing System (AIPS) has been developed by the NRAO.

[4] IRAF is distributed by NOAO, which is operated by the Association of Universities for Research in Astronomy, Inc., under cooperative agreement with the National Science Foundation.

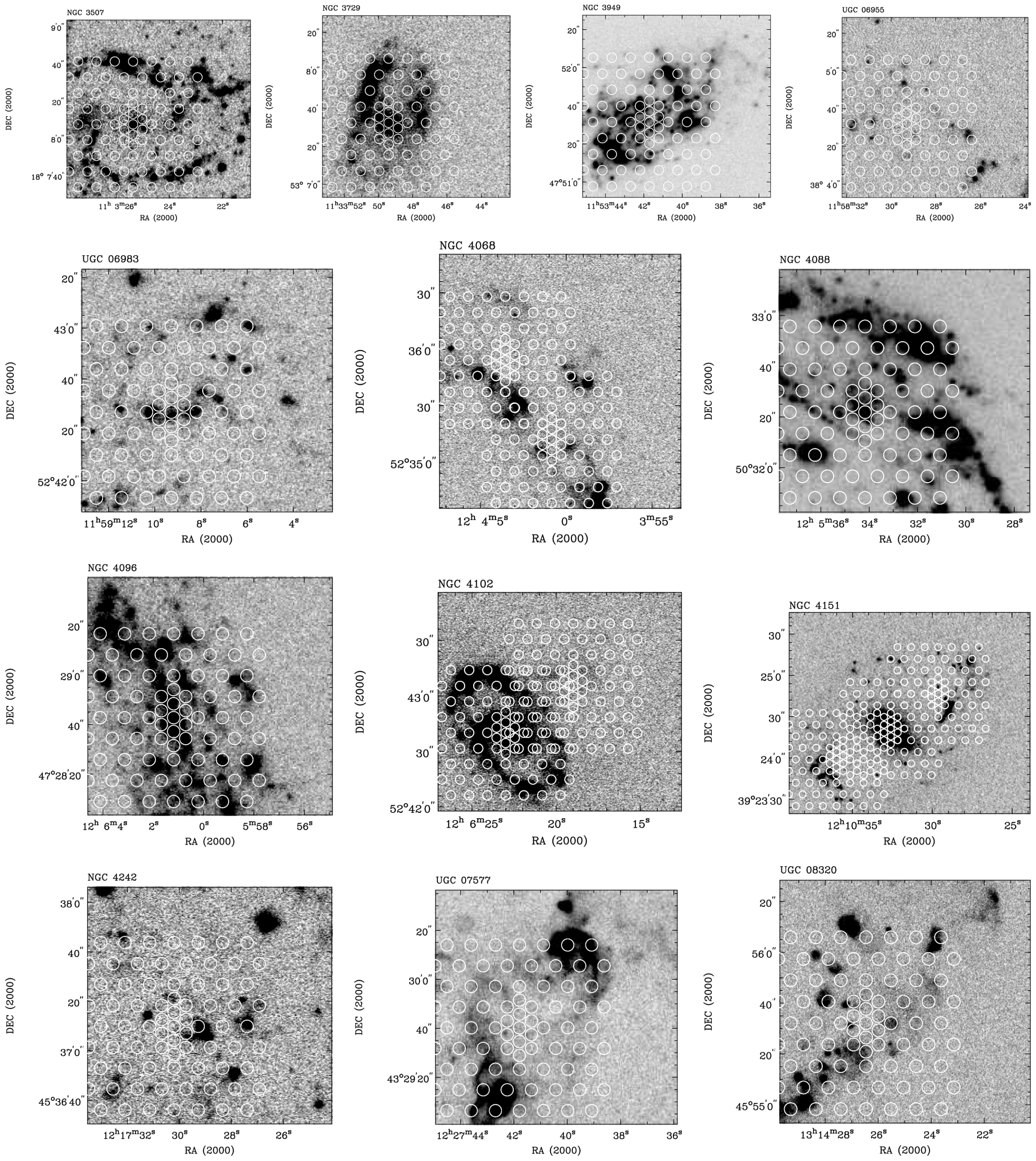

Figure 1. SparsePak fibre footprints for one pointing (dithers not shown) overlaid on the continuum-subtracted narrow-band H α images. Fibres designated as 'sky' are just outside the field of view.

Calibrated, sky-subtracted spectra were cross-correlated with a template emission-line spectrum to measure the luminosity-weighted mean recessional velocity at every position using the IRAF task FXCOR. Velocity values from the cross-correlation were placed into a grid mapping the position of the fibres and were interpolated to fill in gaps (Fig. 2).

2.3 Optical and near-infrared photometry

Results derived from the photometric analysis of the 3.6 μm and optical data are given in Tables B1–B3. Radial and integrated values were determined from aperture photometry using concentric, con-eccentric ellipses using routines in the

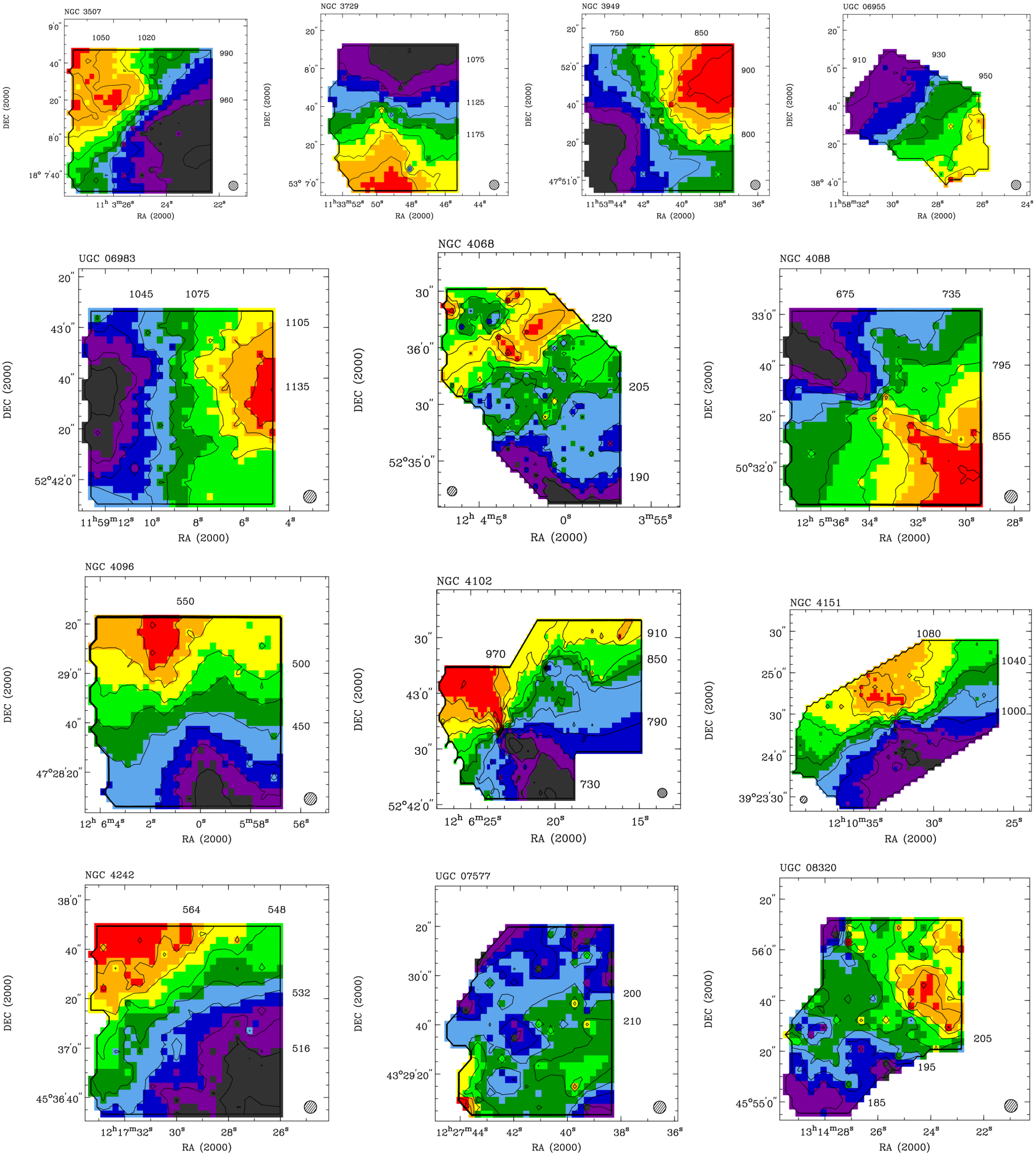
NGC 3507
NGC 3729
NGC 3949
UGC 06955
UGC 06983
NGC 4068
NGC 4088
NGC 4096
NGC 4102
NGC 4151
NGC 4242
UGC 07577
UGC 08320

Figure 2. Ionized gas velocity fields from SparsePak IFS observations.

GALPHOT[5] package for IRAF. The 3.6 μm imaging observations were acquired from the Infrared Array Camera (IRAC) in 2011–2013 as part of *Spitzer's* Cycle 8, while optical imaging observations were taken in 2013–2015 using the Half Degree Imager and S2KB imager on the WIYN 0.9 m telescope. Further details about the photometric data acquisition and analysis are provided in Richards et al. (2016).

2.4 Derivation of neutral and ionized gas rotation curves

Ionized gas velocity fields from SparsePak observations and H I velocity fields from both new and archival H I observations were

---

[5] GALPHOT is a collection of scripts in the IRAF STSDAS environment first developed by Freudling and Salzer. The current version has been further enhanced by members of the Cornell Extragalactic Group and is maintained by Haynes.

analysed using standard tools distributed as part of the GIPSY software package (van der Hulst et al. 1992). Rotation curves for each galaxy were derived by fitting a series of concentric tilted rings to the H I and SparsePak-ionized gas intensity-weighted velocity fields separately using the GIPSY task ROTCUR. The H I velocity fields were sampled using two rings per beam to observe more easily the trend in the bulk circular motion. While common practice, this means that individual rotation curve points are not truly independent and caution should be used when evaluating statistical goodness of fit metrics. Only one ring per resolution element was fit to the Hα velocity fields. Error estimates for the derived H I circular rotational velocities include contributions from non-circular thermal gas motions, asymmetry, and inclination angle uncertainties, while the ionized gas error estimates include only inclination angle uncertainty. The radial extent of the ionized gas velocity field in most of the galaxies was too small to yield meaningful separate approaching and receding rotation curves to measure asymmetry. Non-circular motions are likely the dominant source of uncertainty in the ionized gas rotational velocities and strongly influence the derived circular rotational velocities, as is evident in the shapes of many of the ionized gas rotation curves. Rather than attempt to quantify the affect, we simply utilize the ionized gas rotation curves as a means to visually fill in velocity information for the central regions of galaxies that have inadequate H I emission. Details about the creation of the intensity-weighted velocity fields, extraction of the rotation curves, and error estimates are provided in Richards et al. (2015) and Richards et al. (2016). While significant progress has been made in techniques utilizing the full three-dimensional data cube to derive rotation curves (e.g. Di Teodoro & Fraternali 2015; Józsa et al. 2007), archival data cubes were not available for some of the galaxies in the kinematic sample. Therefore, the two-dimensional intensity-weighted velocity fields were used in order to derive rotation curves in a consistent and systematic manner. Rotation curves were overlaid on position-velocity cuts along the major axis to confirm that the derived circular rotational velocities follow the H I emission (Fig. D1).

Rotation curves derived for the remaining galaxies in the complete EDGES kinematic sample are presented in Fig. C1 and Table C1. Of the 27 remaining galaxies, rotation curves could only be derived for 23 sources. The dwarf galaxy UGC 07577 has ionized gas motions that are dominated by turbulence, and its small maximum H I velocity ($\sim$20 km s^{-1}) and proximity to a larger nearby galaxy suggest UGC 07577 may not be in dynamical equilibrium (Hunter et al. 1998). Therefore, it is excluded from further analysis. The ionized gas kinematics in NGC 4068 and UGC 08320 are also dominated by non-circular turbulent motions and were not included with the successfully derived H I rotation curve. The complex kinematics in NGC 3718 and NGC 4485 hint that their H I is not in dynamical equilibrium, possibly due to interactions with nearby companions. Rotation curves could not be fit successfully to their velocity fields. Finally, the inclination angle of the H I disc in NGC 4214 was too face-on, so the rotation curve could not be constrained accurately.

Deviation between the ionized and neutral gas rotation curves at small radii are largely driven by non-circular motions caused by bars and/or other nuclear activity, as well as beam smearing resolution effects in the H I data. No attempt has been made to correct for these resolution effects. The presence of non-circular motions indicates that the gas is not probing the underlying gravitational potential. Therefore, more accurate modelling of these kinematics does not improve our ability to accurately constrain the distribution of mass in the affected regions.

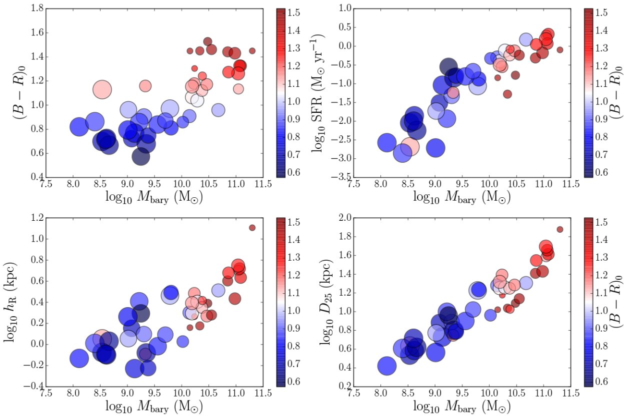

Figure 3. Properties of the galaxy stellar populations as a function of the total mass in baryons: $M_{\rm bary} = M_{\rm H\,I} + M_{\rm H_2} + M_{\rm star}$. The stellar mass is computed assuming M/L = 0.5. Point sizes are scaled to the morphological T-type, where larger points are equivalent to dwarf and late-type spiral galaxies and smaller points represent early-type spiral and S0 galaxies. Point colours are assigned based on the optical $(B-R)_0$ colours. Top left: $(B-R)_0$ colour versus $M_{\rm bary}$. Top right: SFR versus $M_{\rm bary}$. Bottom left: exponential disc scale length measured at 3.6 μm versus $M_{\rm bary}$. Bottom right: size of the optical disc measured at B-band surface magnitude = 25 mag arcsec^{-2} versus $M_{\rm bary}$.

As described in Richards et al. (2016), these kinematic uncertainties are of greatest concern under a maximum disc/bulge assumption where the stellar disc/bulge model circular rotational velocities are being scaled to contribute maximally to the inner rotation curve. It should be noted, however, that an over- or underestimate of the true circular rotational velocities will still result in incorrect baryon-to-total mass ratios using any M/L estimate. Therefore, we do not rely on or base the subsequent analysis on results derived in these inner regions. All comparison of features in the mass distribution of galaxies focus on regions beyond one disc scale length.

3 RESULTS FROM THE COMPLETE EDGES KINEMATIC SAMPLE

With rotation curves derived for all rotationally supported galaxies, we shift focus to the complete EDGES kinematic sample, including results from 17 galaxies presented in Richards et al. (2015) and Richards et al. (2016). Properties of the baryonic components of the full EDGES kinematic sample are displayed in Fig. 3. These plots exhibit well-known scaling relations that exist between the total baryonic mass (gas + stars) and the sizes and star formation histories of the stellar populations. For example, the top plots demonstrate that the least massive galaxies tend to be bluer with smaller overall star formation rates (SFRs), while the most massive galaxies are red with large total SFRs. The size of the points also reveals that the bluer, less massive galaxies typically have later morphological T-types indicating they are late-type spiral or dwarf galaxies, while the red, more massive galaxies are typically early-type spiral or S0 galaxies. The bottom plots show that more massive galaxies have larger stellar discs with longer exponential disc scale lengths.

Fig. 3 demonstrates well-known relations between global baryon characteristics of galaxies. We take this analysis one step further by investigating whether galaxies with similar distributions of mass have similar gas and star properties.

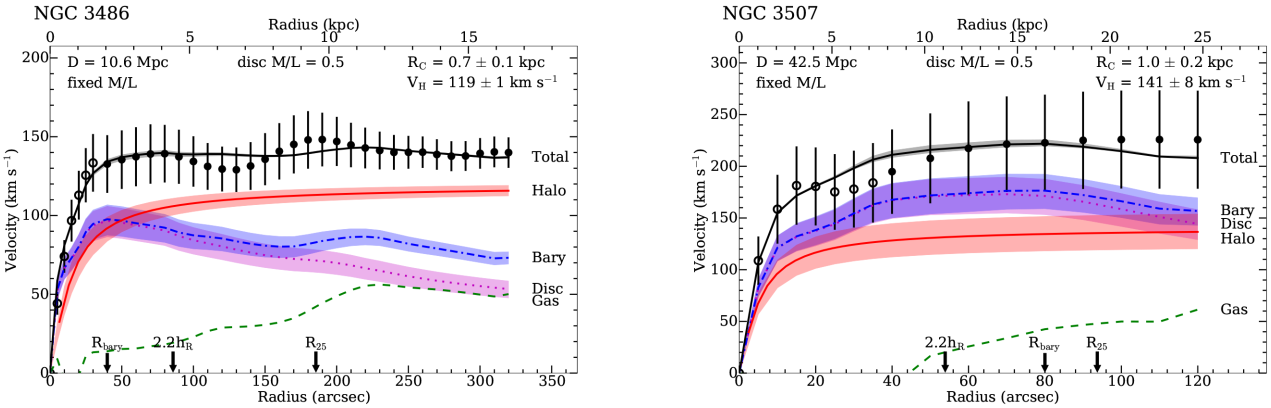

Figure 4. Rotation curve decompositions assuming a fixed stellar disc/bulge M/L = 0.5 ± 0.1 for NGC 3486 and NGC 3507 (see Fig. E1 for the remaining galaxies). The total gas (dashed green line), stellar bulge (dotted–dashed cyan line), stellar disc (dotted purple line), and dark matter halo model (solid red line) components are added in quadrature to achieve the best overall fit (solid black line) to the observed rotation curve. Open circles represent circular rotation velocities derived from the ionized gas (SparsePak) observations and the filled circles are from the H I observations. Adding the baryonic components in quadrature without the dark matter results in the dotted–double-dashed blue line. Shaded colour bands around each line demonstrate the range of possible circular rotational velocities for that component after adding or subtracting 0.1 from the listed stellar disc/bulge M/L.

3.1 Rotation curve decomposition results

Rotation curve decomposition analysis is used to constrain the radial distribution of baryonic and non-baryonic mass. The observed rotation curves trace the total mass in the galaxies as the gas follows the gravitational potential, while mass surface density profiles of the gas and stars provide estimates of the baryonic mass components. As described in Richards et al. (2016), the distribution of atomic gas in each galaxy was measured from the integrated H I map using the GIPSY task ELLINT. CO observations from the literature were used to add in the molecular gas component in 20 sources, assuming a CO/H$_2$ conversion factor of 2×10^{20} cm^{-2} (K km s^{-1}). The atomic and molecular gas distributions were measured separately and then added together to form the total gas mass surface density profile. In general, the molecular gas distributions were confined within the central 2 arcmin of the galaxies and are not a dynamically important component relative to the stellar and atomic gas contributions (e.g. Frank et al. 2016; Lelli, McGaugh & Schombert 2016a). The total gas mass was multiplied by a factor of 1.4 to account for primordial helium. The gas contribution to the observed rotation curve was derived in the same manner detailed in Richards et al. (2016) with the GIPSY task ROTMOD, assuming circular orbits in an infinitely thin disc.

The 3.6 µm surface brightness profiles measured from ellipse photometry were utilized to constrain the distributions of the stellar component. As described in Richards et al. (2016), the model stellar rotation curve was constructed first, assuming a disc-only potential with a sech^2 vertical density distribution. A spherical bulge component was added if necessary to describe the inner kinematics. The stellar content was able to be described adequately by a disc-only stellar mass distribution in all but five galaxies, including NGC 3998 for which a bulge-only distribution was used. When necessary, a stellar bulge/disc decomposition was performed on the 3.6 µm image using DISKFIT (Spekkens & Sellwood 2007). Separate model rotation curves were derived for the disc and bulge, for which a spherical mass distribution was assumed. The stellar contribution to the total observed rotation curve was scaled by a mass-to-light ratio (M/L) assumed to be constant with radius.

Circular rotational velocities from the model stellar and gas rotation curves were summed in quadrature and subtracted from the total observed rotation curve. A spherical pseudo-isothermal dark matter halo was fit to the residuals (e.g. Ostriker & Caldwell 1979; Kent 1986). Reasonable fitting dark matter halo parameters, core radius R_C and maximum halo velocity V_H, were determined using non-linear least squares minimization. Due to the over-sampling of the H I rotation curves and systematic uncertainties inherent in rotation curve decomposition analysis, least squares minimization is used primarily as a convenience and should not be interpreted as a true statistically motivated result. Furthermore, the derivation of dark matter haloes in the context of this work is primarily intended to provide a visualization for the relative amount and distribution of non-baryonic mass necessary to describe the total mass distribution as probed by the observed rotation curve. The final analysis and results do not depend on the form or parameters of the derived dark matter haloes. The degeneracy between the scaling of the stellar component through its M/L and the dark matter halo model was broken under two different assumptions: fixed M/L at 0.5 ± 0.1 (e.g. Eskew, Zaritsky & Meidt 2012; McGaugh & Schombert 2015; Lelli, McGaugh & Schombert 2016b) and maximum disc/bulge. The fixed M/L includes a ±0.1 allowed variance to take into account distance uncertainties (see Richards et al. 2016).

Rotation curve decomposition results are shown in Figs 4 and 5 and in Appendix E (Figs E1 and E2) for all galaxies in the EDGES kinematic sample for which accurate and reliable rotation curves could be derived. Although we erred on the side of inclusion, the rotation curves for NGC 3941, NGC 4102, NGC 4151, NGC 4490, and NGC 4618 were not included in the final decomposition analysis due to large systematic uncertainties in their derived kinematics. After the exclusion of these five galaxies, and those for which rotation curves could not be derived due to turbulent motions and interactions, 34 galaxies remain to be used in the final analysis. Rotation curve decompositions assuming fixed M/L = 0.5 ± 0.1 are presented in Fig. E1 and Table 1. To demonstrate the effect of the assumed stellar M/L on the derived halo model and total fit to the observed rotation curve, the plots in Fig. E1 include decompositions using the fixed M/L ±0.1. The area between the upper and lower limits has been coloured in to visually demonstrate the range in sensitivities to the adopted M/L, which is large for stellar mass-dominated late-type spiral galaxies and minimal for dark-matter-dominated dwarf galaxies. Values for $M_\mathrm{bary}/M_\mathrm{tot}$ at $2.2h_\mathrm{R}$ and R_bary, R_trans, and the $M_\mathrm{bary}/M_\mathrm{tot}$ gradient in Table 1 include uncertainties

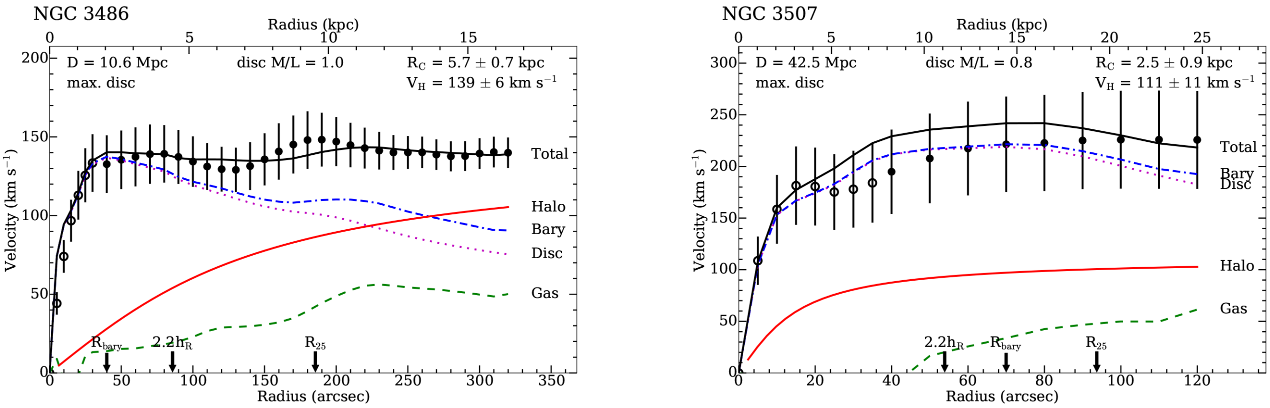

Figure 5. Rotation curve decompositions assuming the stellar disc/bulge contribute maximally to the observed inner dynamics. Lines are the same as in Fig. 4. See Fig. E2 for the remaining galaxies.

Table 1. Fixed M/L rotation curve decomposition results.

Galaxy	M/L		$M_{\rm bary}/M_{\rm tot}$[a]		$R_{\rm trans}$[b]		$M_{\rm bary}/M_{\rm tot}$ grad[c]	$R_{\rm C}$	$V_{\rm H}$
	Disc	Bulge	at $2.2h_{\rm R}$	at $R_{\rm bary}$	(kpc)	($h_{\rm R}$)	(kpc^{-1})	(kpc)	(km s^{-1})
NGC 3486	0.5	–	0.43 ± 0.08	0.54 ± 0.11	2.7 ± 2.9	1.4 ± 1.4	− 0.033 ± 0.007	0.7 ± 0.1	119 ± 1
NGC 3507	0.5	–	0.67 ± 0.13	0.63 ± 0.12	22.5 ± 5.4	4.5 ± 1.1	− 0.049 ± 0.003	1.0 ± 0.2	141 ± 8
UGC 06161	0.5	–	0.28 ± 0.03	0.29 ± 0.01	<0.9	<0.6	− 0.042 ± 0.009	2.7 ± 0.1	88 ± 1
NGC 3675	0.5	–	0.69 ± 0.12	0.78 ± 0.14	15.1 ± 3.7	3.8 ± 0.9	− 0.079 ± 0.001	0.8 ± 0.2	145 ± 5
NGC 3729	0.5	–	0.74 ± 0.13	0.87 ± 0.15	>8.5	>4.6	− 0.050 ± 0.002	2.6 ± 0.9	120 ± 19
NGC 3726	0.5	–	0.46 ± 0.09	0.47 ± 0.07	1.1 ± 0.3	0.5 ± 0.2	− 0.015 ± 0.005	1.3 ± 0.1	125 ± 2
NGC 3893	0.5	–	0.79 ± 0.13	0.82 ± 0.14	14.7 ± 4.0	4.5 ± 1.2	− 0.054 ± 0.004	3.6 ± 1.0	142 ± 9
NGC 3949	0.5	–	0.80 ± 0.15	0.80 ± 0.15	4.2 ± 1.8	3.9 ± 1.7	− 0.058 ± 0.003	1.7 ± 0.3	129 ± 8
NGC 3953	0.5	0.5	0.82 ± 0.15	0.76 ± 0.13	>22.0	>5.1	− 0.047 ± 0.004	8.8 ± 1.9	191 ± 18
UGC 06900	0.5	–	0.13 ± 0.02	0.14 ± 0.02	<0.3	<0.3	0.146 ± 0.017	0.6 ± 0.04	74 ± 2
NGC 3972	0.5	–	0.63 ± 0.11	0.56 ± 0.09	9.6 ± 1.7	3.1 ± 0.5	− 0.126 ± 0.004	15.6 ± 2.9	286 ± 42
UGC 06917	0.5	–	0.30 ± 0.05	0.28 ± 0.03	<1.8	<0.6	− 0.036 ± 0.011	3.2 ± 0.2	121 ± 2
UGC 06930	0.5	–	0.22 ± 0.04	0.23 ± 0.01	<0.8	<0.7	− 0.010 ± 0.010	1.0 ± 0.1	95 ± 4
NGC 3992	0.5	–	0.39 ± 0.08	0.43 ± 0.08	3.5 ± 1.8	0.7 ± 0.3	− 0.013 ± 0.003	2.0 ± 0.2	223 ± 5
NGC 3998	–	0.5	0.31 ± 0.06	0.57 ± 0.12	0.8 ± 0.	0.3 ± 0.1	− 0.075 ± 0.001	0.1 ± 0.1	217 ± 7
UGC 06955	0.5	–	0.19 ± 0.02	0.23 ± 0.01	<0.3	<0.1	0.037 ± 0.015	1.9 ± 0.3	77 ± 8
IC 0749	0.5	–	0.58 ± 0.11	0.54 ± 0.10	8.0 ± 3.2	3.1 ± 1.2	− 0.061 ± 0.005	2.3 ± 0.7	131 ± 17
UGC 06983	0.5	–	0.19 ± 0.03	0.28 ± 0.02	0.8 ± 0.4	0.3 ± 0.1	0.069 ± 0.015	1.9 ± 0.2	114 ± 6
NGC 4051	0.4	–	0.72 ± 0.15	0.71 ± 0.15	7.8 ± 6.3	3.4 ± 2.7	− 0.108 ± 0.003	8.3 ± 5.4	258 ± 126
NGC 4068	0.5	–	0.64 ± 0.07	0.83 ± 0.06	3.3 ± 1.3	3.9 ± 1.5	− 0.011 ± 0.016	1.3 ± 0.4	32 ± 5
NGC 4088	0.4	–	0.68 ± 0.14	0.66 ± 0.14	9.8 ± 2.0	5.3 ± 1.1	− 0.051 ± 0.002	0.5 ± 0.1	118 ± 7
NGC 4096	0.5	–	0.49 ± 0.08	0.49 ± 0.09	5.0 ± 3.6	2.0 ± 1.5	− 0.062 ± 0.003	1.4 ± 0.1	126 ± 3
NGC 4138	0.5	–	0.39 ± 0.07	0.47 ± 0.09	1.7 ± 0.9	1.2 ± 0.6	− 0.064 ± 0.001	0.8 ± 0.03	195 ± 2
NGC 4242	0.5	–	0.27 ± 0.04	0.29 ± 0.03	<0.1	<0.1	0.027 ± 0.025	0.8 ± 0.1	82 ± 7
NGC 4389	0.4	–	0.55 ± 0.13	0.54 ± 0.13	2.0 ± 0.5	2.5 ± 0.7	− 0.157 ± 0.003	2.7 ± 0.4	173 ± 20
NGC 4861	0.5	–	0.77 ± 0.09	0.76 ± 0.05	>11.6	>5.9	− 0.065 ± 0.007	5.1 ± 0.9	43 ± 4
NGC 5005	0.5	0.4	0.75 ± 0.14	0.91 ± 0.17	>11.2	>4.1	− 0.070 ± 0.001	5.5 ± 0.5	256 ± 11
NGC 5033	0.4	0.4	0.53 ± 0.11	0.96 ± 0.18	13.6 ± 4.5	2.4 ± 0.8	− 0.057 ± 0.005	5.7 ± 0.3	203 ± 3
UGC 08303	0.5	–	0.32 ± 0.03	0.30 ± 0.02	<0.4	<0.5	0.004 ± 0.008	0.6 ± 0.1	59 ± 2
UGC 08320	0.5	–	0.26 ± 0.02	0.29 ± 0.02	1.6 ± 0.1	1.5 ± 0.1	− 0.136 ± 0.003	2.6 ± 0.6	81 ± 11
NGC 5055	0.5	0.5	0.63 ± 0.11	1.14 ± 0.22	16.1 ± 4.5	3.4 ± 0.9	− 0.055 ± 0.001	3.8 ± 0.3	166 ± 1
UGC 08839	0.5	–	0.18 ± 0.02	0.24 ± 0.01	<0.5	<0.3	− 0.001 ± 0.009	2.1 ± 0.2	69 ± 2
NGC 5608	0.5	–	0.23 ± 0.03	0.22 ± 0.02	<0.4	<0.4	− 0.055 ± 0.008	0.7 ± 0.1	69 ± 2
NGC 7793	0.5	–	0.54 ± 0.10	0.45 ± 0.09	3.3 ± 0.9	2.7 ± 0.7	− 0.062 ± 0.006	2.5 ± 0.1	127 ± 4

Note. Galaxies are listed in order of increasing right ascension.

[a] Relative baryonic contribution to the total observed gravitational potential measured at 2.2 times the average disc radial scale length, $h_{\rm R}$, and the radius at which the total baryonic contribution to the observed rotation curve is maximal, $R_{\rm bary}$.

[b] The radius at which the gravitational potential transitions from baryon-dominated to dark-matter-dominated (where $M_{\rm bary}/M_{\rm tot} = 0.5$) expressed in kpc and in terms of disc radial scale lengths ($h_{\rm R}$) measured at 3.6 μm.

[c] Rate at which the baryonic-to-total mass fraction decreases.

Table 2. Maximum disc rotation curve decomposition results.

Galaxy	M/L		$M_{\rm bary}/M_{\rm tot}$[a]		$R_{\rm trans}$[b]		$M_{\rm bary}/M_{\rm tot}$ grad[c]	$R_{\rm C}$	$V_{\rm H}$
	Disc	Bulge	at $2.2h_{\rm R}$	at $R_{\rm bary}$	(kpc)	($h_{\rm R}$)	(kpc^{-1})	(kpc)	(km s^{-1})
NGC 3486	1.0	–	0.84	1.0	14.0	7.0	-0.053	5.7 ± 0.7	139 ± 6
NGC 3507	0.8	–	1.0	1.0	>24.7	>4.9	-0.055	2.5 ± 0.9	111 ± 11
UGC 06161	1.1	–	0.45	0.38	2.5	1.7	-0.079	3.8 ± 0.3	95 ± 4
NGC 3675	0.7	–	0.93	1.0	>22.2	>5.6	-0.080	22.4 ± 7.4	318 ± 78
NGC 3729	0.6	–	0.87	1.0	>8.5	>4.6	-0.048	2.5 ± 1.9	102 ± 28
NGC 3726	1.1	–	0.97	0.89	>13.7	>7.0	-0.030	7.0 ± 1.8	123 ± 17
NGC 3893	0.6	–	0.92	0.96	>21.6	>6.6	-0.057	3.7 ± 1.4	129 ± 10
NGC 3949	0.6	–	0.95	0.95	7.0	6.6	-0.061	3.3 ± 0.9	149 ± 18
NGC 3953	0.6	0.5	0.92	0.85	>22.0	>5.1	-0.041	19.9 ± 7.8	254 ± 70
UGC 06900	3.2	–	0.62	0.61	>2.9	>2.5	0.059	0.3 ± 0.03	46 ± 1
NGC 3972	0.6	–	0.74	0.66	10.8	3.5	-0.129	29.8 ± 16.9	465 ± 240
UGC 06917	1.6	–	0.80	0.62	14.1	4.8	-0.083	14.7 ± 3.5	187 ± 33
UGC 06930	1.8	–	0.73	0.57	7.1	5.6	-0.056	1.6 ± 0.6	80 ± 7
NGC 3992	0.8	–	0.62	0.67	32.1	6.1	-0.018	2.8 ± 0.3	191 ± 4
NGC 3998	–	1.4	0.85	1.0	11.7	4.8	-0.077	1.1 ± 0.7	163 ± 12
UGC 06955	3.5	–	0.72	0.62	9.8	3.8	-0.090	1.3 ± 0.4	47 ± 9
IC 0749	0.8	–	0.90	0.82	>10.1	>4.0	-0.070	2.2 ± 1.0	95 ± 17
UGC 06983	3.1	–	0.89	0.87	>15.9	>5.1	-0.024	6.4 ± 1.6	69 ± 8
NGC 4051	0.4	–	0.72	0.71	7.8	3.4	-0.108	8.3 ± 5.4	258 ± 126
NGC 4068	0.7	–	0.77	0.95	3.5	4.1	-0.038	5.8 ± 7.7	79 ± 93
NGC 4088	0.6	–	0.97	0.94	12.1	6.5	-0.054	8.6 ± 5.1	201 ± 73
NGC 4096	0.9	–	0.81	0.82	12.8	5.2	-0.069	5.3 ± 0.8	138 ± 8
NGC 4138	1.0	–	0.76	0.91	6.3	4.4	-0.066	3.0 ± 0.1	208 ± 2
NGC 4242	1.7	–	0.68	0.67	>3.1	>2.8	-0.076	2.2 ± 1.5	88 ± 38
NGC 4389	0.1	–	0.17	0.17	0.5	0.6	-0.124	1.4 ± 0.2	145 ± 9
NGC 4861	0.6	–	0.86	0.81	>11.6	>5.9	-0.071	7.8 ± 2.3	50 ± 10
NGC 5005	0.5	0.3	0.72	0.86	>11.2	>4.1	-0.066	2.7 ± 0.3	202 ± 10
NGC 5033	0.4	0.4	0.53	0.96	13.6	2.4	-0.057	5.7 ± 0.3	203 ± 3
UGC 08303	2.6	–	0.85	0.82	>3.7	>4.6	-0.059	0.6 ± 0.2	42 ± 5
UGC 08320	1.1	–	0.38	0.40	2.0	1.9	-0.147	2.5 ± 0.7	74 ± 13
NGC 5055	0.5	0.4	0.62	1.0	15.9	3.3	-0.055	3.7 ± 0.2	166 ± 1
UGC 08839	3.0	–	0.59	0.49	6.1	3.3	-0.086	5.9 ± 0.1	88 ± 6
NGC 5608	1.8	–	0.59	0.69	2.3	2.9	-0.096	1.5 ± 0.3	71 ± 6
NGC 7793	0.6	–	0.64	0.53	4.0	3.3	-0.067	3.1 ± 0.3	131 ± 6

Notes. [a] Relative baryonic contribution to the total observed gravitational potential measured at 2.2 times the average disc radial scale length, $h_{\rm R}$, and the radius at which the total baryonic contribution to the observed rotation curve is maximal, $R_{\rm bary}$.

[b] The radius at which the gravitational potential transitions from baryon-dominated to dark-matter-dominated (where $M_{\rm bary}/M_{\rm tot} = 0.5$) expressed in kpc and in terms of disc radial scale lengths ($h_{\rm R}$) measured at 3.6 μm.

[c] Rate at which the baryonic-to-total mass fraction decreases.

that have been determined from the upper and lower M/L limits. This error has been computed as the average difference between the values calculated using the listed fixed M/L value and its ±0.1 variations. In some cases, the decomposition of the observed rotation curve was overestimated using a M/L of 0.5, so a value of 0.4 was adopted and only upper error limits were calculated. In the maximum disc/bulge assumption, the stellar disc and bulge were scaled such that their peak circular rotational velocities contribute maximally to the observed rotation curve on top of the contribution from the gas. A separate maximal M/L value was fit for the disc and bulge when both components are present. The maximum disc/bulge decomposition results are shown in Fig. E2 and Table 2. Uncertainties are not computed from the maximum stellar disc/bulge fits, as these values represent upper limits.

4 ANALYSIS

In this section, we use the rotation curve decompositions to investigate the distribution of mass in the complete kinematic sample. We motivate the selection of the fixed M/L results over the maximum disc/bulge assumption, and cluster galaxies into groups with similar mass distributions. Finally, structural and star formation properties of galaxies in each group are scrutinized to determine if they differ among galaxy mass distribution groups.

4.1 Mass distributions

As in Richards et al. (2016), we compare the radial distributions of baryonic-to-total mass fractions under both stellar M/L assumptions for all 34 galaxies in the final analysis sample (Fig. 6, left-hand panels). Many of the comparisons noted in Richards et al. (2016) for a subset of galaxies are more apparent with the complete final sample presented in Fig. 6. For example, it is apparent that the fixed M/L results in the top left panel display a much wider range of possible baryonic-to-total mass fraction distributions. Under the maximum disc/bulge assumption, there is noticeably less scatter and distinction between the fast and slow rotating galaxies. The fastest rotating and, therefore, most massive galaxies do not appear to shift much between the fixed M/L and maximum disc/bulge assumptions, while the mass fraction distributions in the slower rotating, less

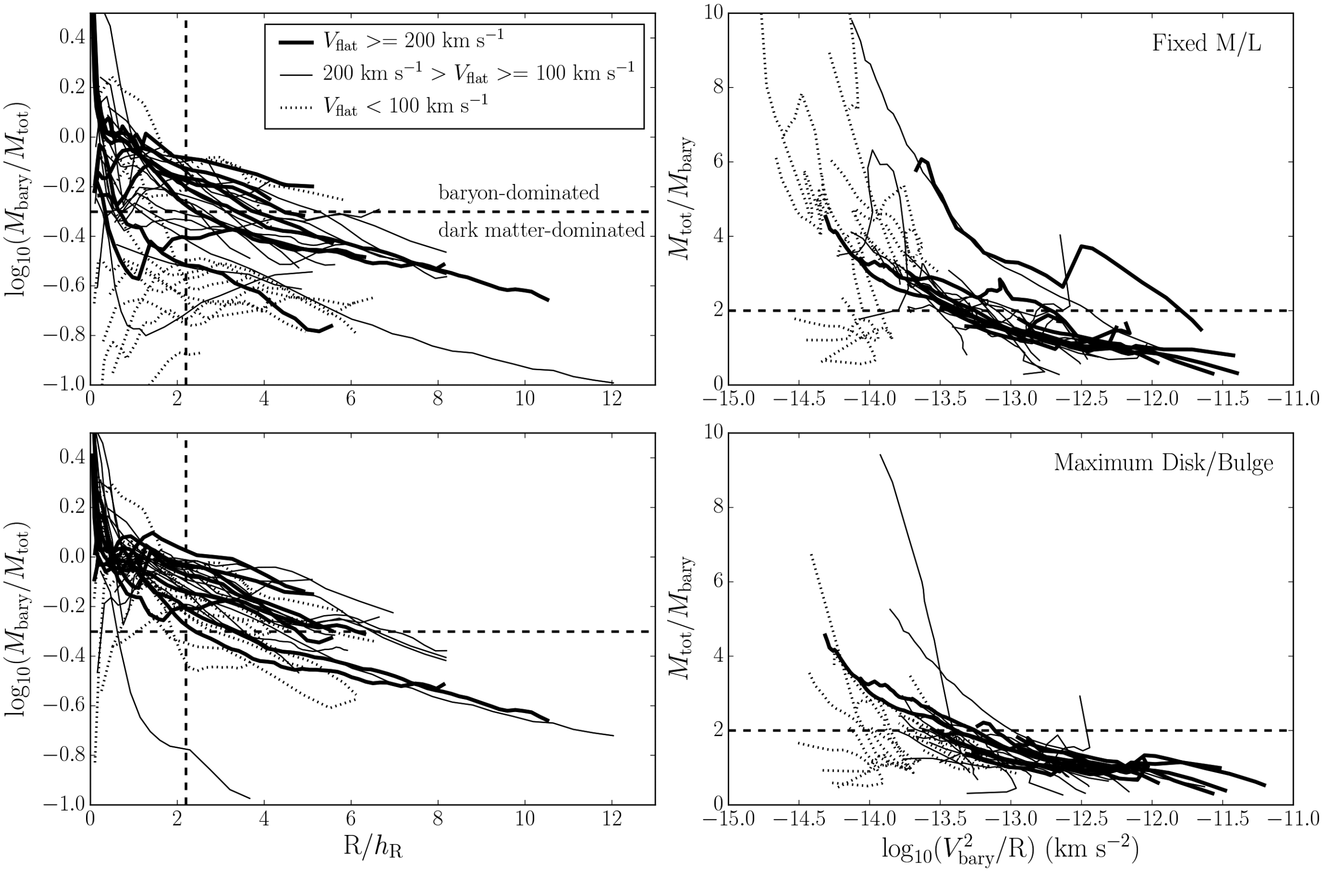

Figure 6. Left: radial distributions of baryonic-to-total mass fractions in each galaxy. Radii have been scaled by average disc scale length measured at 3.6 μm. Right: mass discrepancy, defined as the inverse of the baryonic-to-total mass fraction, as a function of radial acceleration due to the baryonic component. The top panels display results from the fixed stellar M/L = 0.5±0.1 decompositions, while the bottom panels show the maximum stellar disc/bulge decomposition results. The horizontal dashed lines in each plot denote where the mass fraction transitions from being baryon-dominated to dark-matter-dominated (where $M_{\rm bary}/M_{\rm tot} = 0.5$ on the left and $M_{\rm tot}/M_{\rm bary} = 2.0$ on the right). The vertical dashed lines in the left plots mark the location of 2.2$h_{\rm R}$. The most massive galaxies, with $V_{\rm flat} \geq 200\,{\rm km\,s^{-1}}$, are plotted with a thick solid line, intermediate mass ($200\,{\rm km\,s^{-1}} > V_{\rm flat} \geq 100\,{\rm km\,s^{-1}}$) with a thin solid line, and the lowest mass galaxies ($V_{\rm flat} < 100\,{\rm km\,s^{-1}}$) are plotted with a dotted line.

massive galaxies are greatly affected. This implies that values of M/L = 0.5 at 3.6 μm correspond to nearly maximal discs in massive galaxies (see also Lelli et al. 2016a). The gravitational potentials in the most massive galaxies start out baryon-dominated and become increasingly more dark-matter-dominated with increasing radius. This is in contrast to the least massive galaxies that are often dark-matter-dominated at all radii under the fixed M/L assumption.

The right-hand panels in Fig. 6 show the MDARs for the EDGES kinematic sample derived from fixed M/L and maximum disc/bulge decompositions. As the radial acceleration due to the total baryonic component increases, the ratio of total-to-baryon mass decreases in manner that is similar for all galaxies. As in the radial distributions of baryonic-to-total mass, the prominent difference between the fixed M/L and maximum disc/bulge results is that the mass ratio in the slowest rotating galaxies becomes more baryon-dominated at smaller radial accelerations than in the maximum disc/bulge decompositions.

We use the left-hand panels in Fig. 6 to summarize and define attributes of the mass distributions in the galaxies. We take the ratio of baryonic-to-total mass ($M_{\rm bary}/M_{\rm tot}$) at 2.2 disc exponential scale lengths (2.2 $h_{\rm R}$), the radius at which an infinitely thin rotating exponential disc would have its maximum circular rotational velocity, to describe the global baryonic-to-total mass fraction. As a comparison, we additionally use the radius at which $V_{\rm bary}$ is maximal since this choice is more appropriate for the dwarf galaxies with smaller stellar contributions to their total baryonic mass. The radius at which the distribution of mass transitions from baryon- to dark-matter-dominated scaled by the galaxy's disc scale length ($R_{\rm trans}/h_{\rm R}$) describes how quickly, radially, the galaxy's potential becomes dominated by the dark matter halo. Finally, a linear regression analysis is used to fit the mass fraction distribution beyond one disc scale length to determine the rate at which the baryonic-to-total mass fraction decreases ($M_{\rm bary}/M_{\rm tot}$ gradient). These mass distribution attributes are reported in Tables 1 and 2 for the fixed and maximal M/L results, respectively. It is important to note that these parameterizations of the mass distribution are independent of the dark matter halo model fit in the rotation curve decomposition.

As discussed in Richards et al. (2016), it is not possible to distinguish either the maximal disc/bulge or fixed M/L decomposition as the absolutely correct result without additional constraints on the true baryonic contribution. However, the fixed M/L decompositions appear to offer more astrophysically plausible results, as the maximum disc solutions for the lowest mass and lowest surface brightness galaxies require large M/Ls that would imply unphysical stellar populations. Fig. 7 demonstrates the dependence of the adopted maximum disc M/L on central surface brightness derived

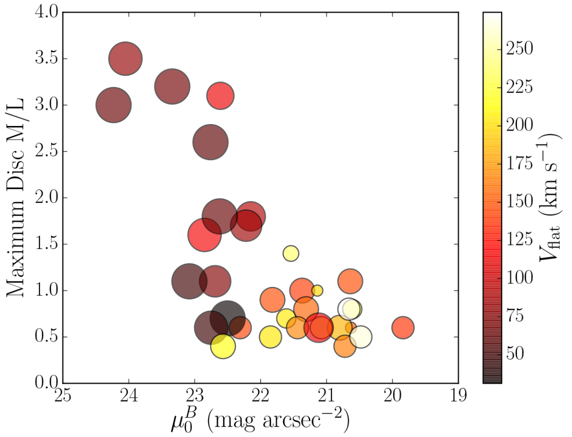

Figure 7. Adopted stellar disc M/L assuming the stellar contribution to the observed rotation curve is maximal near the centre as a function of central surface brightness measured in the optical *B* band. μ_0^B is derived from an exponential fit to the outer surface brightness profile. Points are coloured by their observed outer circular rotational velocity, $V_{\rm flat}$, and scaled in size by their morphological T type.

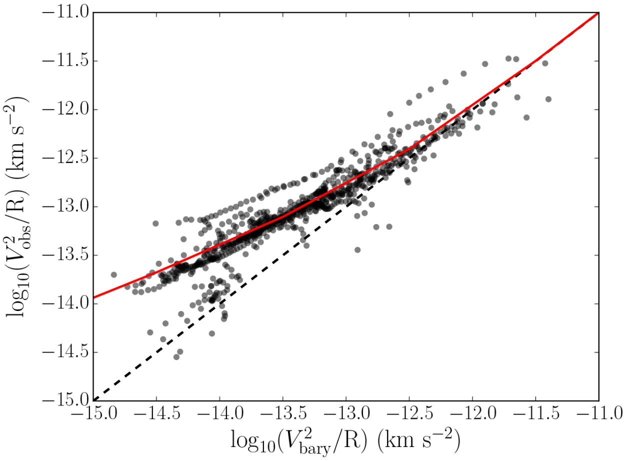

Figure 8. Radial acceleration relation for the complete EDGES kinematic sample. Each data point represents a measurement at a single radius. The dashed line is the one-to-one correlation between the observed and baryonic radial acceleration. The solid red line represents the fit derived in equation (4) of McGaugh et al. (2016) for rotationally supported galaxies.

from exponential fits to the outer stellar discs. This tendency for low surface brightness galaxies to have higher M/Ls than their high surface brightness counterparts under the maximum disc assumption has been encountered in many previous decomposition studies (e.g. de Blok & McGaugh 1997; McGaugh & de Blok 1998; Swaters et al. 2011). The impact of the assumed M/L on the mass distribution attributes for the most massive galaxies is relatively minimal. We, therefore, move forward with the more astrophysically plausible fixed M/L results and explore whether differences in distribution of mass correspond to measurable differences in stellar and gas properties.

Much attention has recently been given to the strong correlation between the observed radial acceleration and the radial acceleration expected from the baryons alone, known as the radial acceleration relation (McGaugh, Lelli & Schombert 2016; Lelli et al. 2017). Fig. 8 presents the radial acceleration relation for the 34 galaxies in the EDGES kinematic sample with rotation curve decompositions assuming a fixed M/L. The dashed line provides the one-to-one correlation between the observed radial acceleration and the baryons only radial acceleration while the solid red line shows the empirically derived function fit to the radial acceleration relation for rotationally supported galaxies in the SPARC sample (equation 4 in McGaugh et al. 2016). The function derived in McGaugh et al. (2016) provides a good fit to the EDGES kinematic sample data, with the exception of a handful of outliers. The outliers are galaxies for which there is still some uncertainty as to whether the neutral and/or ionized gas is tracing the gravitational potential. Most notably, the outliers that fall below the fitted relation and instead lie near the one-to-one line at small radial accelerations include NGC 4068 and NGC 4861 that exhibit regions of intense star formation. There are an additional two outlying galaxies that lie above the relation, NGC 3998 and NGC 4138. They are also visible outliers in the top right-hand panel of Fig. 6. These galaxies have the same functional form, but are offset to larger mass discrepancies and observed total radial accelerations for a given baryons-only radial acceleration. Both NGC 3998 and NGC 4138 are spheroidal-type galaxies (SA0) with complex H I velocity fields and uncertain inclination angles, which could cause the circular rotational velocities to be overestimated. Incorrect distance estimates could cause the same observed systematic offset, and cannot be ruled out as the culprit, especially as the adopted distances to these galaxies originate from the same study (Tonry et al. 2001).

4.2 Baryon properties of galaxies with similar mass distributions

Fig. 9 presents the organization of the galaxies in the three-dimensional space defined by the mass distribution attributes, where the point sizes represent $R_{\rm trans}/h_{\rm R}$. The top plots use the baryon-to-total mass fraction at $2.2h_R$, while the bottom plots use the baryon-to-total mass fraction at $R_{\rm bary}$. Galaxies were clustered into four different groups based on their position in this three-dimensional space using a k-means clustering algorithm, after being scaled to account for the different units and standard deviations of the three variables. The point colours in the plots on the left show the group assignments from this clustering, while the point colours in the right plots correspond to morphological type.

With the galaxies assigned to groups of similar mass distribution attributes, we can examine whether galaxies within each group exhibit similarities in gas and star properties. It is well established that rotation curve shapes and distributions of mass in galaxies roughly correlate with morphological type in the sense that dwarf galaxies tend to have slowly rising rotation curves out to the last measured point with larger dark matter components (e.g. Broeils 1992; Roberts & Haynes 1994). The morphological type also provides a convenient qualitative summarization of a galaxy's dominant stellar characteristics based on its optical appearance. We examine if morphological type is the primary driver behind the differences in mass distribution attributes in the right-hand side panels of Fig. 9. The galaxies do not fall into distinct clusters based on their morphological types, but some global trends are apparent. For example, galaxies with the largest baryon-to-total mass fractions, largest transition radii, and steepest gradients (groups 2 and 4 in the left plots) tend to be spirals of Sa-Sb morphologies (red points). Galaxies in groups 1 and 3 in the left plots appear to correspond primarily to dwarf irregulars and late-type spirals (blue and green points). Late-type Sc-Sd spiral galaxies are the most diverse morphological type in the sense of mass distribution with representation in all clusters.

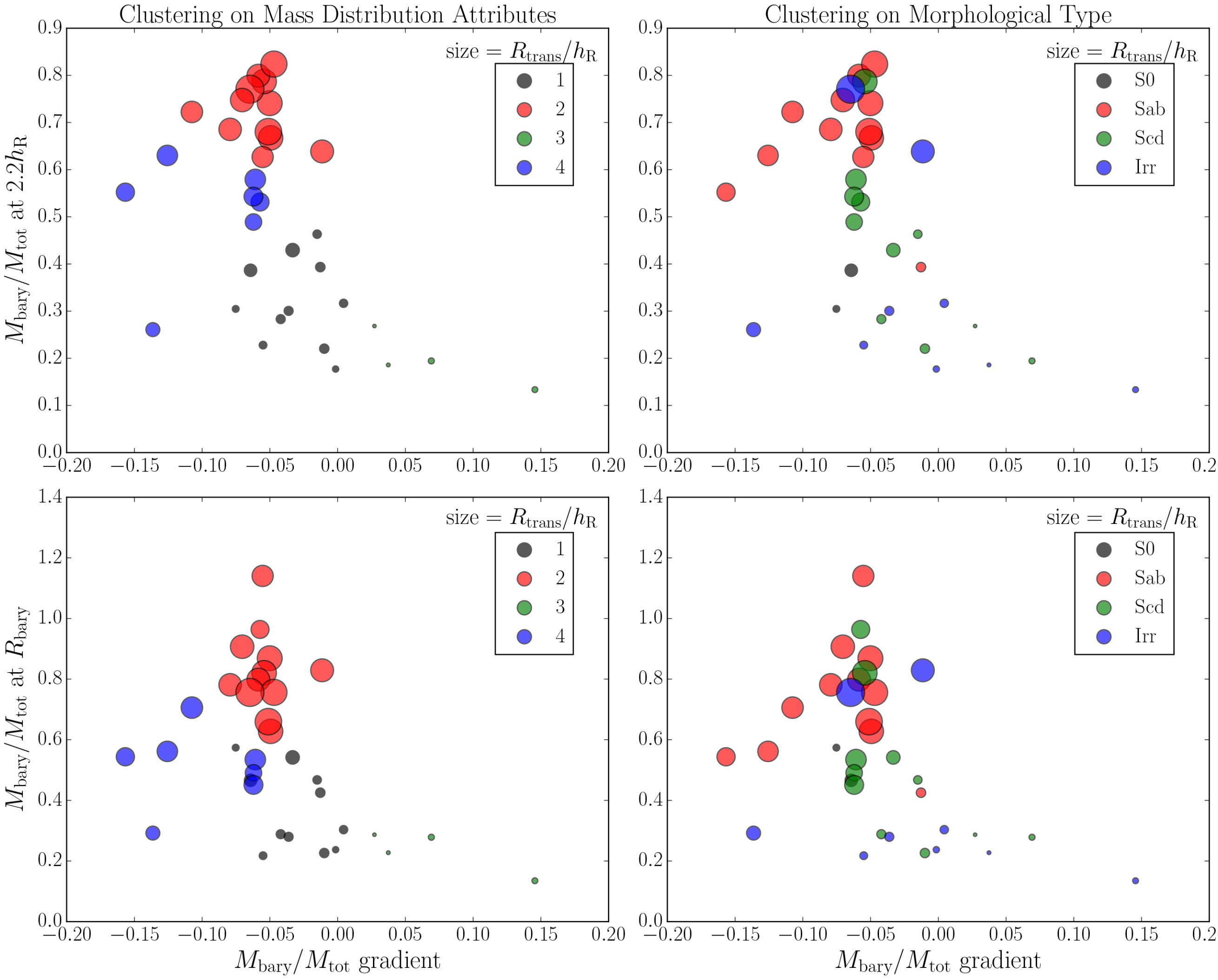

Figure 9. Baryonic-to-total mass fraction at $2.2h_{\rm R}$ (top) and $R_{\rm bary}$ (bottom) versus baryonic-to-total mass fraction radial gradient. Point sizes in all plots represent the value of the transition radius normalized by the disc scale length, $R_{\rm trans}/h_{\rm R}$. Point colours represent the galaxies' cluster assignments. Left: clustering in the three-dimensional mass distribution space. Right: grouping based on the galaxy's morphological type.

Fig. 9 demonstrates that galaxies clustered with similar mass distribution attributes do not necessarily have similar optical morphologies. To make the analysis more explicit, we utilize boxplots to compare the distributions of specific stellar and gas properties of galaxies separated into the four mass distribution groups (Fig. 10). The top left-hand panel demonstrates the range of baryonic masses among galaxies in each cluster. Mass distribution groups 2 and 4 (red and blue points, respectively, in the left plots of Fig. 9) have median baryonic masses about an order of magnitude greater than groups 1 and 3 (black and green points, respectively), but there is still much overlap between the groups. This result is expected in the context of the mass distribution clustering, as it simply indicates that baryon-dominated galaxies, described as having greater baryon-to-total mass fractions and longer transition radii, also have larger total baryonic masses. Based on the scaling relations with $M_{\rm bary}$ displayed in Fig. 3, galaxies in mass distribution groups 2 and 4 also tend to have redder $B-R$ colours, larger total SFRs, longer exponential disc scale lengths, and larger stellar disc diameters than galaxies in mass distribution groups 1 and 3. The top right-hand panel in Fig. 10 further reveals that the more gas-rich galaxies, in terms of total gas to stellar mass ratio, tend to reside in groups 1 and 3. This is also likely a consequence of a slight anticorrelation between gas fraction and total baryonic mass.

Similarities among galaxies within the same mass distribution group become less obvious when stellar and star formation properties are considered. For example, there does not appear to be any correlation between distribution of mass and concentration of stellar light (Fig. 10, middle left-hand panel) or EW (middle right-hand panel). There is a slight, but not significant tendency for galaxies in mass distribution groups 1 and 3 to have more negatively sloped linear radial gradients in $B-R$ colour. Furthermore, galaxies in group 3 have the most positively sloped linear radial gradients in $\log_{10}$(EW), meaning those galaxies typically exhibit higher current to past star formation activity at larger radii.

In the context of this discussion, one interpretation of the results is there is a small, non-significant propensity for galaxies that have stellar profiles indicative of more active star formation in their outer regions to have mass distributions that are dark-matter-dominated. We acknowledge, however, that the sample size is small and that a more likely interpretation is that this result is just an artefact of the aforementioned trends with baryonic mass and morphological type. Altogether, the clustering results imply that the mass

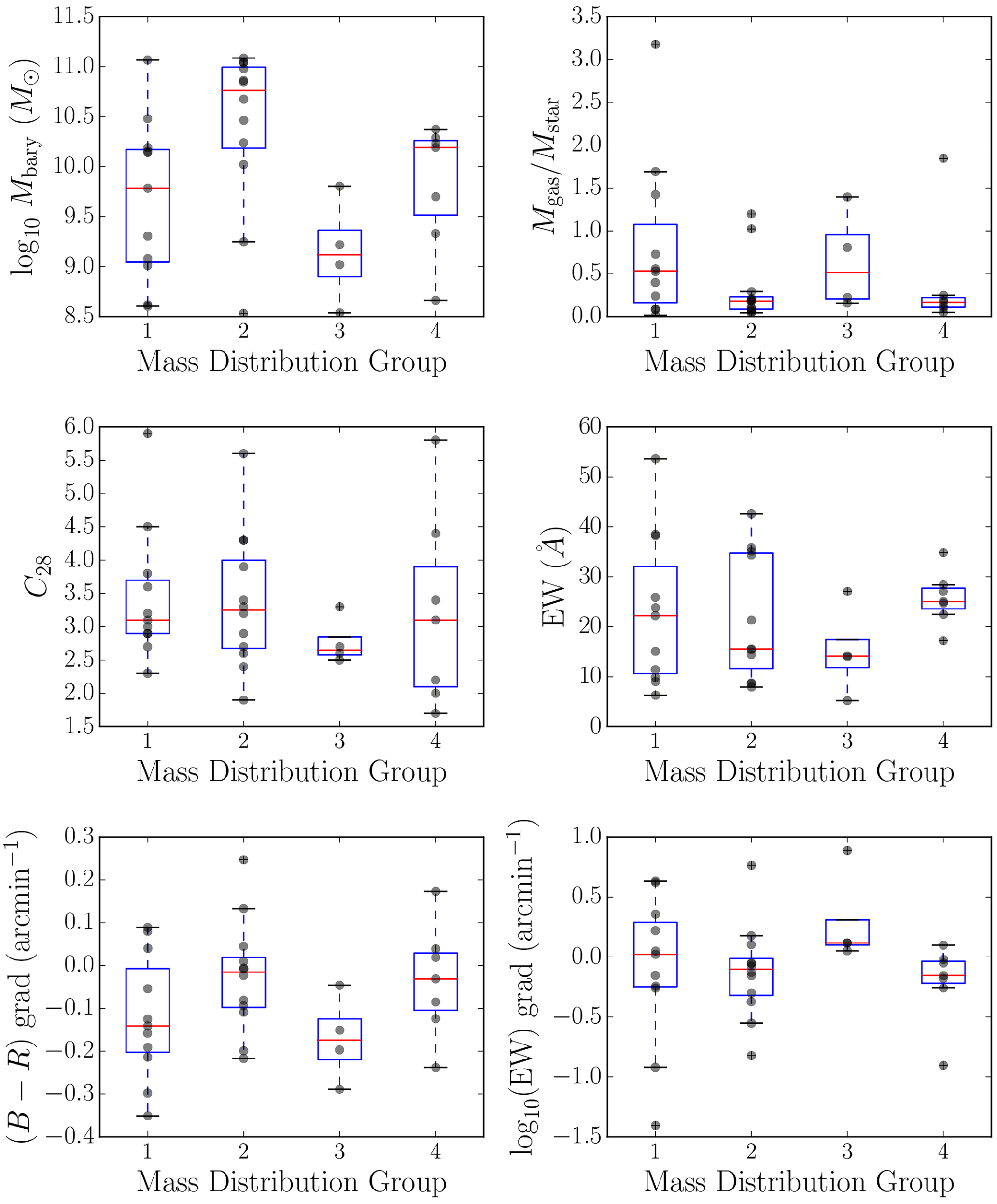

Figure 10. Boxplot comparison of global and structural characteristics of galaxies separated by mass distribution cluster assignment. Top left: total baryonic mass. Top right: total gas mass to stellar mass fraction. Middle left: radial concentration of stellar light. Middle right: equivalent width. NGC 4861 is not shown due to its extremely large EW value of 176 Å, dominated by the bright star-forming H II region I Zw 49. Bottom left: linear radial gradient in $B-R$ colour. Bottom right: linear radial gradient in equivalent width. Group numbers are as in Fig. 9: group 1 = black points, group 2 = red points, group 3 = green points, group 4 = blue points.

discrepancy in a galaxy, which is known to correlate with total baryonic mass, does not appear to correlate strongly with any characteristics of its star formation history. This emphasizes the role of baryons in simulations that must be able to produce galaxies with similar distributions of dark and baryonic mass that evolve with different star formation histories.

5 CONCLUSION

We have presented final results from rotation curve decomposition analysis of the complete EDGES kinematic sample. New and archival H I synthesis observations from the VLA and WSRT and new IFS observations from SparsePak on the WIYN 3.5 m telescope have been acquired to constrain the neutral and ionized gas kinematics. We took advantage of *Spitzer* 3.6 µm images to trace the extended stellar populations, as well as optical broad-band *B* and *R* and narrow-band H α from the WIYN 0.9 m telescope to measure properties of the dominant stellar populations. This multiwavelength data set was used to illustrate the important role of baryons in creating diverse populations of galaxies, even when they form inside similarly structured dark matter haloes. The main results are summarized below.

(i) Ionized and neutral gas rotation curves for the 27 remaining galaxies in the EDGES kinematic sample, including new H I radio synthesis observations of three galaxies from the VLA and new ionized gas IFS observations for 13 galaxies from SparsePak, are presented in Fig. C1. Rotation curve decomposition results for the complete final sample of 34 galaxies are presented in Figs E1 and E2 and summarized in Tables 1 and 2.

(ii) We have demonstrated how the rotation curve decomposition results change under the assumption of a fixed stellar M/L = 0.5±0.1 and maximal contribution to the observed inner dynamics (Fig. 6). The key findings from this comparison are that the faster rotating more massive galaxies have stellar contributions closer to maximal than the slower rotating less massive galaxies and that the maximum disc/bulge decompositions require non-physical M/Ls for the lowest mass galaxies. Fig. 6 is used to define summary attributes for the distribution of mass in galaxies.

(iii) Exploratory clustering analysis using the fixed M/L results reveals a range of stellar and star formation properties within groups of galaxies with similar mass distribution attributes. This implies that even galaxies whose baryons were distributed similarly in their gravitational potentials have likely undergone different star formation histories.

The analysis of the distribution of baryonic and dark matter mass in galaxies has uncovered a diverse range of baryonic attributes among galaxies with similar distributions of mass. Taken at face value, this suggests that the physical processes governing the evolution of the gas and stars in galaxies vary even within similar parent dark matter haloes. It is somewhat remarkable, then, that the chaotic process of star formation and feedback mechanisms may alter the distribution and characteristics of the baryons in galaxies without changing the tight relationship between total baryonic mass and dark matter halo mass. Comparisons between observations and simulations in this context will be critical to our progress in understanding how galaxies form and evolve in dark matter haloes.

ACKNOWLEDGEMENTS

The authors thank Adrick Broeils, Martha P. Haynes, J. M. van der Hulst, and Marc A. W. Verheijen, as well as the THINGS, LITTLE THINGS, and WHISP collaborations, for providing H I data cubes and moment maps of archival data. The authors also acknowledge the referee for their insight and helpful recommendations that improved this manuscript. This paper is based on work presented in EER's PhD dissertation, which was accepted by Indiana University graduate faculty in partial fulfilment of the requirements for the degree. The authors acknowledge observational and technical support from the National Radio Astronomy Observatory (NRAO). We acknowledge use of the WIYN 0.9 m telescope operated by WIYN Inc. on behalf of a Consortium of ten partner Universities and Organizations, and the WIYN 3.5 m telescope. The WIYN Observatory is a joint facility of the University of Wisconsin-Madison, Indiana University, the National Optical Astronomy Observatory, and the University of Missouri. This work is based on observations made with the *Spitzer Space Telescope*, which is operated by the Jet Propulsion Laboratory, California Institute of Technology under a contract with NASA. E.E.R. acknowledges support from the Provost's Travel Award for Women in Science, a professional development fund supported through the Office of the Provost at Indiana University Bloomington, the Indiana University College of Arts and Sciences Dissertation Year Fellowship, and the Indiana Space Grant Consortium. L.v.Z. recognizes support from the Helena Kluyver Female Visitor programme at ASTRON during which some of this analysis was completed. This work was partially supported by NASA ADAP award NNX17AF17G. This research has made use of the NASA/IPAC Extragalactic Database (NED) that is operated by the Jet Propulsion Laboratory, California Institute of Technology, under contract with the National Aeronautics and Space Administration.

REFERENCES

Arnault P., Kunth D., Casoli F., Combes F., 1988, A&A, 205, 41
Barnes J. E., Hernquist L., 1992, Nature, 360, 715
Beck S. C., Lacy J. H., Turner J. L., 2010, ApJ, 722, 1175
Böker T., Lisenfeld U., Schinnerer E., 2003, A&A, 406, 87
Boselli A., Cortese L., Boquien M., 2014, A&A, 564, A65
Braine J., Combes F., Casoli F., Dupraz C., Gerin M., Klein U., Wielebinski R., Brouillet N., 1993, A&AS, 97, 887
Broeils A. H., 1992, PhD thesis, PhD thesis, Univ. Groningen
Bush S. J., Wilcots E. M., 2004, AJ, 128, 2789
Carignan C., Puche D., 1990, AJ, 100, 394
Clemens M. S., Alexander P., Green D. A., 1998, MNRAS, 297, 1015
Condon J. J., Condon M. A., Gisler G., Puschell J. J., 1982, ApJ, 252, 102
Cormier D. et al., 2014, A&A, 564, A121
Dalcanton J. J. et al., 2009, ApJS, 183, 67
de Blok W. J. G., McGaugh S. S., 1997, MNRAS, 290, 533
de Blok W. J. G., Walter F., Brinks E., Trachternach C., Oh S.-H., Kennicutt R. C., Jr, 2008, AJ, 136, 2648
de Vaucouleurs G., de Vaucouleurs A., Corwin H. G., Jr., Buta R. J., Paturel G., Fouqué P., 1991, Third Reference Catalogue of Bright Galaxies. Springer-Verlag, Berlin
Di Cintio A., Lelli F., 2016, MNRAS, 456, L127
Di Teodoro E. M., Fraternali F., 2015, MNRAS, 451, 3021
Dicaire I. et al., 2008, MNRAS, 385, 553
Drozdovsky I. O., Schulte-Ladbeck R. E., Hopp U., Greggio L., Crone M. M., 2002, AJ, 124, 811
Dumas G., Mundell C. G., Emsellem E., Nagar N. M., 2007, MNRAS, 379, 1249
Epinat B. et al., 2008a, MNRAS, 388, 500
Epinat B., Amram P., Marcelin M., 2008b, MNRAS, 390, 466
Eskew M., Zaritsky D., Meidt S., 2012, AJ, 143, 139
Ferrero I. et al., 2017, MNRAS, 464, 4736
Fitzpatrick E. L., 1999, PASP, 111, 63
Flohic H. M. L. G., Eracleous M., Chartas G., Shields J. C., Moran E. C., 2006, ApJ, 647, 140
Frank B. S., de Blok W. J. G., Walter F., Leroy A., Carignan C., 2016, AJ, 151, 94
Ganda K., Falcón-Barroso J., Peletier R. F., Cappellari M., Emsellem E., McDermid R. M., de Zeeuw P. T., Carollo C. M., 2006a, MNRAS, 367, 46
Ganda K., Falcón-Barroso J., Peletier R. F., Cappellari M., Emsellem E., McDermid R. M., de Zeeuw P. T., Carollo C. M., 2006b, MNRAS, 367, 46
Garrido O., Marcelin M., Amram P., 2004, MNRAS, 349, 225
Ho L. C., Filippenko A. V., Sargent W. L. W., Peng C. Y., 1997, ApJS, 112, 391
Hunter D. A., Wilcots E. M., van Woerden H., Gallagher J. S., Kohle S., 1998, ApJ, 495, L47
Hunter D. A., Hunsberger S. D., Roye E. W., 2000, ApJ, 542, 137
Hunter D. A. et al., 2012, AJ, 144, 134
Israel F. P., Tacconi L. J., Baas F., 1995, A&A, 295, 599
Johnson M. C., Hunter D., Wood S., Oh S.-H., Zhang H.-X., Herrmann K. A., Levine S. E., 2015, AJ, 149, 196
Józsa G. I. G., Kenn F., Klein U., Oosterloo T. A., 2007, A&A, 468, 731
Kaczmarek J. F., Wilcots E. M., 2012, AJ, 144, 67
Karachentsev I. D. et al., 2006, AJ, 131, 1361
Kennicutt R. C., Evans N. J., 2012, ARA&A, 50, 531
Kent S. M., 1986, AJ, 91, 1301
Krips M. et al., 2005, A&A, 442, 479
Lelli F., Verheijen M., Fraternali F., 2014, A&A, 566, A71
Lelli F., McGaugh S. S., Schombert J. M., 2016a, AJ, 152, 157

Lelli F., McGaugh S. S., Schombert J. M., 2016b, ApJ, 816, L14
Lelli F., McGaugh S. S., Schombert J. M., Pawlowski M. S., 2017, ApJ, 836, 152
Leroy A., Bolatto A. D., Simon J. D., Blitz L., 2005, ApJ, 625, 763
McGaugh S. S., 2004, ApJ, 609, 652
McGaugh S. S., 2012, AJ, 143, 40
McGaugh S. S., de Blok W. J. G., 1998, ApJ, 499, 41
McGaugh S. S., Schombert J. M., 2015, ApJ, 802, 18
McGaugh S. S., Schombert J. M., Bothun G. D., de Blok W. J. G., 2000, ApJ, 533, L99
McGaugh S. S., Lelli F., Schombert J. M., 2016, Phys. Rev. Lett., 117, 201101
McMullin J. P., Waters B., Schiebel D., Young W., Golap K., 2007, in Shaw R. A., Hill F., Bell D. J., eds, ASP Conf. Ser. Vol. 376, Astronomical Data Analysis Software and Systems XVI. Astron. Soc. Pac., San Francisco, p. 127
McQuinn K. B. W., Mitchell N. P., Skillman E. D., 2015, ApJS, 218, 29
Mundell C. G., Shone D. L., 1999, MNRAS, 304, 475
Mundell C. G., Pedlar A., Shone D. L., Robinson A., 1999, MNRAS, 304, 481
Noordermeer E., van der Hulst J. M., Sancisi R., Swaters R. A., van Albada T. S., 2005, A&A, 442, 137
Oh S.-H. et al., 2015, AJ, 149, 180
Oke J. B., 1990, AJ, 99, 1621
Ostriker J. P., Caldwell J. A. R., 1979, in Burton W. B., ed., Proc. IAU Symp. 84, The Large-Scale Characteristics of the Galaxy. D. Reidel Publ. Co., Dordrecht, p. 441
Ott J. et al., 2012, AJ, 144, 123
Pedlar A., Howley P., Axon D. J., Unger S. W., 1992, MNRAS, 259, 369
Pott J.-U., Hartwich M., Eckart A., Leon S., Krips M., Straubmeier C., 2004, A&A, 415, 27
Radburn-Smith D. J. et al., 2011, ApJS, 195, 18
Richards E. E. et al., 2015, MNRAS, 449, 3981
Richards E. E. et al., 2016, MNRAS, 460, 689
Roberts M. S., Haynes M. P., 1994, ARA&A, 32, 115
Sales L. V. et al., 2017, MNRAS, 464, 2419
Schlafly E. F., Finkbeiner D. P., 2011, ApJ, 737, 103
Schwarz U. J., 1985, A&A, 142, 273
Sofue Y., Tutui Y., Honma M., Tomita A., 1997, AJ, 114, 2428
Spano M., Marcelin M., Amram P., Carignan C., Epinat B., Hernandez O., 2008, MNRAS, 383, 297
Sparke L. S., van Moorsel G., Schwarz U. J., Vogelaar M., 2009, AJ, 137, 3976
Spekkens K., Sellwood J. A., 2007, ApJ, 664, 204
Stil J. M., Israel F. P., 2002, A&A, 389, 42
Swaters R. A., 1999, PhD thesis, Rijksuniversiteit Groningen
Swaters R. A., van Albada T. S., van der Hulst J. M., Sancisi R., 2002, A&A, 390, 829
Swaters R. A., Sancisi R., van Albada T. S., van der Hulst J. M., 2009, A&A, 493, 871
Swaters R. A., Sancisi R., van Albada T. S., van der Hulst J. M., 2011, ApJ, 729, 118
Thuan T. X., Hibbard J. E., Lévrier F., 2004, AJ, 128, 617
Tonry J. L., Dressler A., Blakeslee J. P., Ajhar E. A., Fletcher A. B., Luppino G. A., Metzger M. R., Moore C. B., 2001, ApJ, 546, 681
Tully R. B., Bottinelli L., Fisher J. R., Gougenheim L., Sancisi R., van Woerden H., 1978, A&A, 63, 37
Tully R. B. et al., 2013, AJ, 146, 86
Usui T., Saitō M., Tomita A., 2001, AJ, 121, 2483
van der Hulst J. M., Terlouw J. P., Begeman K. G., Zwitser W., Roelfsema P. R., 1992, in Worrall D. M., Biemesderfer C., Barnes J., eds, ASP Conf. Ser. Vol. 25, Astronomical Data Analysis Software and Systems I. Astron. Soc. Pac., San Francisco, p. 131
van der Hulst J. M., van Albada T. S., Sancisi R., 2001, in Hibbard J. E., Rupen M., van Gorkom J. H., eds, ASP Conf. Ser. Vol. 240, Gas and Galaxy Evolution. Astron. Soc. Pac., San Francisco, p. 451
van Eymeren J., Marcelin M., Koribalski B. S., Dettmar R.-J., Bomans D. J., Gach J.-L., Balard P., 2009, A&A, 505, 105
van Eymeren J., Jütte E., Jog C. J., Stein Y., Dettmar R.-J., 2011, A&A, 530, A29
van Moorsel G. A., 1983, A&AS, 54, 19
van Zee L., Dale D. A., Barnes K. L., Staudaher S., Calzetti D., Dalcanton J. J., Bullock J. S., Chandar R., 2012, American Astronomical Society Meeting Abstracts 220. p. 433.08
Verheijen M. A. W., Sancisi R., 2001, A&A, 370, 765
Viallefond F., Allen R. J., de Boer J. A., 1980, A&A, 82, 207
Walter F., Brinks E., de Blok W. J. G., Bigiel F., Kennicutt R. C., Jr, Thornley M. D., Leroy A., 2008, AJ, 136, 2563
Wilcots E. M., Lehman C., Miller B., 1996, AJ, 111, 1575
Young J. S. et al., 1995, ApJS, 98, 219

APPENDIX A: NOTES ON INDIVIDUAL GALAXIES

This appendix presents short descriptions of the 27 remaining galaxies in the EDGES kinematic sample. Observational data products are presented in Figs A1–A26.

A1 NGC 3507

The H I data comes from archival VLA C configuration observations (project code AD947), which do not appear to be published in the literature. The field of view of the VLA observations are spatially centred between NGC 3507 and the nearby edge-on galaxy NGC 3501. The H I distribution is clumpy with a central hole. The stellar distribution reveals two grand design spiral arms emanating from both ends of a central bar. The bar is not as visible in the ionized gas, which displays a strong nuclear point source. X-ray emission associated with this central source suggests that NGC 3507 is a LINER powered by stellar processes (Flohic et al. 2006). The EW profile rises from the centre, indicating more recent star formation in the disc of the galaxy.

The neutral gas kinematics result in a flat rotation curve, but are difficult to constrain due to the low inclination angle of NGC 3507. The ionized gas kinematics are likely influenced by the stellar bar and/or nuclear activity, and are not well-modelled by the stellar contribution to the total observed rotation curve. The adopted inclination angle of 17° results in a $V_{\rm flat}$ that gives an Luminous Tully-Fisher Relation (LTFR) distance of 42.5 Mpc, which is much larger than other Tully–Fisher distance estimates in the literature. Using this distance, the mass distribution of NGC 3507 is baryon-dominated assuming a fixed M/L = 0.5 and maximum disc M/L = 0.8, largely due to the relatively short radial extent of the H I that limits how far out the gravitational potential can be traced.

A2 UGC 06161

The H I data from WHISP appear more extended than the stellar component in this dwarf galaxy. The H I velocity field and rotation curve indicate solid body rotation. Decomposing the rotation curve reveals a mass distribution that is dark-matter-dominated at nearly all radii assuming M/L = 0.5 and beyond 1.7 disc scale lengths assuming maximal stellar contribution with M/L = 1.1.

A3 NGC 3718

NGC 3718 and companion galaxy NGC 3729, located ∼11 arcmin to the east, are part of the Ursa Major cluster of galaxies (Verheijen & Sancisi 2001). NGC 3718 contains a severely warped H I disc with a stellar distribution that is just as peculiar. The H I data used here are from VLA observations originally published in Sparke et al. (2009) who describe the complex dynamics in great detail.

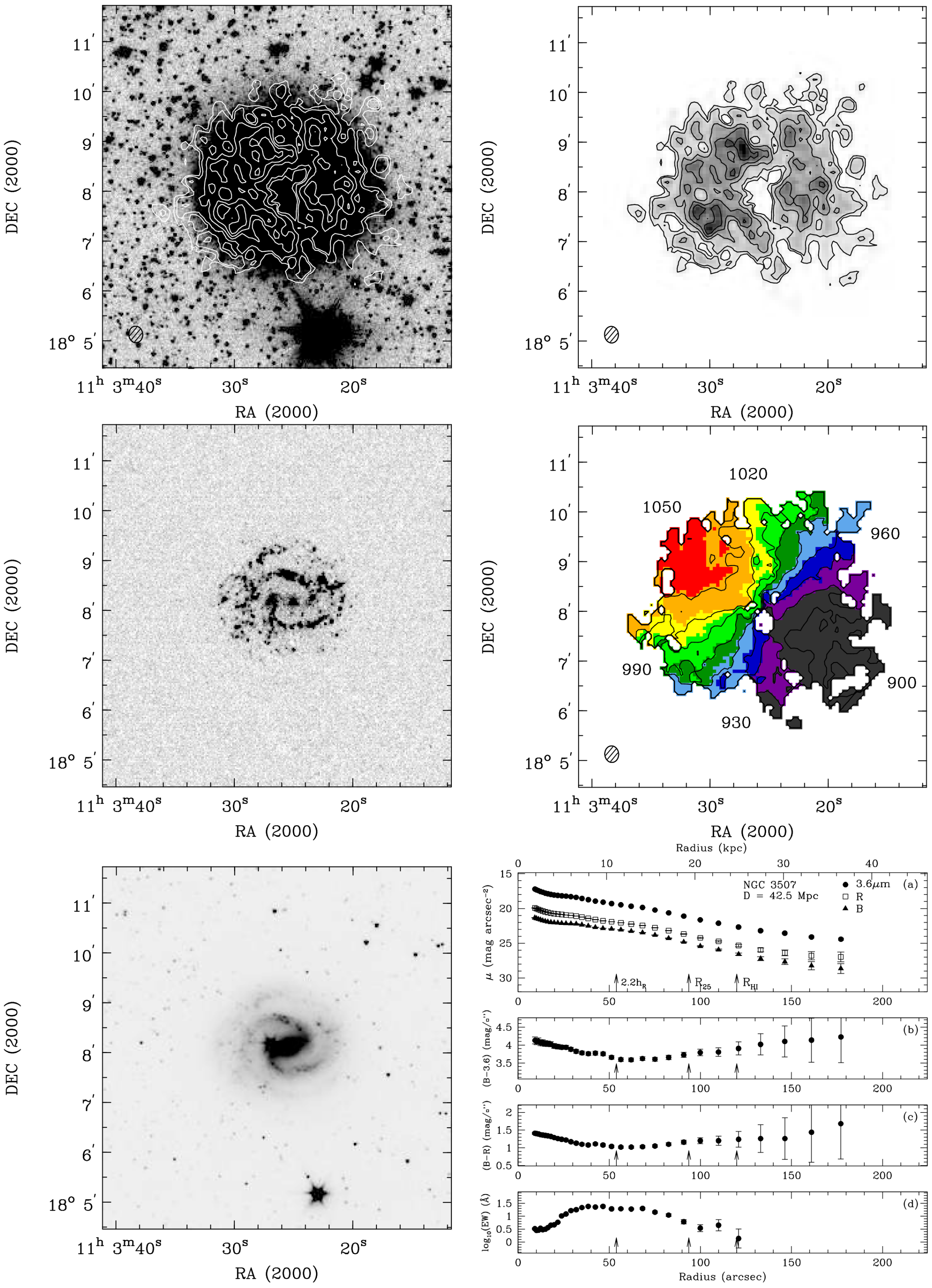

Figure A1. **NGC 3507:** (Top left) H I integrated intensity contours overlaid on the *Spitzer* 3.6 μm image. Top right: H I intensity contours overlaid on the H I intensity image. The first low resolution VLA H I contour represents a column density of 10^{20} atoms cm^{-2}. Middle left: continuum-subtracted narrow-band Hα image from the WIYN 0.9 m telescope. Middle right: H I velocity field with isovelocity contours. Bottom left: *Spitzer* 3.6 μm image with a high surface brightness stretch. Bottom right: ellipse photometry results showing radial profiles of surface brightness, $B-3.6$ colour, $B-R$ colour, and equivalent width (EW).

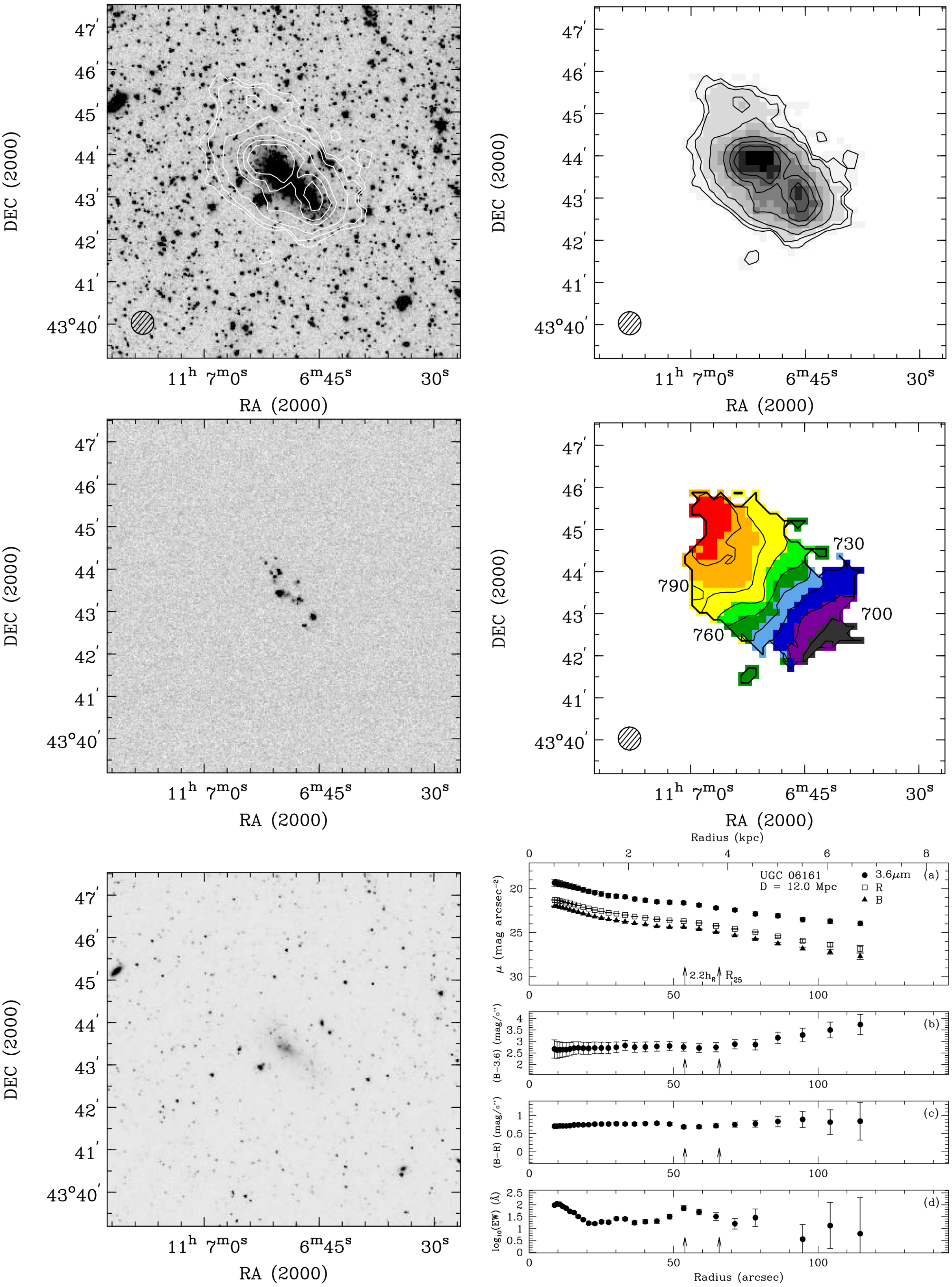

Figure A2. **UGC 06161:** Panels same as in Fig. A1. The first WHISP 30 arcsec resolution H I contour represents a column density of 10^{20} atoms cm^{-2}.

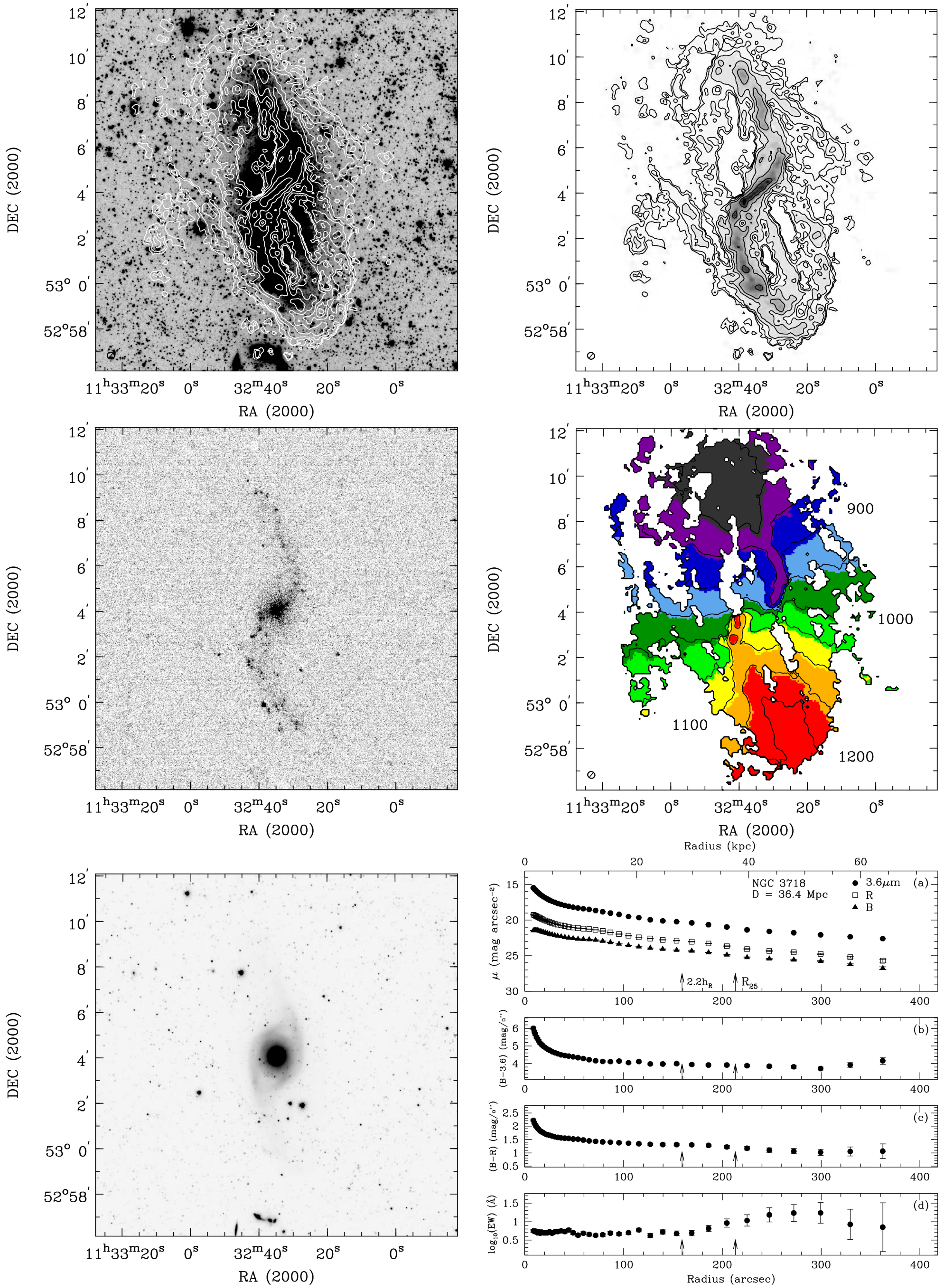

Figure A3. NGC 3718: Panels same as in Fig. A1. The first low-resolution VLA H I contour represents a column density of 10^{20} atoms cm^{-2}.

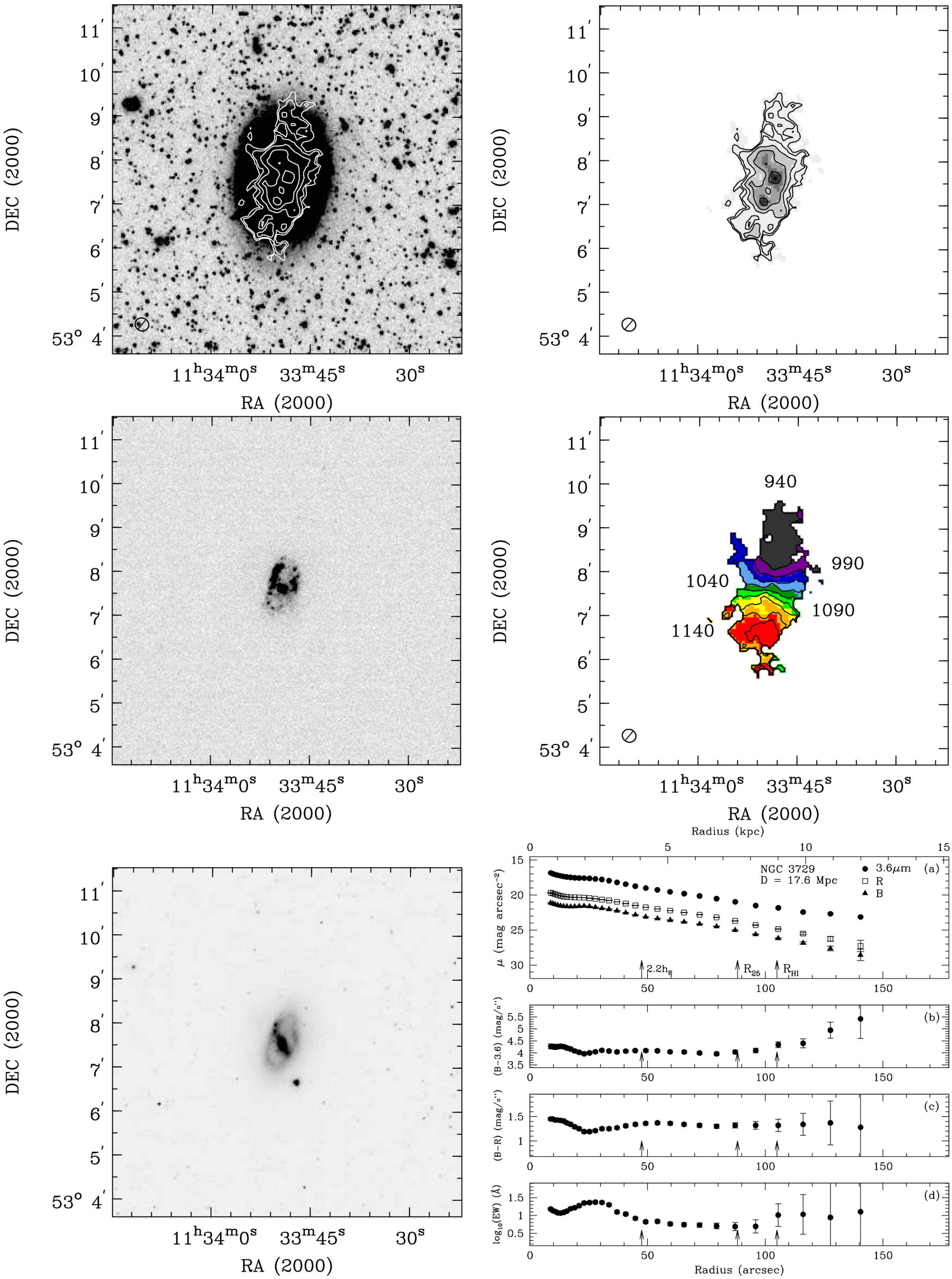

Figure A4. **NGC 3729:** Panels same as in Fig. A1. The first low-resolution VLA H I contour represents a column density of 10^{20} atoms cm^{-2}.

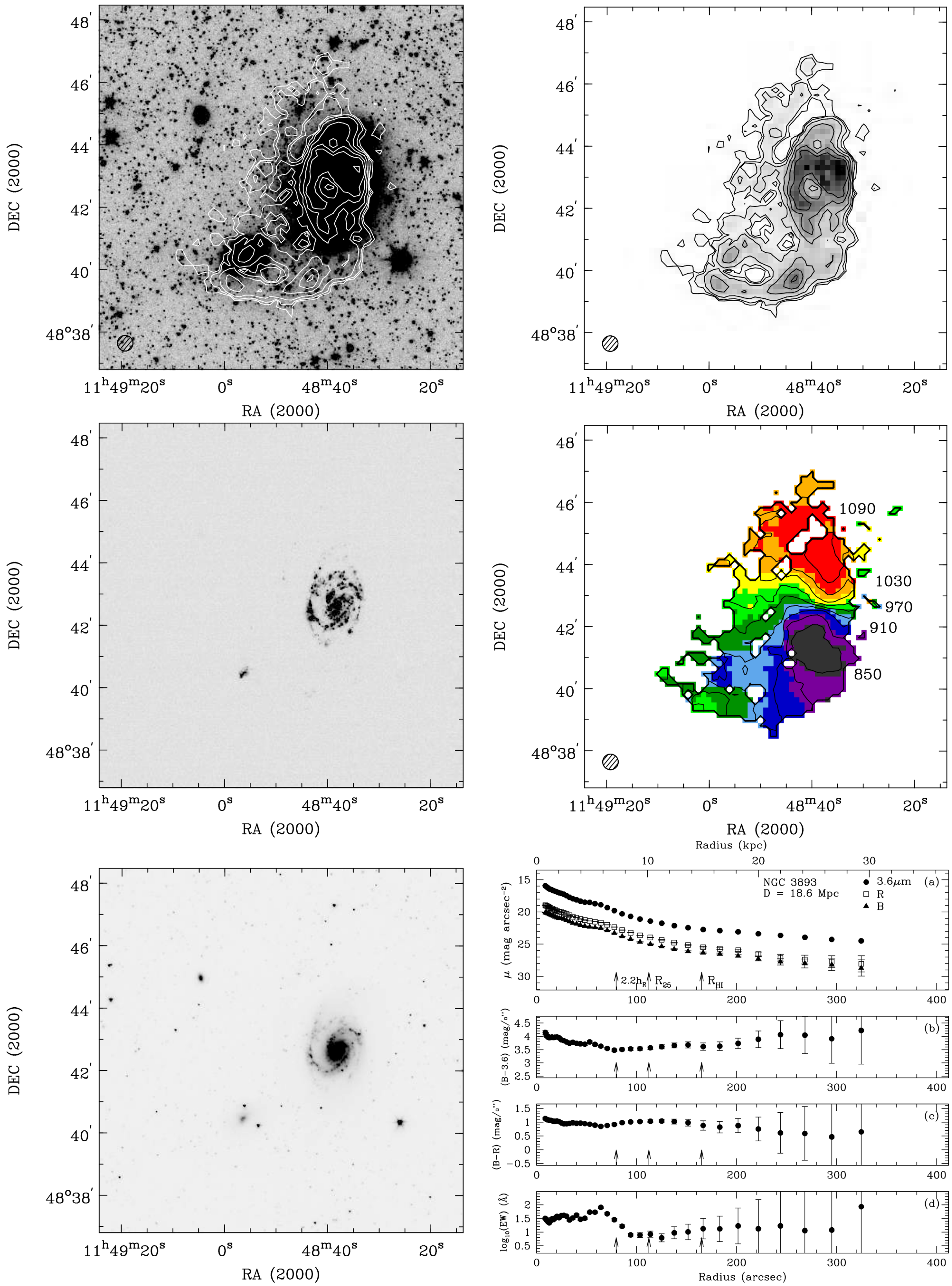

Figure A5. **NGC 3893:** Panels same as in Fig. A1. The first WHISP 30 arcsec resolution H I contour represents a column density of 10^{20} atoms cm^{-2}.

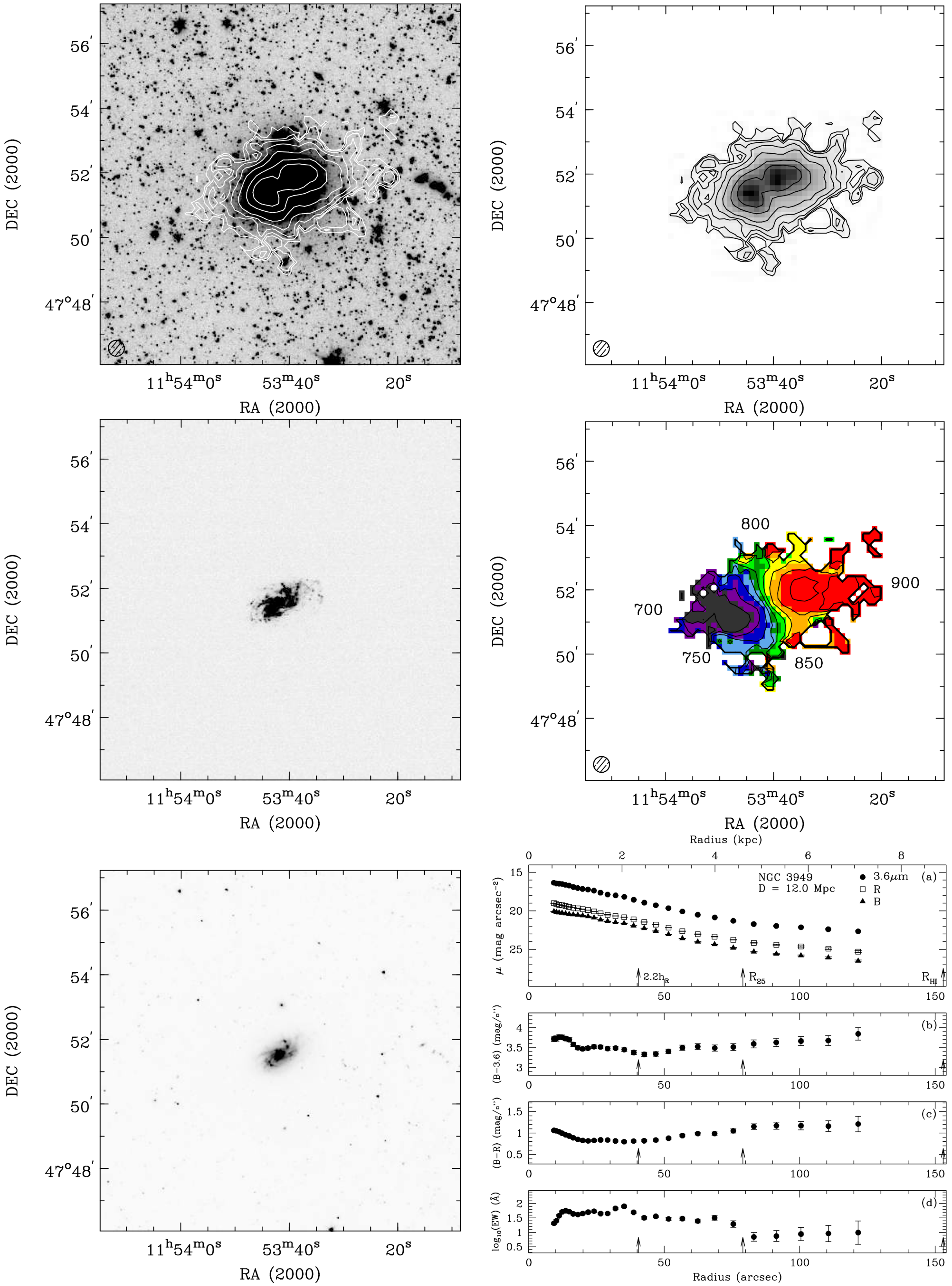

Figure A6. **NGC 3949:** Panels same as in Fig. A1. The first WHISP 30 arcsec resolution H I contour represents a column density of 5×10^{19} atoms cm^{-2}.

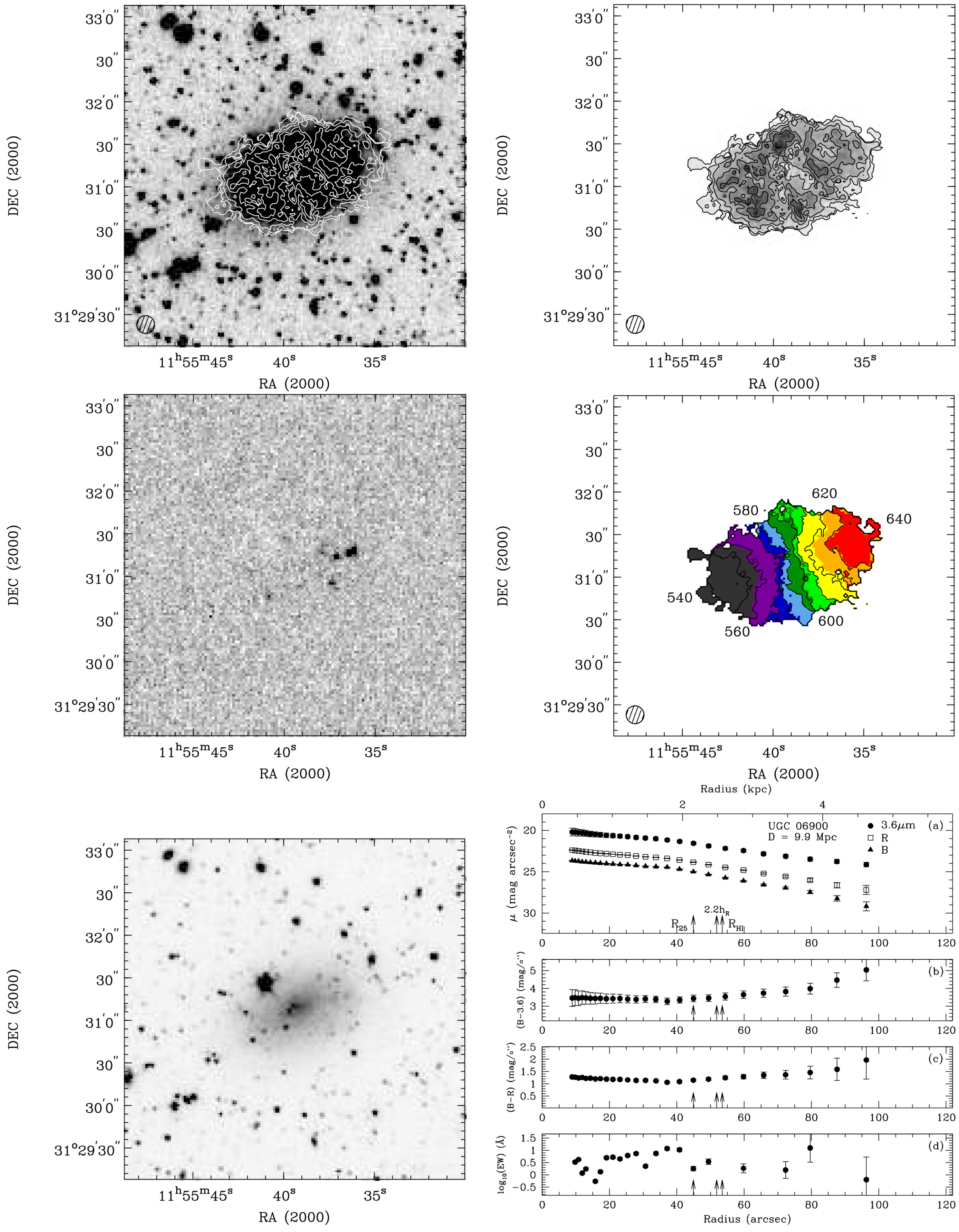

Figure A7. **UGC 06900:** Panels same as in Fig. A1. The first medium-resolution VLA H I contour represents a column density of 4 × 10^{20} atoms cm^{-2}.

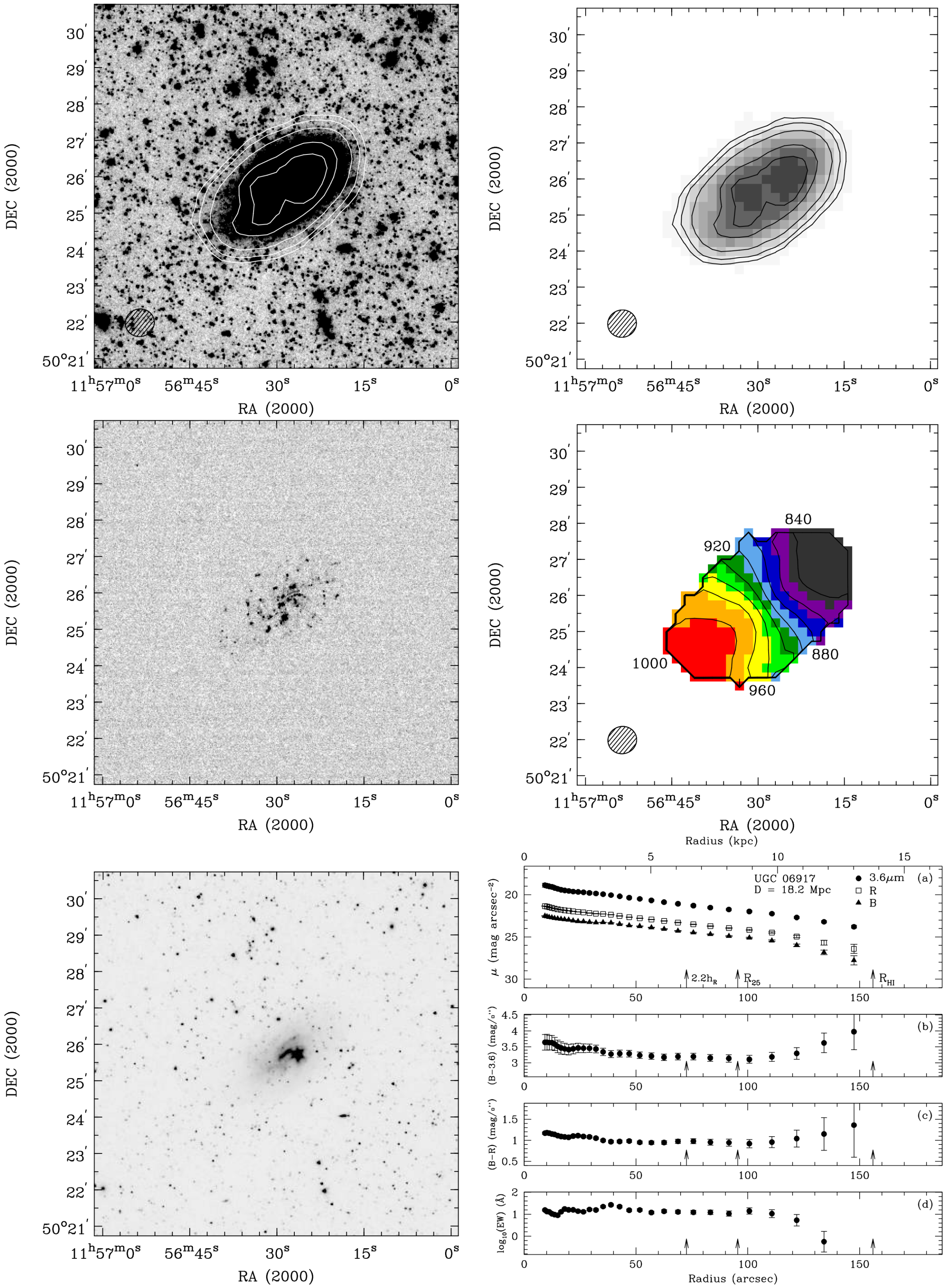

Figure A8. **UGC 06917:** Panels same as in Fig. A1. The first low-resolution VLA H I contour represents a column density of 10^{20} atoms cm^{-2}.

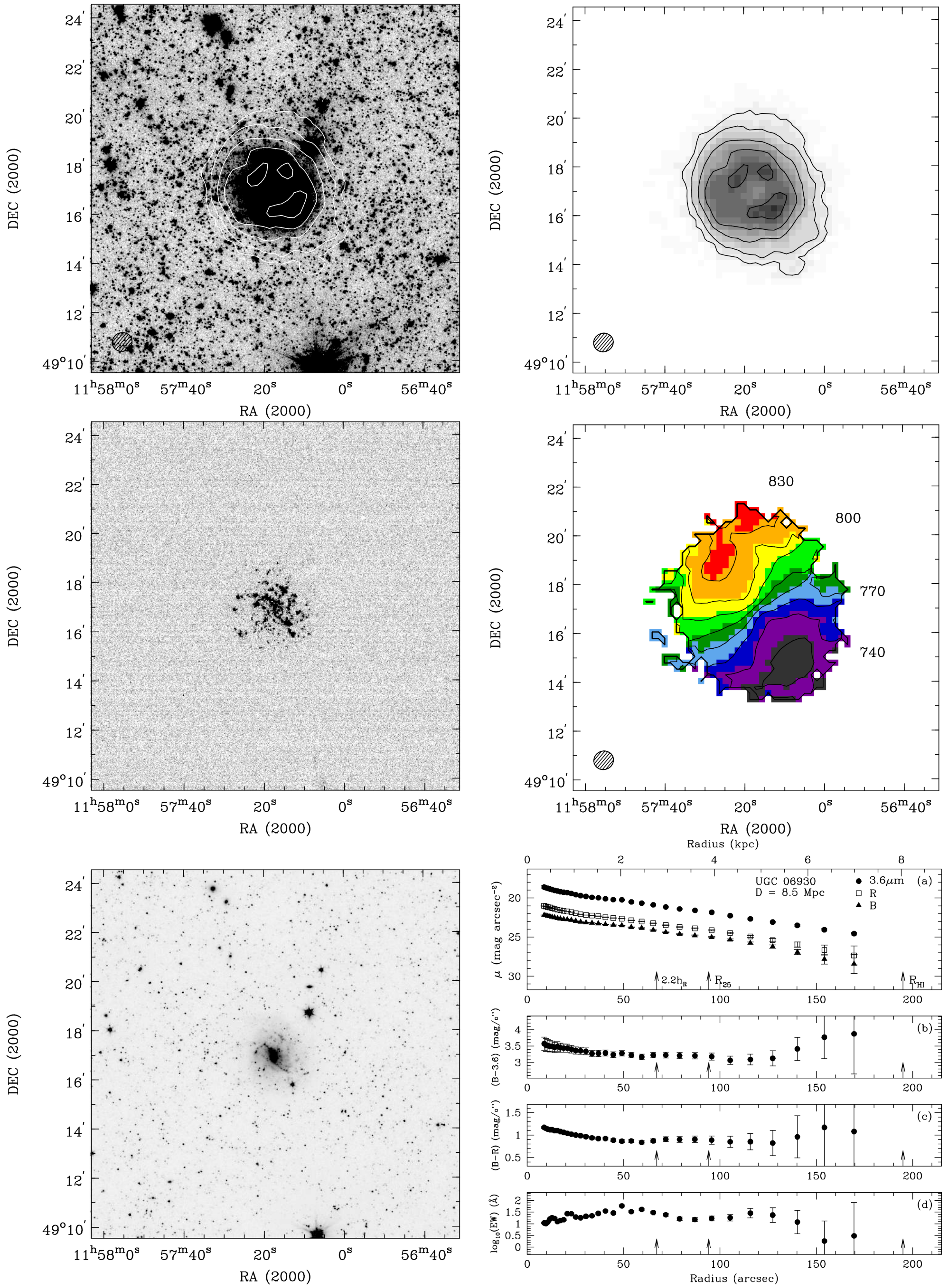

Figure A9. **UGC 06930:** Panels same as in Fig. A1. The first low resolution VLA H I contour represents a column density of 10^{20} atoms cm^{-2}.

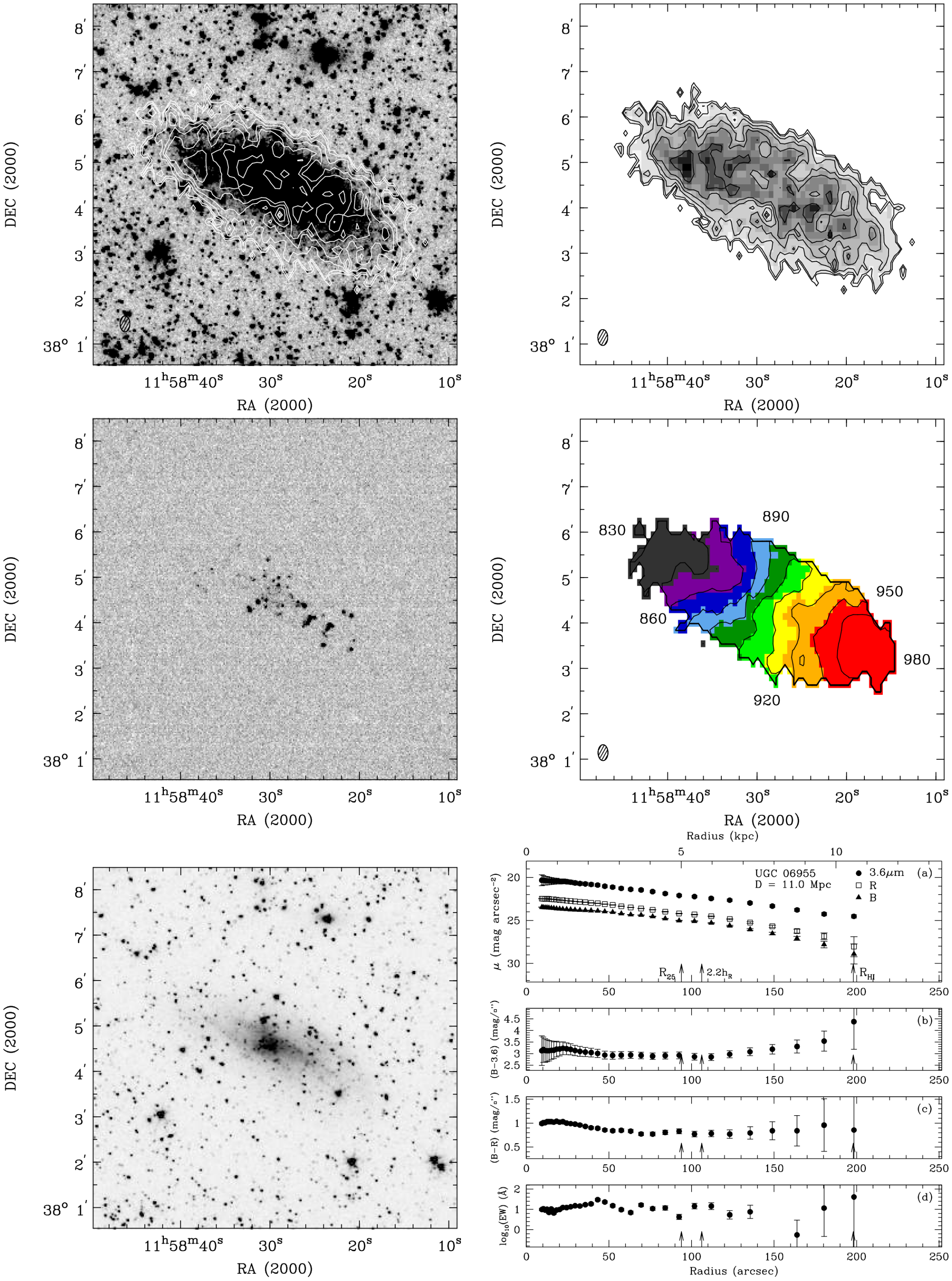

Figure A10. **UGC 06955:** Panels same as in Fig. A1. The first WSRT H I contour represents a column density of 10^{20} atoms cm^{-2}.

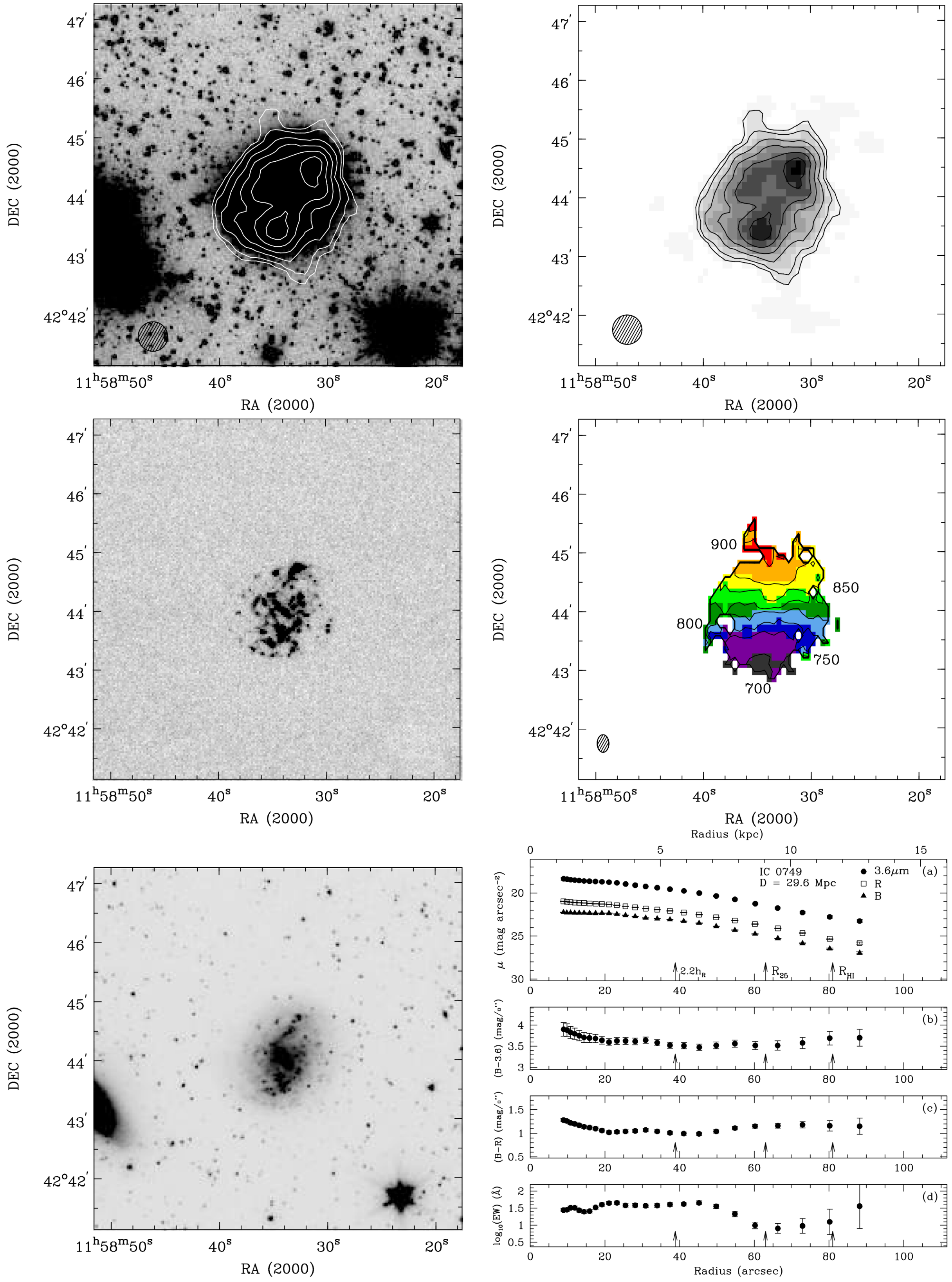

Figure A11. **IC 0749:** Panels same as in Fig. A1. The first medium resolution (30 × 30 arcsec) WSRT H I contour represents a column density of 10^{20} atoms cm^{-2}. The velocity field is made from the full resolution cube (18 × 12 arcsec).

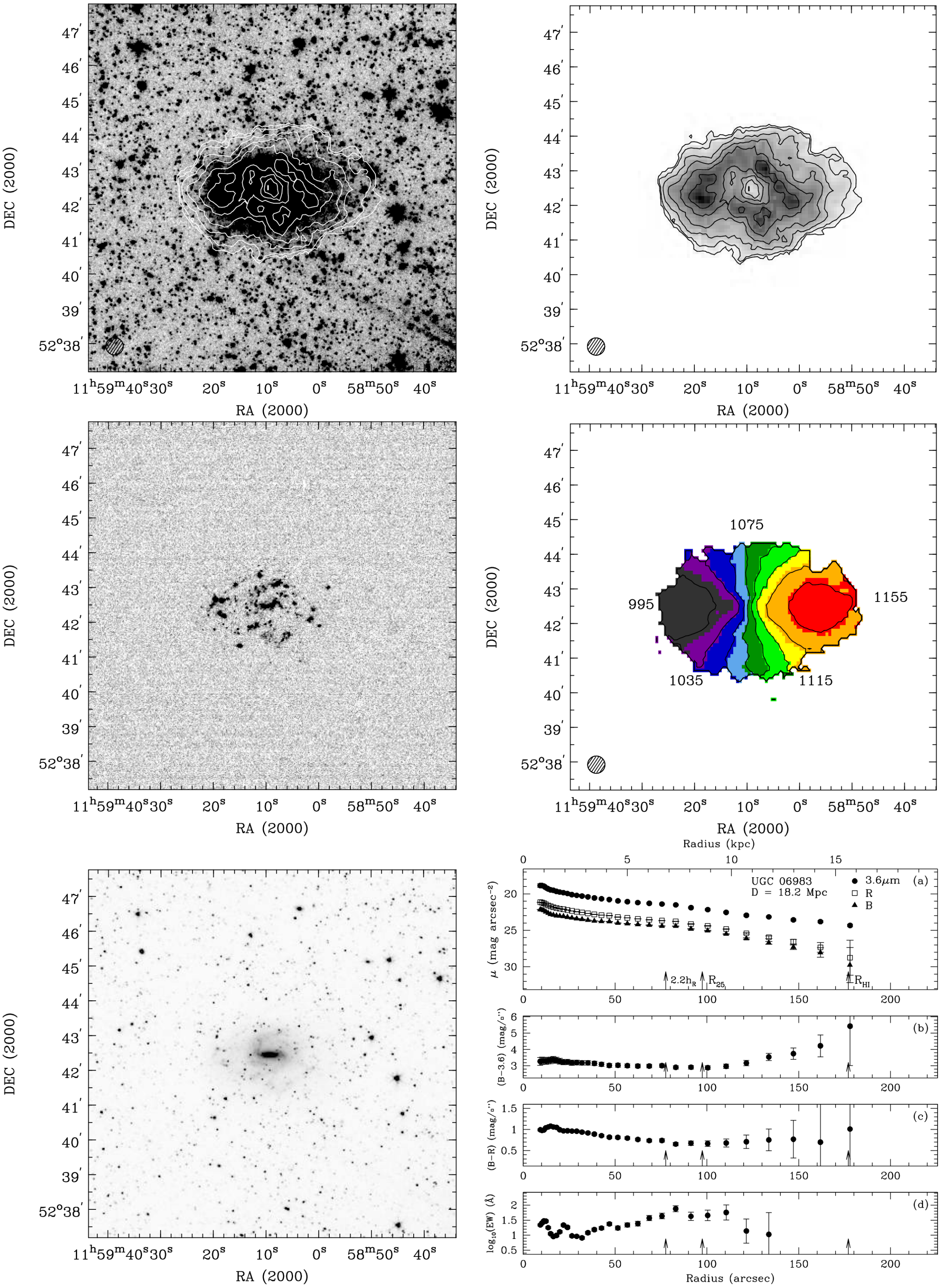

Figure A12. **UGC 06983:** Panels same as in Fig. A1. The first medium-resolution WSRT H I contour represents a column density of 10^{20} atoms cm^{-2}.

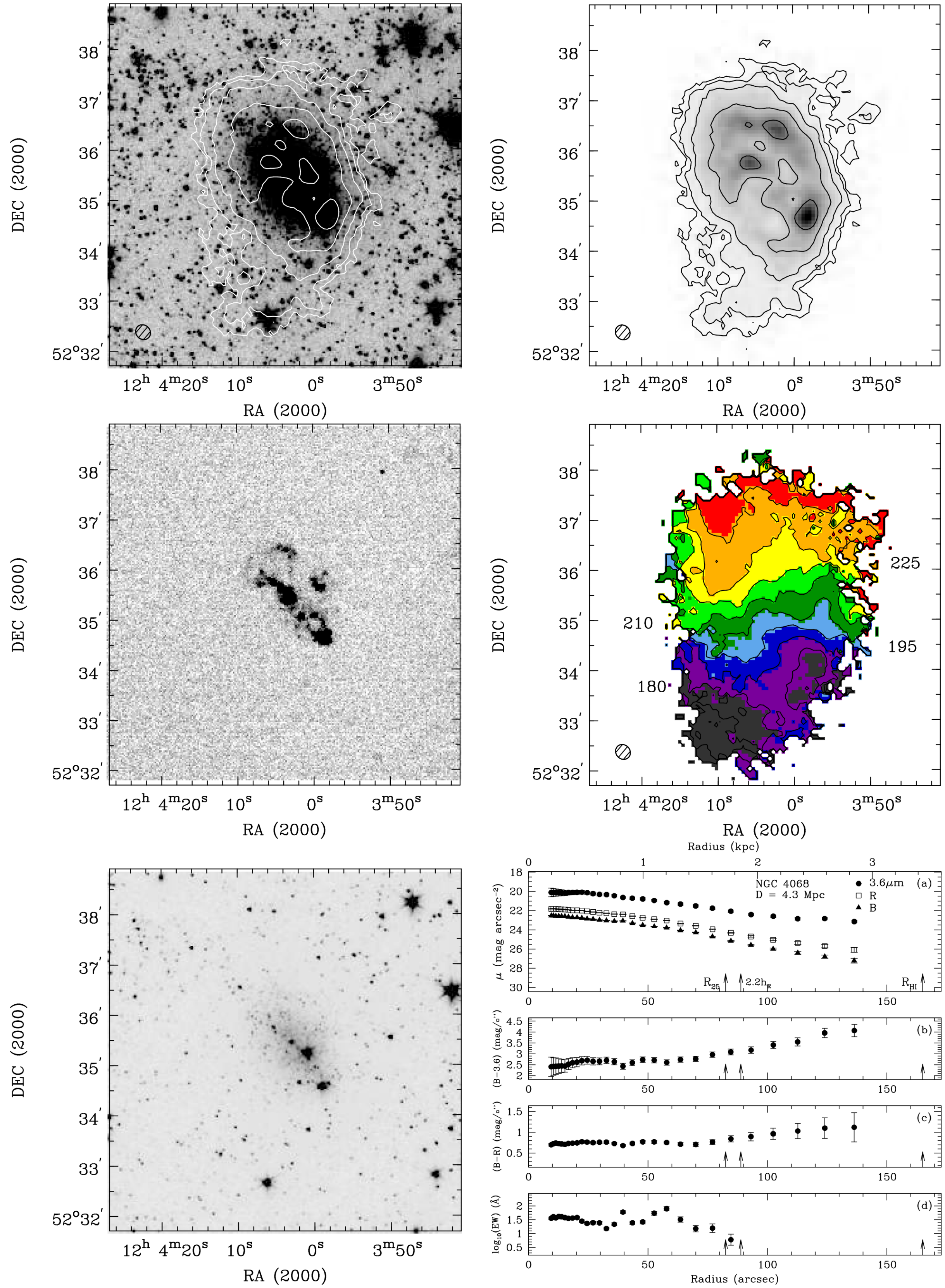

Figure A13. **NGC 4068:** Panels same as in Fig. A1. The first low-resolution VLA H I contour represents a column density of 10^{20} atoms cm^{-2}.

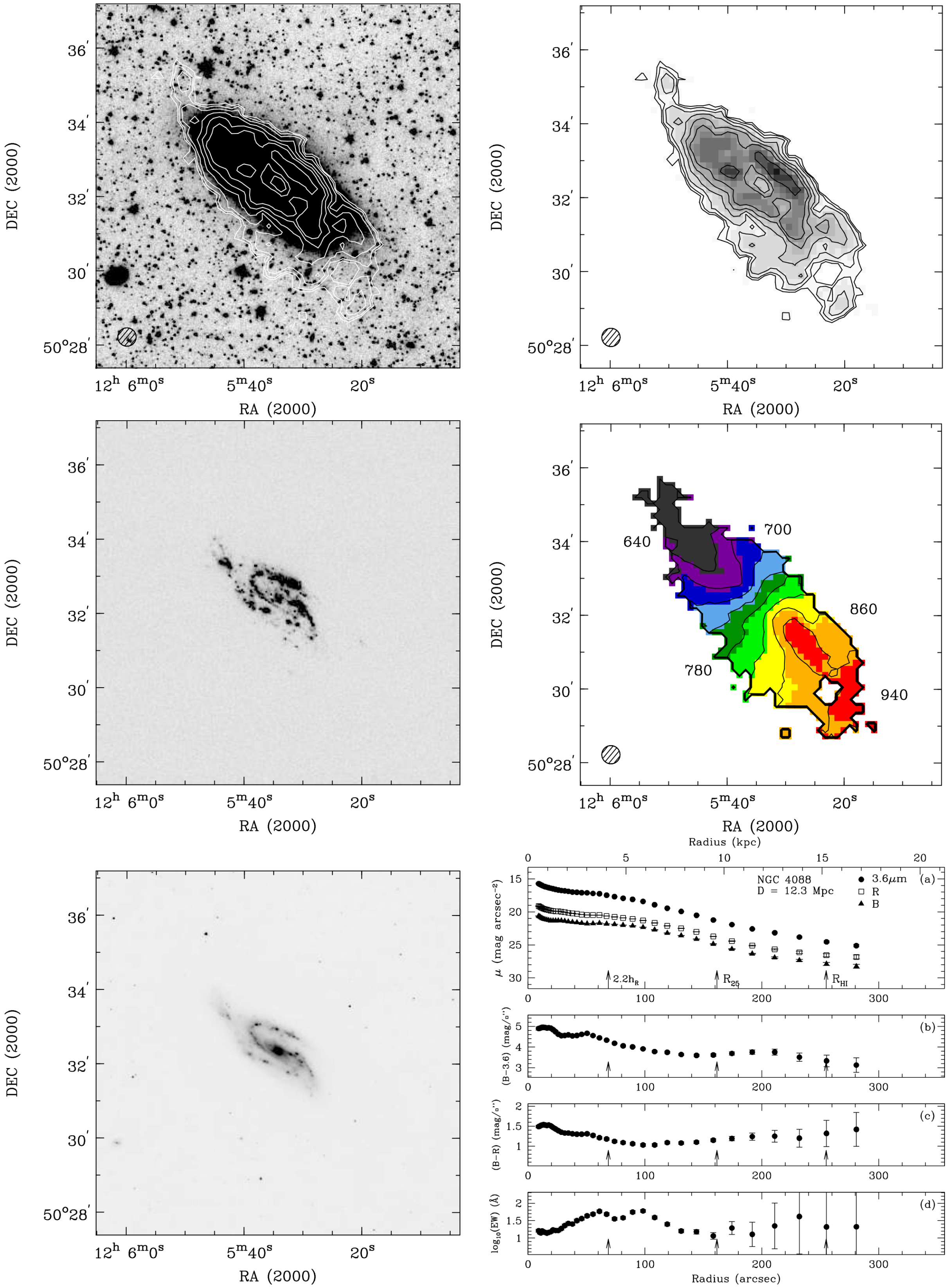

Figure A14. **NGC 4088:** Panels same as in Fig. A1. The first WHISP 30 arcsec resolution H I contour represents a column density of 10^{20} atoms cm^{-2}.

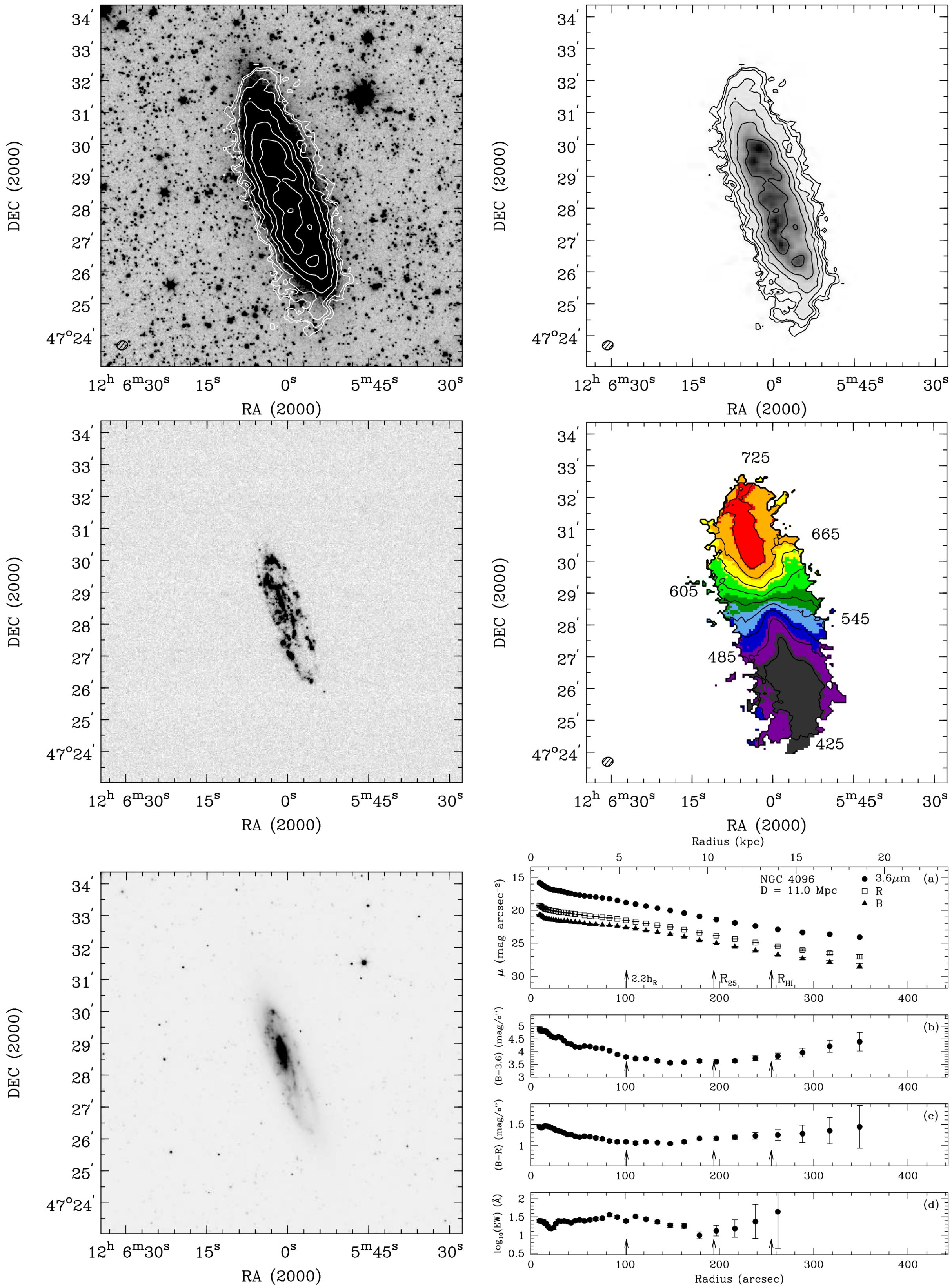

Figure A15. **NGC 4096:** Panels same as in Fig. A1. The first low-resolution VLA H I contour represents a column density of 10^{20} atoms cm^{-2}.

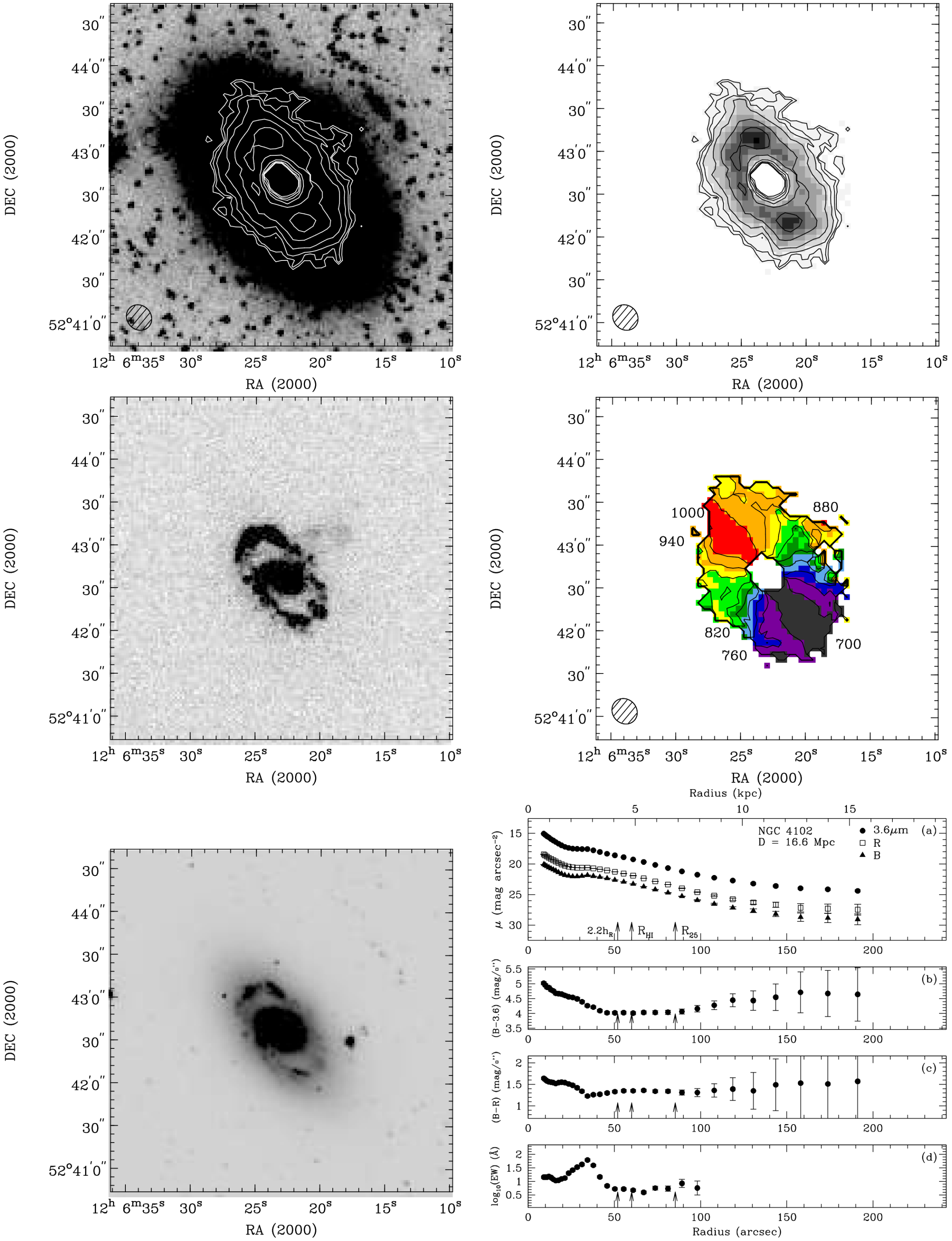

Figure A16. **NGC 4102:** Panels same as in Fig. A1. The first low-resolution VLA H I contour represents a column density of 4×10^{19} atoms cm^{-2}.

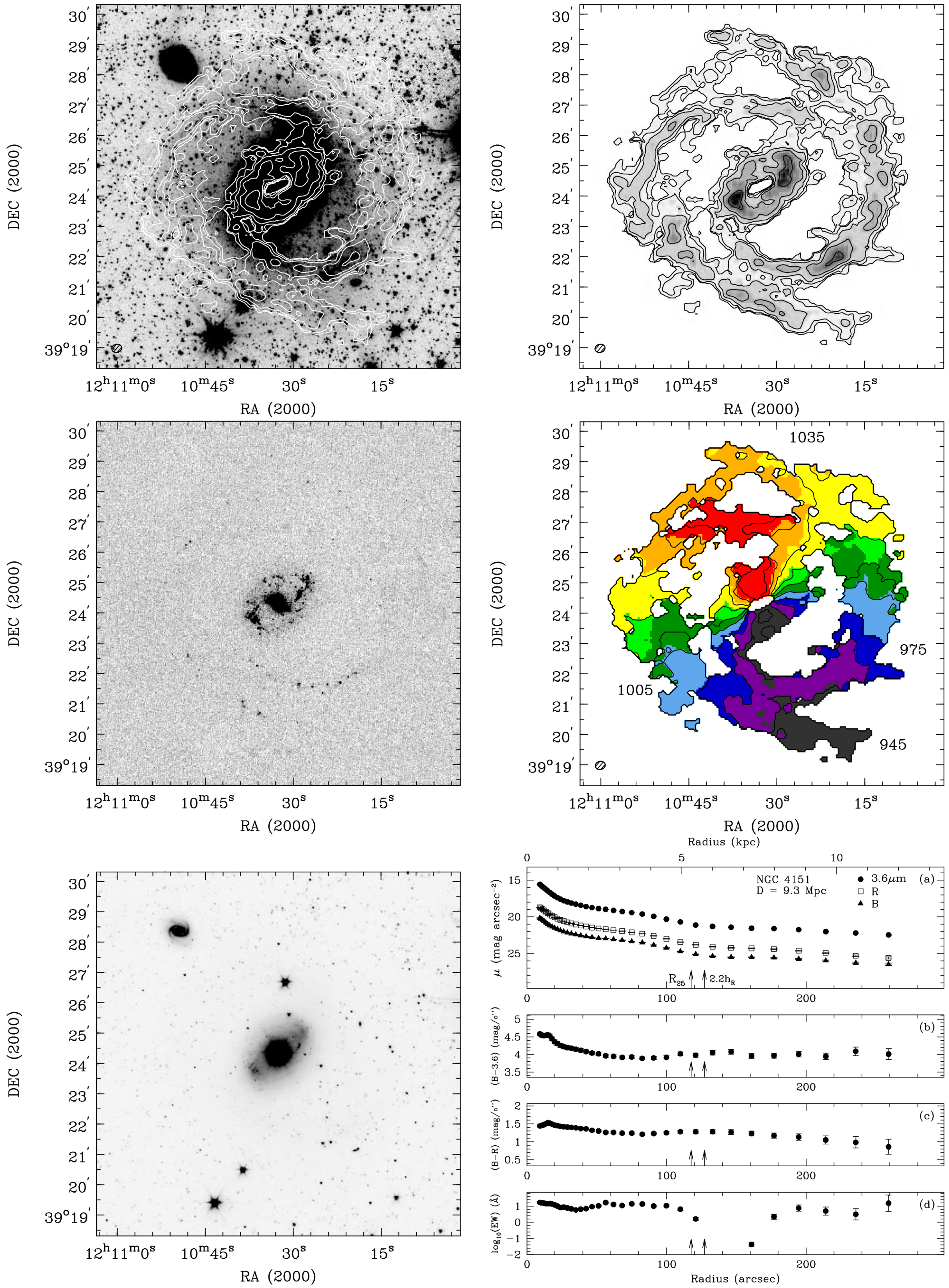

Figure A17. **NGC 4151** Panels same as in Fig. A1. The first tapered resolution VLA H I contour represents a column density of 5×10^{19} atoms cm^{-2}.

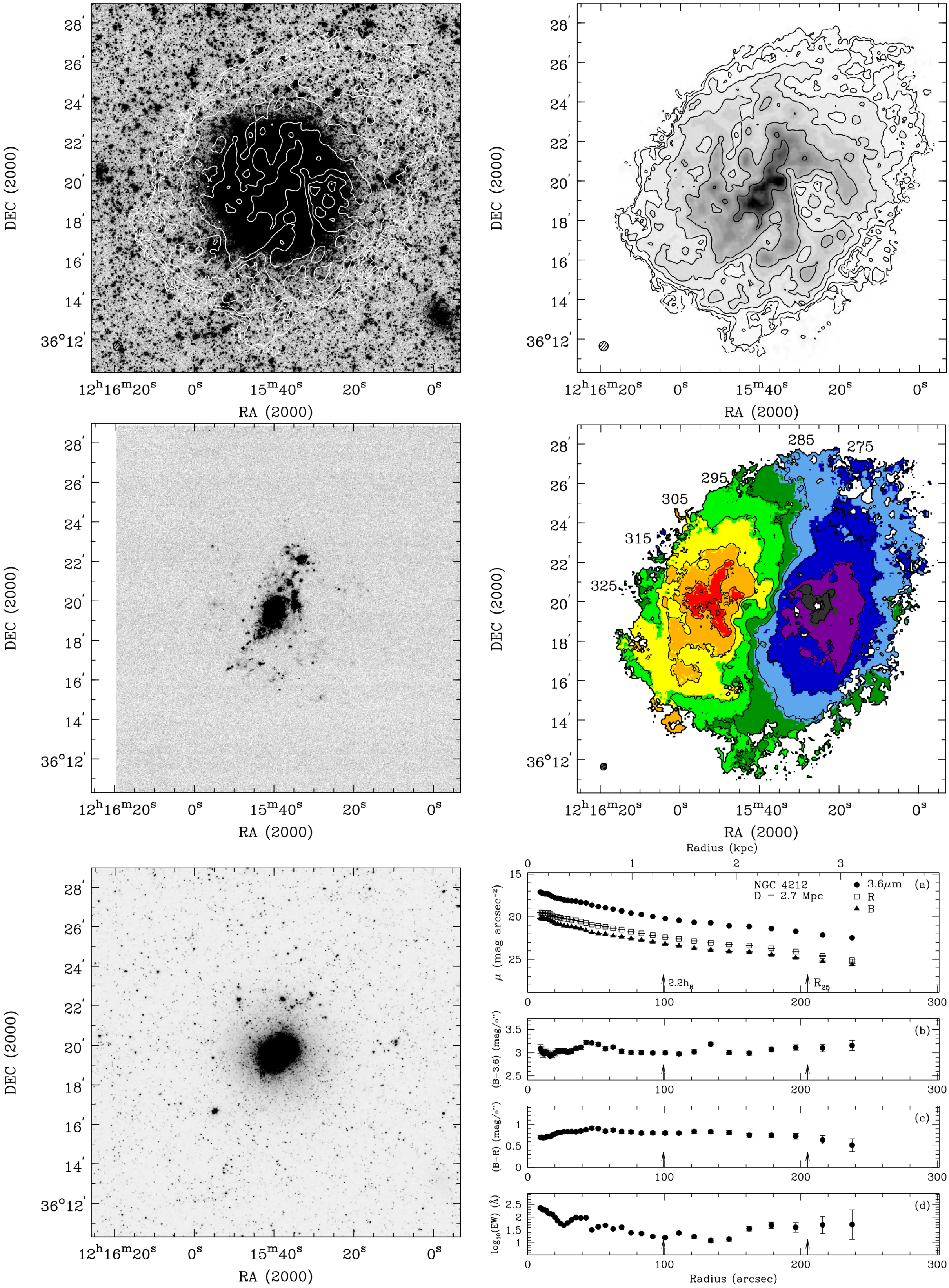

Figure A18. **NGC 4214:** Panels same as in Fig. A1. The first tapered resolution VLA H I contour represents a column density of 5 × 10^{19} atoms cm^{-2}. The velocity field is made from the low-resolution cube.

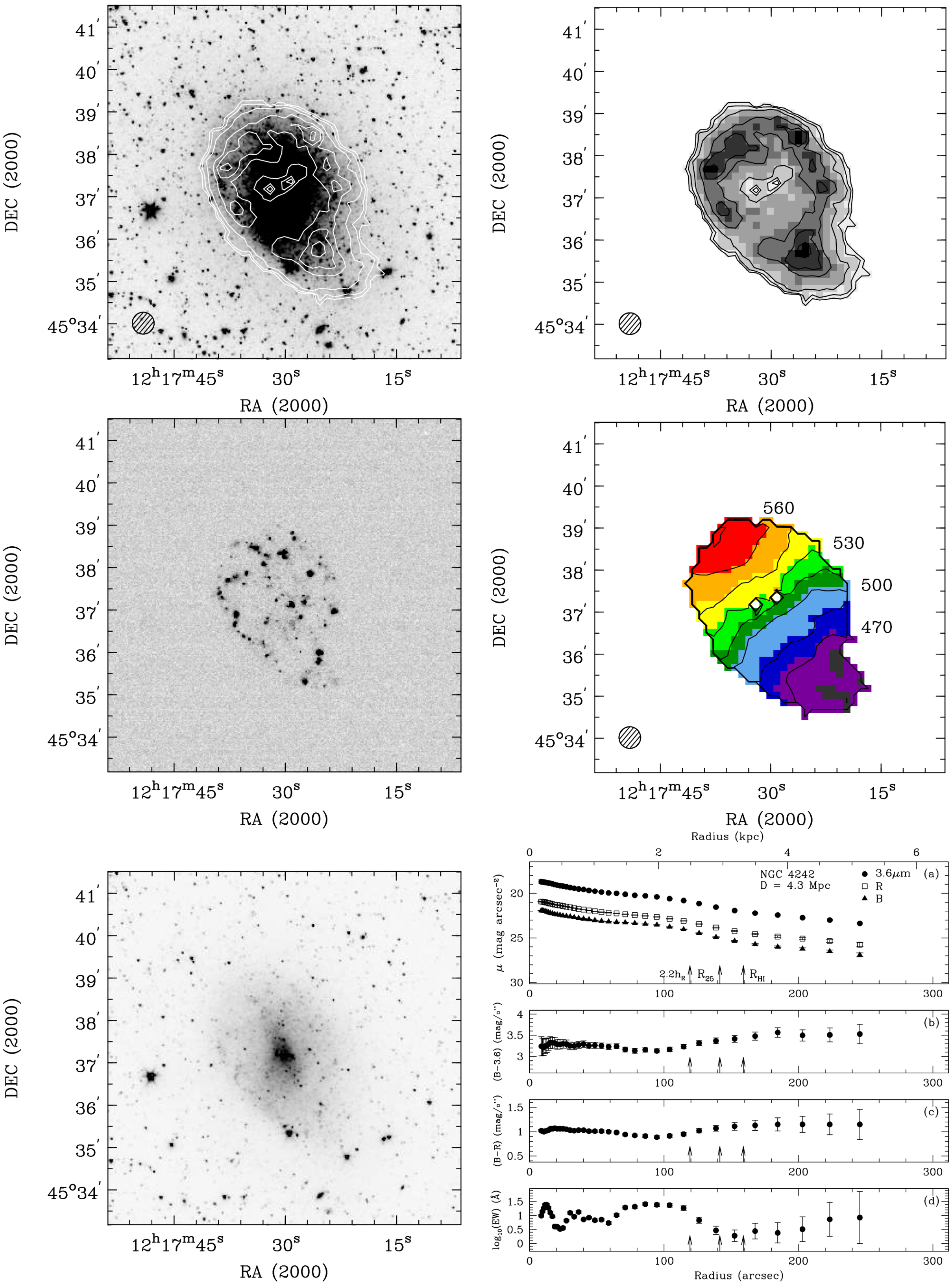

Figure A19. **NGC 4242:** Panels same as in Fig. A1. The first WHISP 30 arcsec resolution H I contour represents a column density of 10^{20} atoms cm^{-2}.

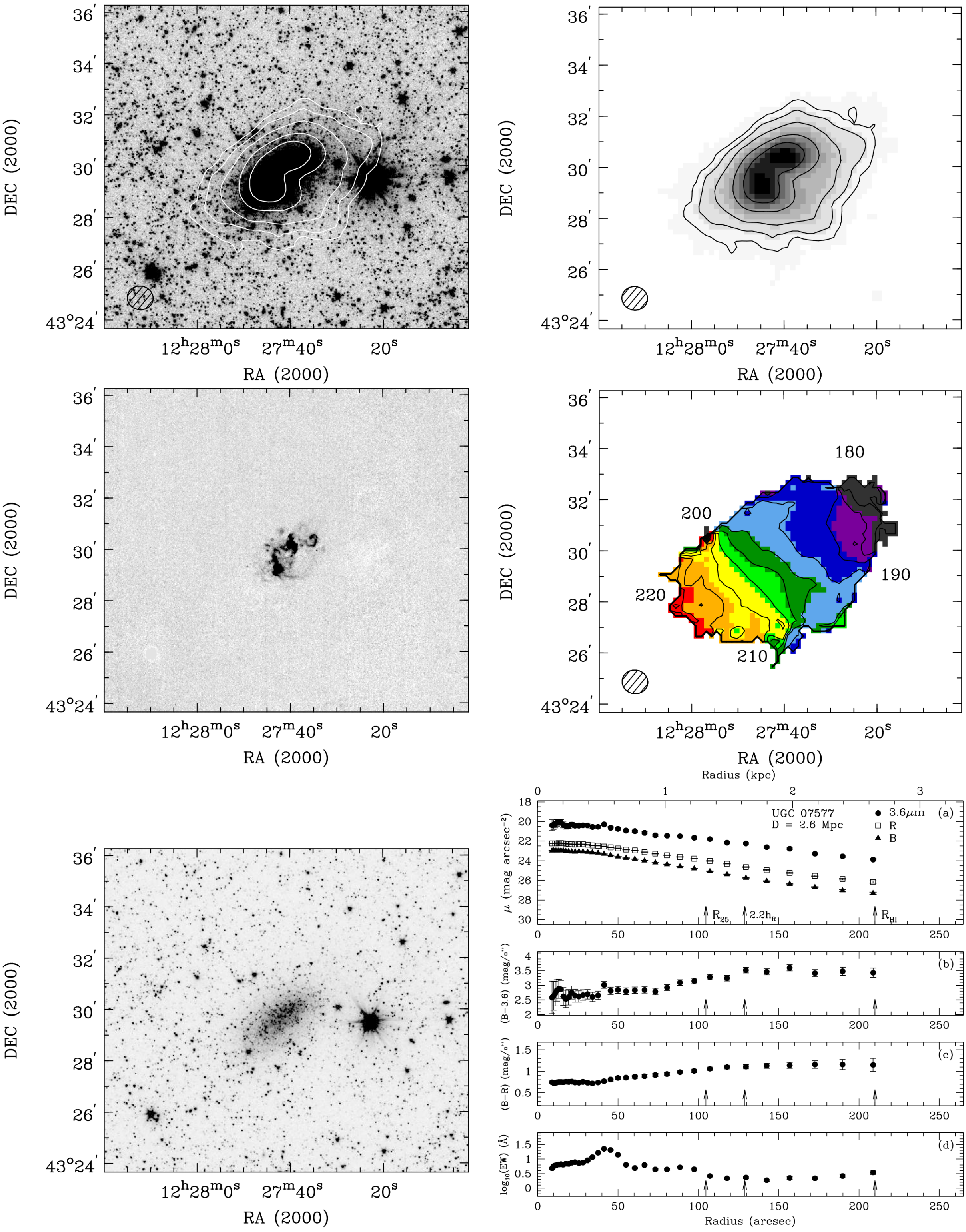

Figure A20. **UGC 07577:** Panels same as in Fig. A1. The first low-resolution VLA H I contour represents a column density of 5 × 10^{19} atoms cm^{-2}.

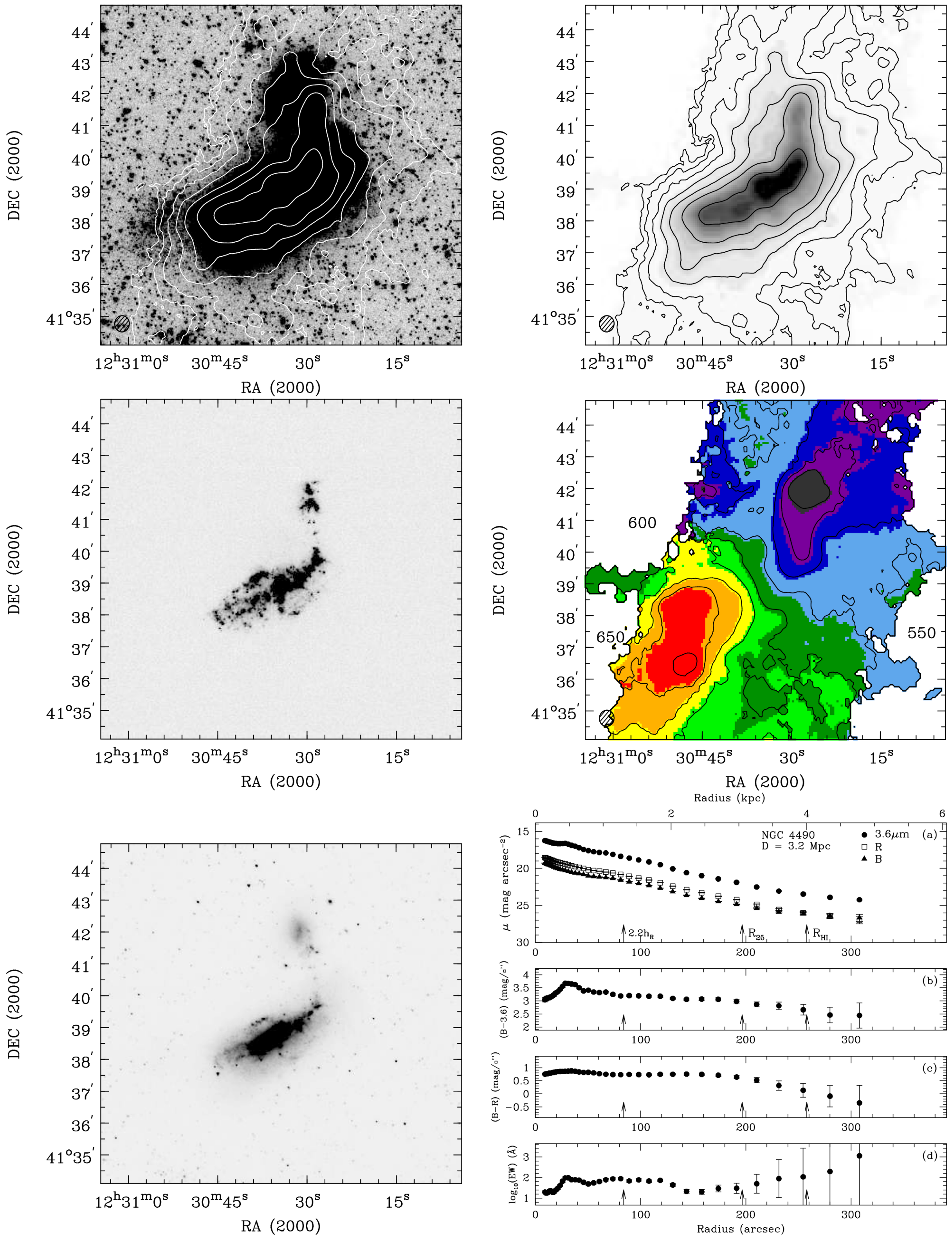

Figure A21. **NGC 4485 and NGC 4490:** Panels same as in Fig. A1. The first low-resolution VLA H I contour represents a column density of 10^{20} atoms cm^{-2}.

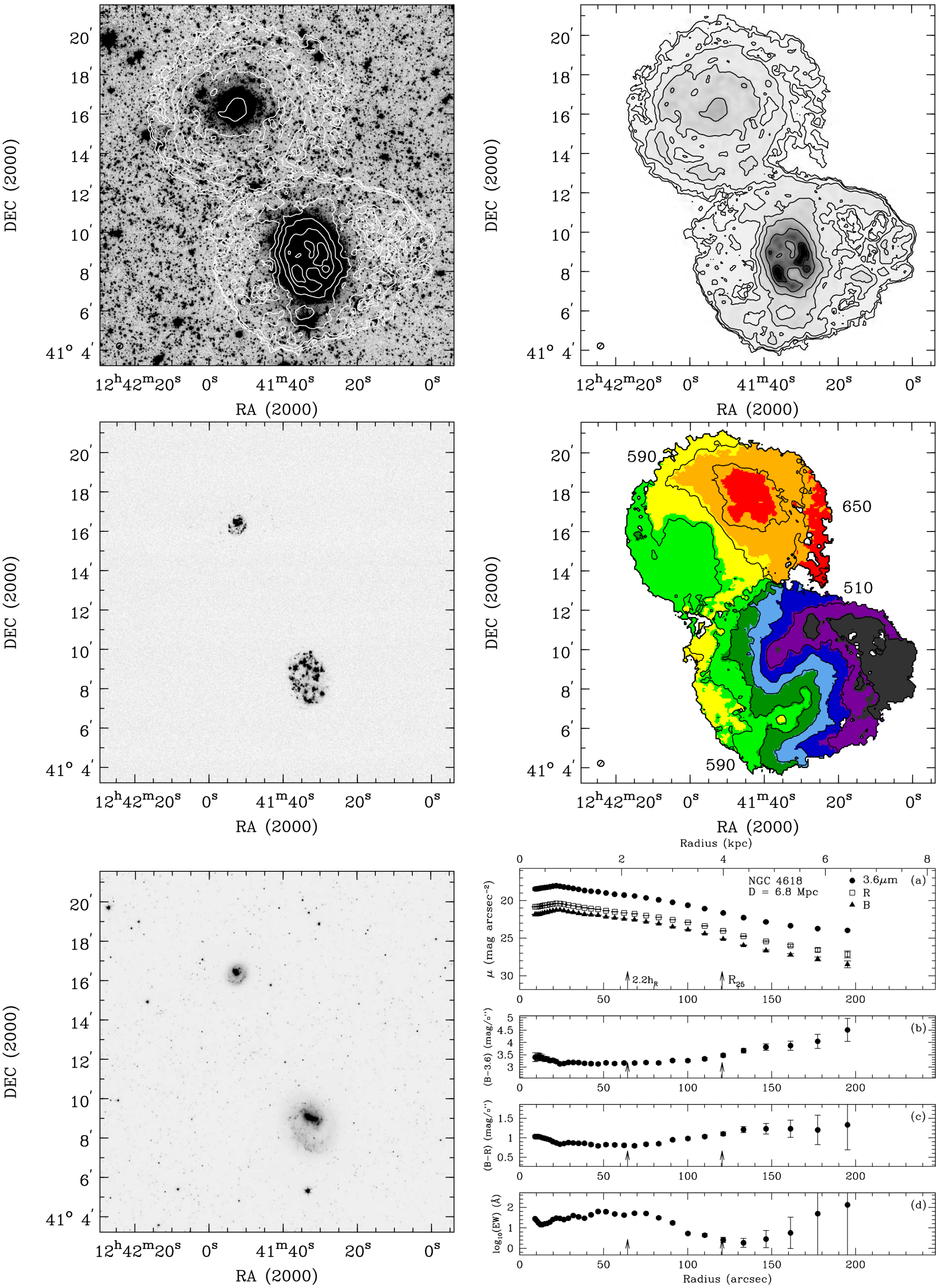

Figure A22. **NGC 4618:** Panels same as in Fig. A1. The first tapered resolution VLA H I contour represents a column density of 4×10^{19} atoms cm^{-2}.

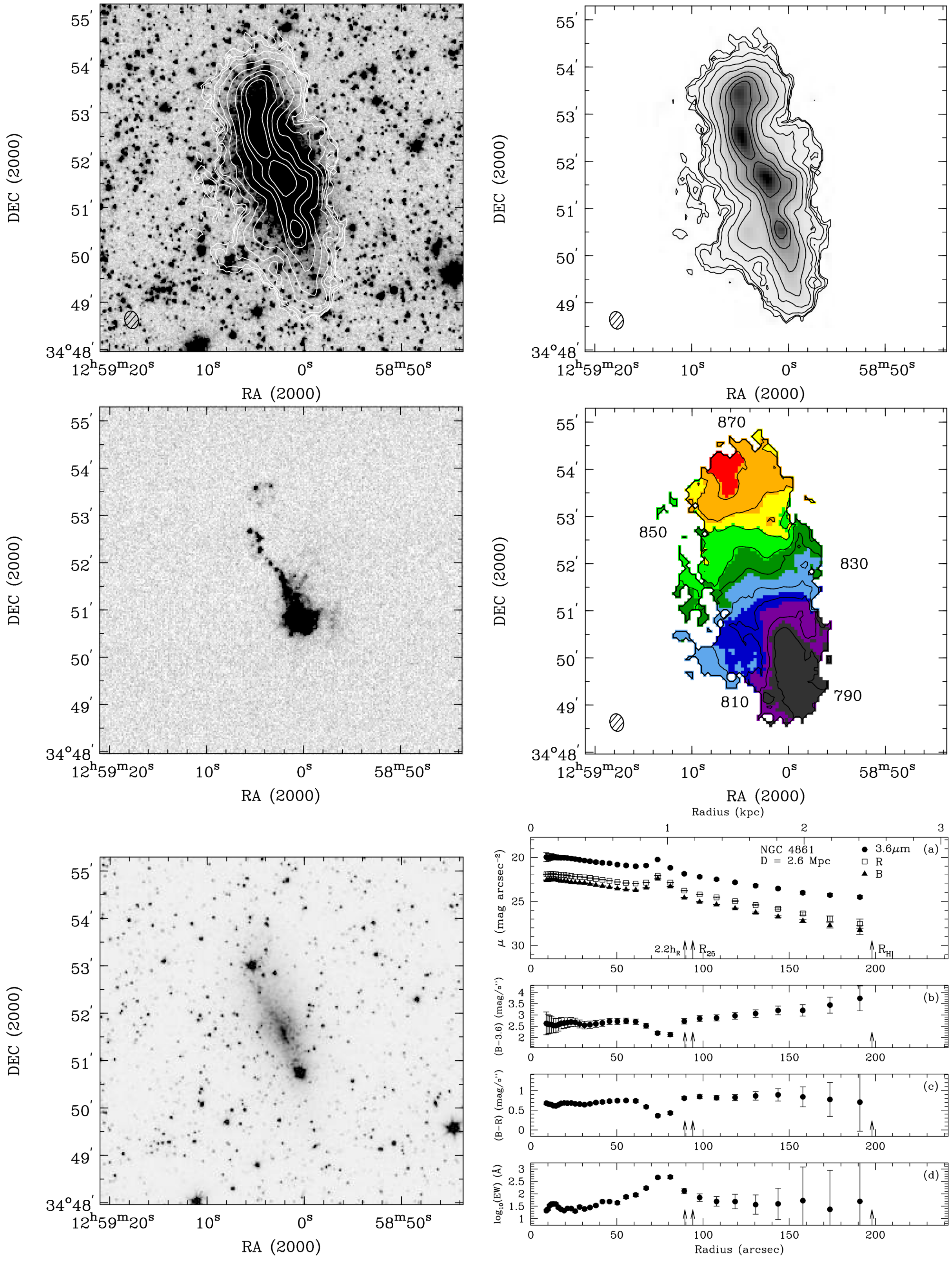

Figure A23. NGC 4861: Panels same as in Fig. A1. The first low-resolution VLA H I contour represents a column density of 2×10^{19} atoms cm^{-2}.

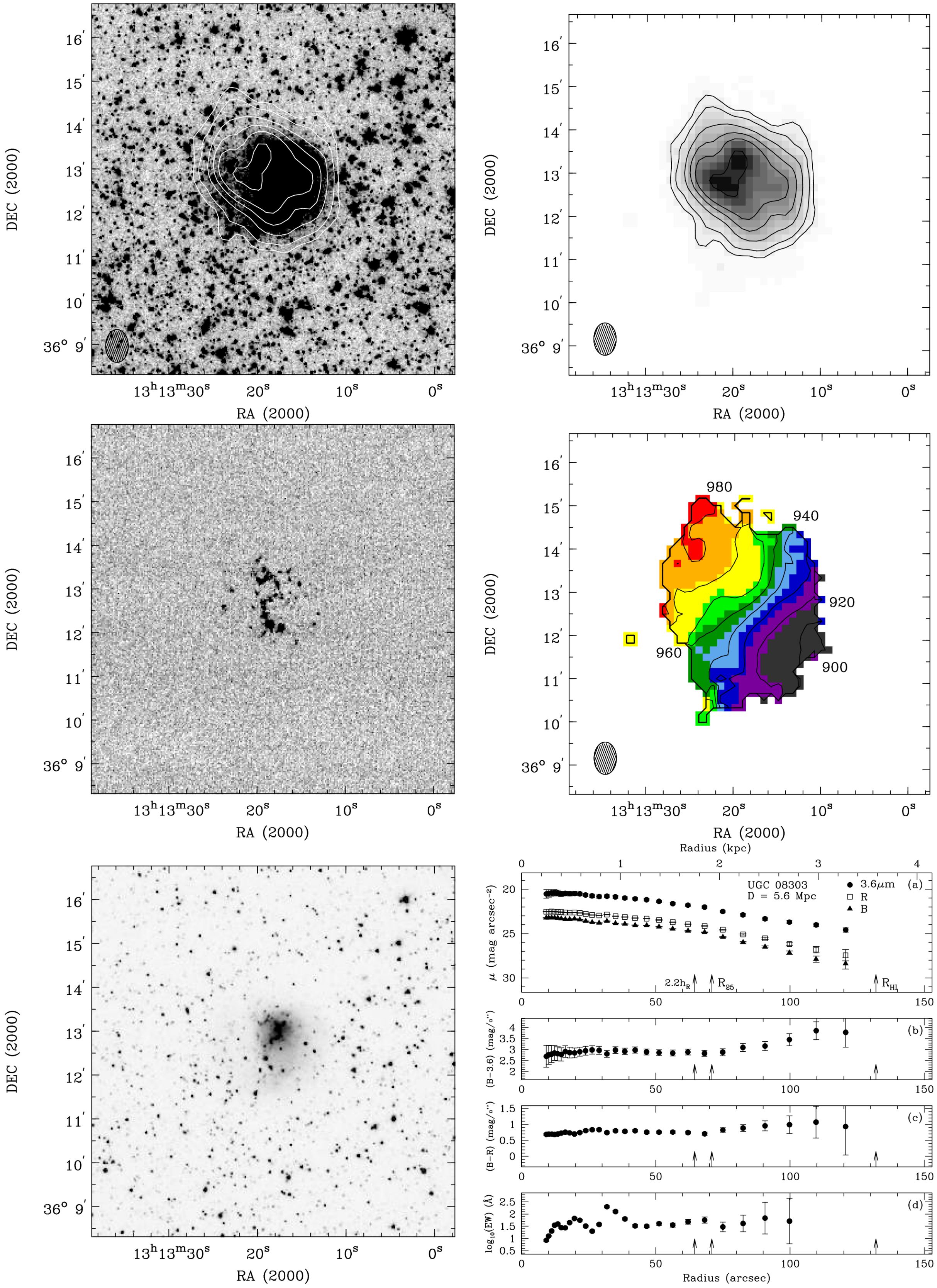

Figure A24. **UGC 08303:** Panels same as in Fig. A1. The first WHISP 30 arcsec resolution H I contour represents a column density of 2×10^{20} atoms cm^{-2}.

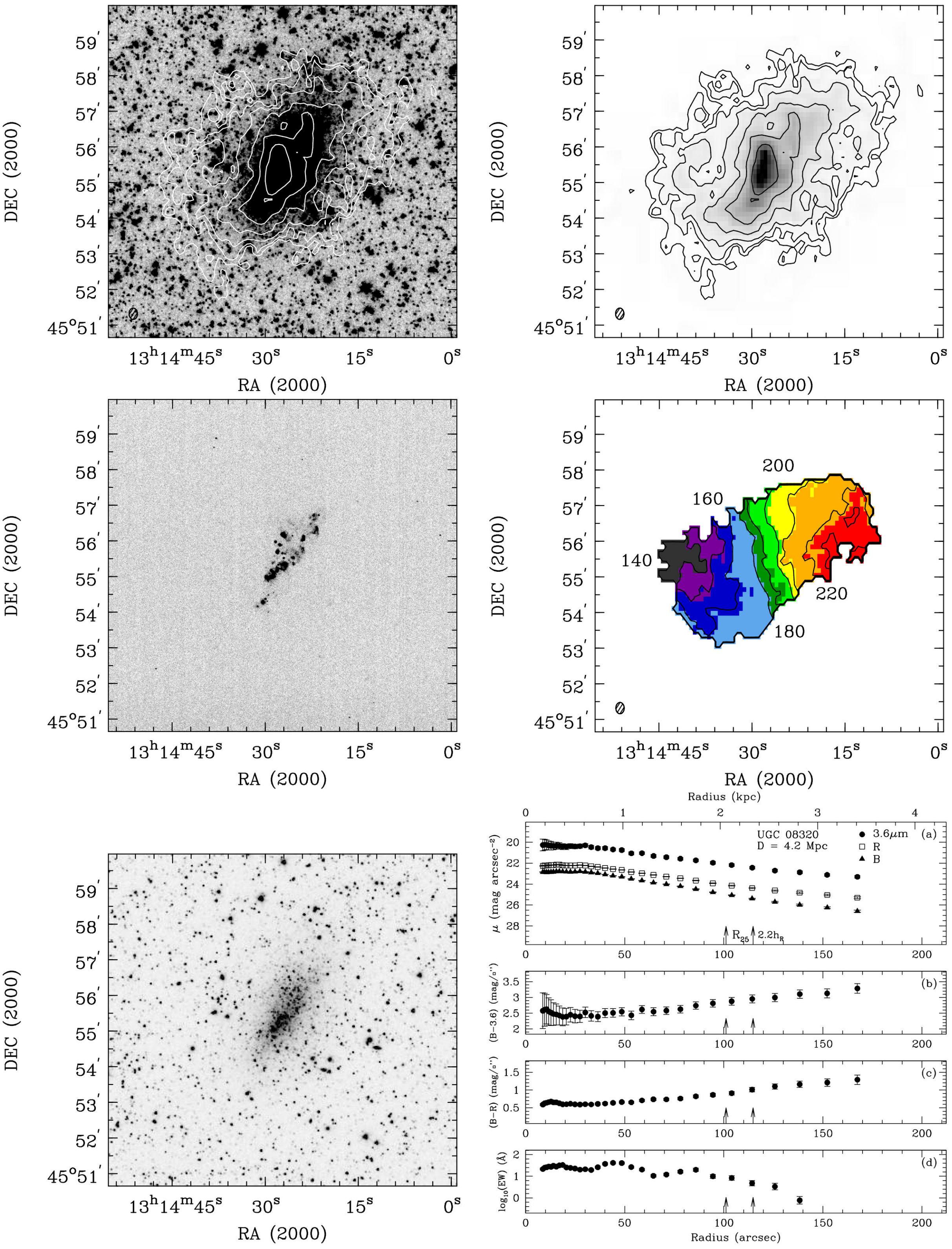

Figure A25. **UGC 08320:** Panels same as in Fig. A1. The first WSRT H I contour represents a column density of 10^{20} atoms cm^{-2}.

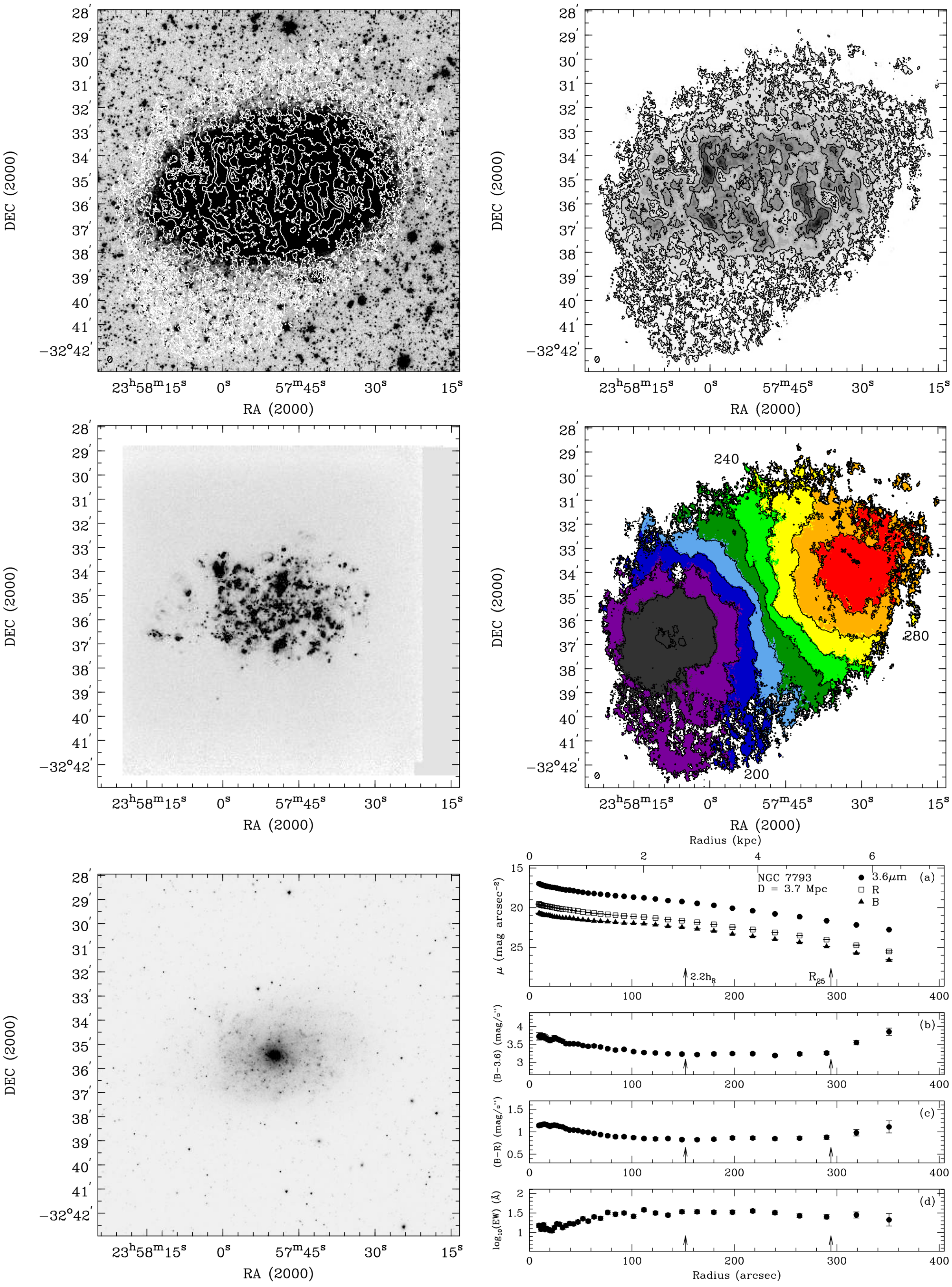

Figure A26. NGC 7793: Panels same as in Fig. A1. The first low-resolution VLA H I contour represents a column density of 10^{20} atoms cm^{-2}.

The H I kinematics were additionally studied by Schwarz (1985). The molecular gas dynamics have also been investigated by Pott et al. (2004) and Krips et al. (2005) who cite evidence for tidal interaction and gas accretion. Due to its complex and peculiar nature, NGC 3718 is not well-suited for rotation curve decomposition analysis and was not included in the kinematic analysis.

A4 NGC 3729

NGC 3729 is a nearby companion galaxy to NGC 3718 detected in the same VLA observations. The distribution of H I does not extend as far as the low surface brightness stellar disc, especially along the minor axis. There is a stellar bar oriented nearly along the minor axis of the galaxy that connects to a ring-like structure associated with a bump in the EW profile and decrease in the $B - R$ colour profile. Bright regions of bar-induced shocked ionized gas are visible in the H α image, as well (Usui, Saitō & Tomita 2001).

The kinematic signature of the bar is visible in the ionized gas velocity field. The true dynamics of NGC 3729 are likely more complex than the azimuthally averaged circular velocities estimated from the tilted ring analysis. Usui et al. (2001) found evidence for counter-rotating orbits in slit-spectroscopy oriented along the bar. Nonetheless, the estimated circular rotational velocities derived from the ionized gas velocity field are well described by the shape of the modelled stellar contribution to the observed rotation curve.

A5 NGC 3893

The WHISP H I data for NGC 3893 has an irregular morphology and connects to the nearby companion NGC 3896 to the south-east. Despite the obvious interaction, the velocity field of NGC 3893 reveals a regularly rotating H I disc about 2 arcmin in size. The H I velocity field was described using tilted rings with varying PA from ∼345° to ∼385°, in agreement with Verheijen & Sancisi (2001). The H α image and EW profile suggest recent star formation in the central arcmin of the disc. Ionized gas kinematics derived from the Hα emission in NGC 3893 were acquired by the Gassendi H α survey of SPirals (GHASP), and are in agreement with the H I derived rotation curve (e.g. Spano et al. 2008).

A6 NGC 3949

The H I content of NGC 3949 as revealed by the 30 arcsec resolution WHISP data extends slightly farther than the low surface brightness stellar disc. The neutral and ionized gas velocity fields are fairly regular with no kinematic signature of a central barred potential. The ionized and neutral gas rotation curves are in good agreement. As in Verheijen & Sancisi (2001), we find that the rotation curve derived from the receding side of the H I velocity field rises faster than the approaching side. Stellar and ionized gas emission-line kinematics from Ganda et al. (2006a) show global rotation in agreement with the H I.

A7 UGC 06900

Processed H I data for UGC 06900 was acquired from the LITTLE THINGS survey and is originally published in Hunter et al. (2012). The H I distribution is clumpy with a radial extent similar to the low surface brightness stellar disc. There is little evidence of recent star formation based on the lack of H α emission. The H I kinematics indicate a slowly rising rotation curve, consistent with other dwarf galaxies in the EDGES kinematic sample. Decomposing the rotation curve under the maximum stellar disc assumption results in an unusually large M/L of 3.2 and baryonic-to-total mass fraction at $2.2h_\mathrm{R}$ that jumps to 0.61 from 0.13 under the fixed M/L = 0.5 assumption. The mass distribution of UGC 06900 under the fixed M/L assumption is entirely dark-matter-dominated, in agreement with the detailed decomposition performed by Oh et al. (2015).

A8 UGC06917

Archival VLA D configuration observations (project code AV237) of UGC 06917 display a smooth, extended H I distribution with evidence of solid body rotation in the velocity field. Narrow-band H α imaging shows star formation distributed along what appear to be faint, tightly wound spiral arms. The H I derived rotation curve rises slowly to maximum velocity around 115 km s^{-1} in good agreement with the rotation curve presented in Verheijen & Sancisi (2001) derived from WSRT H I observations. Under the fixed stellar M/L assumption, the dark matter contribution to the observed rotation curve dominates, but the observed kinematics allow a maximum stellar M/L of 1.6, increasing $M_\mathrm{bary}/M_\mathrm{tot}$ at $2.2h_\mathrm{R}$ from 30 to 81 per cent.

A9 UGC 06930

H I observations of UGC 06930 come from the same archival VLA D configuration data as UGC 06917. Like UGC 06917, UGC 06930 has an extended H I disc with star formation regions distributed throughout the stellar disc. The outer edges of the H I velocity field along the major axis appear to be warped slightly. H I observations from the WSRT for UGC 06930 are additionally available as part of WHISP and Verheijen & Sancisi (2001). Like UGC 06917, the rotation curve of UGC 06930 can be decomposed assuming a dark-matter-dominated mass distribution with fixed stellar M/L = 0.5, or a maximal stellar contribution with M/L = 1.8.

A10 UGC06955

H I moment maps of UGC 06955 from the WSRT were kindly provided by Adrick Broeils. Details about the observations can be found in Broeils (1992). Narrow-band Hα imaging reveals numerous discrete star-forming regions distributed preferentially on the receding western half of the disc. The neutral and ionized gas kinematics agree well with each other, except for a small deviation towards higher velocities for the ionized gas in the very centre. The rotation curve is slowly rising with the gas disc being the primary baryon contribution at large radii under the fixed stellar M/L assumption.

A11 IC 0749

IC 0749 is part of an interacting pair with IC 0750, which is visible to the south-east. The processed H I data from the WSRT is published in Verheijen & Sancisi (2001), and was kindly made available by Marc Verheijen. The PA of the major axis of H I disc appears to be slightly offset from the PA of the low-surface brightness stellar disc major axis, but aligns well with the star-forming disc as seen in the narrow-band H α image. The H I rotation curve is similar in shape to low-mass dwarf galaxies in that it rises slowly to the last measured point. It differs, however, in its decomposition by being baryon-dominated out to three disc scale lengths under the fixed stellar M/L assumption, rather than being dark-matter-dominated at all measured radii.

A12 UGC 06983

UGC 06983 is a late-type spiral with a small stellar bar oriented along its major axis. The WSRT H I data provided by Marc Verheijen and published in Verheijen & Sancisi (2001) shows a small depression in the centre of the column density map, but no distorted isovelocity contours in the velocity field, which could have been a kinematic signature of the bar. There is no obvious signature of bar's influence in the SparsePak ionized gas velocity field, either. The ionized gas rotation curve rises more steeply than the H I rotation curve in the centre, but they are in agreement beyond 30 arcsec. The model gas rotation curve overtakes the model stellar rotation curve beyond R_{25} in the fixed stellar M/L decomposition, but the stellar contribution to the observed dynamics is dominant under the maximum disc assumption with a stellar M/L = 3.1.

A13 NGC 4068

New VLA C configuration observations presented in Fig. A13 show that the H I is distributed farther out than the stellar light with an extension down towards the south-east. NGC 4068 is a well-studied starburst system (e.g. McQuinn, Mitchell & Skillman 2015) with a TRGB distance estimate of 4.3 Mpc (Karachentsev et al. 2006). The ionized gas in this starbursting dwarf appears turbulent in the narrow-band H α image and in the SparsePak velocity field. Alternatively, the H I velocity field shows clear signs of rotation, but with an asymmetric morphology and PA that is offset from the stellar distribution. The rotation curve derived from these new VLA observations extends to farther radii than the ones derived in Lelli, Verheijen & Fraternali (2014) and Swaters et al. (2009) from the same WSRT data. The shape of the rotation curve beyond 100 arcsec is questionable due to the asymmetric distribution of H I on the approaching and receding sides, and was not fit during the decomposition. The ionized gas rotation curve was found to be dominated by turbulent motions and was not included in the decomposition. The mass distribution was found to be baryon-dominated out to nearly four disc scale lengths under the fixed stellar M/L = 0.5 assumption.

A14 NGC 4088

H I observations from WHISP reveal an asymmetric H I disc with regular rotation. The position–velocity diagram in Verheijen & Sancisi (2001) demonstrates the kinematic asymmetry between the approaching and receding sides of the H I disc. The uneven distribution of the H I gas appears to follow the distribution of bright star-forming regions, as seen in the narrow-band H α image. The stellar distribution also features a positive EW gradient and negative colour gradients from the centre out to the star-forming disc. The small spiral companion, NGC 4085, lies about 10 arcmin to the south.

The ionized gas kinematics do not appear to follow the neutral gas kinematics. It is not clear why there is a discrepancy between the shapes of the ionized and neutral gas rotation curves, but it is likely a combination of low spatial resolution effects in the H I data and non-circular-ionized gas motions in the centre. The general shape of the ionized gas rotation curve is reflected in the model stellar rotation curve in the decomposition, but the magnitude of the ionized gas circular rotational velocities cannot be matched by the stellar disc contribution without overestimating the flat portion of the H I rotation, which is in agreement with Verheijen & Sancisi (2001).

A15 NGC 4096

NGC 4096 is similar to NGC 4088 in the asymmetric nature of the distribution of star formation. The highest density of stellar light and star-forming regions in the narrow-band H α image is noticeably offset from the centre of the H I and low surface brightness stellar disc. This lopsidedness is reflected in the galaxy kinematics, as well. Using WHISP data, van Eymeren et al. (2011) measured the H I rotation curve for the approaching and receding sides separately and found that the receding side rotation curve peaks at rotation velocities ∼50 km s^{-1} greater than the approaching side. We find a similar effect in the H I data from new VLA C configuration observations shown in Fig. A15, but with a smaller discrepancy. The final shape of azimuthally averaged rotation curve is well described by the stellar disc model rotation curve. CO observations from Sofue et al. (1997) additionally show an asymmetric molecular gas distribution with a rotating ring of radius 20 arcsec.

A16 NGC 4102

New VLA C configuration observations of NGC 4102 shown in Fig. A16 reveal a ring of H I with inhomogeneous column density around the circumference. The H I observations newly presented here are more sensitive than previous WSRT observations, which were not able to recover the spatially congruent ring of H I emission (Verheijen & Sancisi 2001). There is a strong nuclear radio continuum source (Condon et al. 1982) that causes the H I to appear in absorption across the full velocity width of the line emission.

The ring structure seen in H I emission also appears in the narrow-band H α image and high surface brightness stellar distribution. Radial photometry profiles show a sharp decrease in colour and corresponding increase in EW at the radius of the star-forming ring (∼35 arcsec). Within the outer star-forming ring, the nucleus of NGC 4102 is host to a stellar bar, LINER, and starburst. High-resolution infrared observations of the nucleus have revealed a high concentration of central mass with a highly extincted rotating disc or ring of star formation 4.3 arcsec in diameter (Beck, Lacy & Turner 2010). We additionally detect an outflow of ionized gas in the narrow-band H α image. A detailed analysis of the outflow from SparsePak IFS observations will be presented in Braun et al. (in preparation).

Kinematic signatures of the copious amount of activity occurring in this galaxy were detected in SAURON IFS observations by Ganda et al. (2006b). While the central stellar kinematics appeared well behaved with purely circular motion, the ionized gas kinematics as traced by H β and [O III] turned out to be much more complex. The ionized gas kinematics measured in the lower resolution, larger field-of-view SparsePak data do not appear as complicated as the SAURON observations. The derived ionized gas rotation curve overlaps with and agrees well with the H I rotation curve.

The ionized and neutral gas rotation curves are flat with a maximum circular rotational velocity near 180 km s^{-1}. The radial extent of the H I, however, is confined well within the stellar disc and is not enough to probe beyond the baryon-dominated centre of the mass distribution. Therefore, NGC 4102 is not included in the final decomposition analysis due to our inability to constrain the dark matter contribution.

A17 NGC 4151

NGC 4151 is one of the most well-studied galaxies in the EDGES kinematic sample due to the powerful active galactic nucleus (AGN) at its centre (Ho et al. 1997). The H I data are from combined archival VLA B and C configuration observations. The B configuration data were originally published in Mundell & Shone (1999) and Mundell et al. (1999), and the C configuration in Pedlar et al. (1992). The B configuration data were channel averaged by two to match the spectral resolution of the C configuration data before combination. Similar to NGC 4102, H I absorption can be seen against the strong continuum emission of the central AGN. The structure and kinematics of the neutral gas are complex, featuring an inner ring surrounding a stellar bar and an outer ring that is connected to the inner H I at both ends of the major axis. The structure and kinematics of the H I from WHISP observations are additionally studied by Noordermeer et al. (2005).

The ionized gas emission follows the neutral gas with faint discrete H II regions distributed along the outer ring. The SparsePak kinematics are dominated by circular rotation, in agreement with the SAURON [O III] and H β-ionized gas kinematics observed in Dumas et al. (2007). The ionized and neutral gas rotation curves agree where they overlap, but are both highly uncertain due to the face-on nature of the galaxy and the incongruity of the H I emission. Therefore, NGC 4151 was not included in the final decomposition analysis.

A18 NGC4214

NGC 4214 is a nearby (2.7 Mpc; Drozdovsky et al. 2002) dwarf irregular galaxy and well-studied starbursting system (e.g. McQuinn et al. 2015). It has an extended H I disc and bright ionized gas emission with an irregular morphology. The H I data were processed from archival VLA B, C, and D configuration observations acquired as part of the THINGS survey (Walter et al. 2008). The closed isovelocity contours in the H I velocity field indicate that the neutral gas disc is warped. Similar to THINGS, the inclination angle of the H I disc was found to be too face-on for the tilted ring analysis to yield reliable results, so NGC 4214 was not included in the decomposition analysis. More detailed kinematic modelling of the H I kinematics in NGC 4214 are provided in Lelli et al. (2014) and Swaters et al. (2009).

Due to the low inclination angle, we did not target NGC 4214 for ionized gas kinematics with SparsePak. Furthermore, Fabry-Perot H α observations as part of the GHASP survey revealed no evidence for rotation (Epinat, Amram & Marcelin 2008b). Swaters et al. (2009) also notes that the H I has large velocity dispersions in the centre and appears to be counterrotating relative to the outer H I disc.

A19 NGC 4242

NGC 4242 is an SABdm galaxy with an irregular morphology. H I observations from WHISP reveal higher levels of H I column density distributed in a ring around a high surface brightness stellar concentration at the centre. The H I also shows an extension to the south-west on the approaching side of the galaxy that does not appear to overlap with a stellar population, although the same feature can be seen in the ionized gas of the narrow-band H α image. The EW profile displays numerous bumps and wiggles where the annuli encounter discrete H II star-forming regions in the H α image.

The straight isovelocity contours in the H I velocity field are indicative of solid body rotation. The SparsePak ionized gas velocity field shows similar kinematics, but is more irregular. Despite this, the ionized and neutral gas kinematics both result in slowly rising rotation curves that agree well where they overlap. An H I rotation curve was additionally derived from the WHISP data in Swaters et al. (2009). Our kinematic parameters and resulting H I rotation curve are in excellent agreement. H α kinematics from the GHASP survey presented in Garrido, Marcelin & Amram (2004) provide confirmation that ionized and neutral gas rotation curves are well matched. Fixing the stellar M/L to 0.5 results in a dark-matter-dominated mass decomposition for NGC 4242.

A20 UGC 07577

UGC 07577 is a nearby (2.6 Mpc; Dalcanton et al. 2009) dwarf irregular galaxy. Archival VLA D configuration data were originally published in Hunter et al. (1998) as part of a mosaic around the large irregular galaxy NGC 4449. The H I disc roughly follows the exponential stellar distribution. The highest column density regions appear to overlap with the brightest ionized gas emission in the narrow-band H α image.

Unlike the ionized gas kinematics that are dominated by turbulent motions, the neutral gas velocity field indicates clear solid body rotation. However, the H I rotation curve only reaches circular velocities on the order of 20 km s^{-1} at the last measured point. The same result has been found by numerous other studies using WSRT (e.g. Tully et al. 1978; Stil & Israel 2002; Swaters et al. 2009) and VLA (e.g. Ott et al. 2012) observations. Swaters (1999) additionally found that the rotation curve of UGC 07577 could be decomposed without the need for dark matter and suggest that it could have formed in tidal debris around NGC 4449 (e.g. Barnes & Hernquist 1992). UGC 07577's proximity to NGC 4449 (projected distance ∼40 kpc) and the existence of the tidal streams around NGC 4449 make UGC 07577 a strong tidal dwarf galaxy candidate (e.g. Hunter, Hunsberger & Roye 2000). In light of this, UGC 07577 is not included in the kinematic analysis.

A21 NGC 4485 and NGC 4490

It is apparent from their H I distributions that NGC 4485 and NGC 4490 are interacting. The smaller irregular galaxy, NGC 4485, is connected to the larger spiral, NGC 4490, by a faint stellar stream with a few bright H II regions. The H I observations used here appear originally in Clemens, Alexander & Green (1998), where it is suggested that the morphology of the H I can be explained by a galactic-scale bipolar outflow driven by supernovae in NGC 4490.

The H I emission roughly associated with NGC 4490 does show signs of rotation in its velocity field, so an attempt was made to fit titled ring models. The best-fitting kinematic model roughly agrees with that presented in Viallefond, Allen & de Boer (1980) from low-resolution WSRT observations, but reaches a larger V_{flat} of 100 km s^{-1} versus their ∼85 km s^{-1}. Our derived V_{flat} results in an LTFR distance estimate of 3.2 Mpc, which conflicts with the TRGB-derived distance estimate of 8.9 Mpc to NGC 4485 (Tully et al. 2013). The interaction between the two galaxies creates too much uncertainty for the kinematics, so NGC 4485 and NGC 4490 are not included in the final analysis.

A22 NGC 4618

NGC 4618 forms a physical pair with the galaxy NGC 4625 to the north-east and is likely interacting with the other system, as both galaxies exhibit tidal features in their stellar distributions. The H I data used here has been processed from archival B, C, and D configuration VLA observations. C configuration data from project code AW618 were published in Bush & Wilcots (2004) and again in Kaczmarek & Wilcots (2012) with the B configuration observations added. Older C and D configuration observations from project codes AO108 and AO101, respectively, were additionally processed and combined with the AW618 data.

During the data processing, it was discovered that the 4IF mode observational set-up for each data set was done incorrectly and required each channel in the higher frequency bandpass to be shifted by 3.4 kHz ($<1\,\mathrm{km\,s^{-1}}$) relative to their true observed frequencies. This ultimately affects 18 channels of H I line emission from 452–540 $\mathrm{km\,s^{-1}}$ in the final data cube used for analysis. The velocity field created from this cube was compared to the one in WHISP to confirm that the $<1\,\mathrm{km\,s^{-1}}$ offset had no discernible effect on the resulting kinematics.

The combined data sets result in the highest sensitivity H I observations published for these galaxies and recover more diffuse emission than what is presented in Bush & Wilcots (2004) and Kaczmarek & Wilcots (2012), or for the WSRT observations in van Moorsel (1983). Tilted ring modelling of the H I velocity field of NGC 4618 proved to be challenging. The twisted isovelocity contours indicate a severe warp, which can be described through a nearly 100° drop in PA from 200° to 100°. We were unable to reproduce the shapes of the rotation curves presented in Bush & Wilcots (2004), Kaczmarek & Wilcots (2012), or van Moorsel (1983) and instead find a rising rotation curve. The H α rotation curve from GHASP shows solid body rotation out to 150 arcsec (Epinat et al. 2008a). Due to the complexity involved in the dynamical modelling and the likely interacting nature of NGC 4618, it is excluded from the final analysis.

A23 NGC4861

NGC 4861 is classified as both a barred Magellanic spiral and blue compact dwarf galaxy at a TRGB-estimated distance of 10.0 Mpc (Tully et al. 2013). It contains an extremely bright star-forming H II region, I Zw 49, located ~80 arcsec south-west of the photometric centre. NGC 4861 has the bluest colour, largest EW, and highest SFR of any galaxy in the EDGES kinematic sample due to this massive star-forming complex. The signature of this region is visible in all the radial profiles as a bump in surface brightness and EW and a dip in $B - 3.6$ and $B - R$ colour.

The H I data used in this analysis comes from VLA archival C configuration observations published in Thuan, Hibbard & Lévrier (2004). Archival D configuration data from the VLA were additionally used to trace the rotation curve to a larger radius. The D configuration observations published in Wilcots, Lehman & Miller (1996) include a detection of a small H I cloud to the east of NGC 4861. This same cloud is detected in the C configuration data when smoothed to 35 arcsec resolution (Thuan et al. 2004). There is no stellar counterpart to this H I emission. A detailed kinematic analysis of NGC 4861 is available in van Eymeren et al. (2009). The shape and amplitude of the rotation curve derived here is in good agreement with van Eymeren et al. (2009). Decomposing the rotation curve suggests that the stellar disc is nearly maximal at inner radii. The gas contribution to the observed dynamics overtakes the stellar contribution near the peak of the observed rotation curve (~150 arcsec).

A24 UGC 08303

H I observations from WHISP reveal that the neutral gas follows the stellar distribution, which features a high surface brightness concentration offset from the centre of the low surface brightness disc. The H α image shows an irregular distribution of H II regions. UGC 08303 was detected in the H I observations of NGC 5033 (Richards et al. 2016), but was outside the primary beam half-power width. A slowly rising rotation curve was derived from the H I velocity field. There is some asymmetry between the approaching and receding sides, as can additionally be seen in the position–velocity diagram in Stil & Israel (2002). As is common for rotation curves of this shape, the mass distribution of UGC 08303 was found to be dark-matter-dominated at all radii under the fixed stellar M/L = 0.5 assumption and stellar-disc-dominated with a stellar M/L = 2.6 under the maximum disc assumption.

A25 UGC 08320

UGC 08320 is a well-studied dwarf irregular system at a distance of 4.2 Mpc estimated from TRGB measurements (Tully et al. 2013). H I moment maps from processed WSRT observations were received from Adrick Broeils (Broeils 1992). The H I disc appears to be warped in both its column density contours and isovelocity contours. Following Broeils (1992), we model this warp as a change in PA. The resulting rotation curve turns over at 120 arcsec and remains flat with an estimated circular rotational velocity around 50 $\mathrm{km\,s^{-1}}$. The detailed kinematics and decompositions presented in Oh et al. (2015) and Johnson et al. (2015) result in a rotation curve that decreases after reaching its peak circular velocities, which are higher due to their lower adopted inclination angle. Despite these differences, the mass decomposition still roughly agrees with the one presented here and in Broeils (1992). No clear rotation was seen in the ionized gas velocity field from SparsePak, so a rotation curve could not be derived for the ionized gas.

A26 NGC 7793

High-resolution VLA H I observations used in the analysis were acquired from THINGS (Walter et al. 2008). NGC 7793 is late-type spiral galaxy and member of the Sculptor group at a distance of 3.7 Mpc (Radburn-Smith et al. 2011). The detailed morphology of the gas follows the star formation visible in the H α image. The stellar distribution is symmetric and regular with faint, tightly wound spiral arms. The H I kinematics are discussed in detail in de Blok et al. (2008) as well as Carignan & Puche (1990). The rotation curve derived here agrees well with both. Furthermore, the H α rotation curve in Dicaire et al. (2008) agrees with the H I kinematics. The observed decreasing circular rotational velocities at large radii are not accurately modelled in the rotation curve decomposition. A similar result was obtained for the decomposition presented in de Blok et al. (2008).

APPENDIX B: TABLES

Tables B1–B3 provide observed, extinction and distance corrected, and radial properties of galaxies in this work. Imaging parameters and data sources for the H I synthesis observations are given in Table B4. Galaxies are listed in order of increasing right ascension. All reported magnitudes are calculated using the Vega system.

Table B1. Observed properties.

Galaxy	Morphological[a] type	m_B	m_R	$m_{3.6}$	log$_{10}$(H α flux) (erg s^{-1} cm^{-2})	EW (Å)	HI flux (Jy km s^{-1})	W_{20}[b] (km s^{-1})	CO flux[c] (Jy km s^{-1})	CO flux[d] reference
NGC 3507	SBb	12.00 ± 0.02	10.83 ± 0.02	8.17 ± 0.01	– 11.77 ± 0.09	14.4 ± 0.4	13.4 ± 2.7	170	...	...
UGC 06161	SBdm	14.31 ± 0.02	13.57 ± 0.02	11.58 ± 0.05	– 12.48 ± 0.18	38.5 ± 2.6	22.2 ± 4.4	141	...	...
NGC 3718	SBa pec	11.77 ± 0.02	10.30 ± 0.02	7.39 ± 0.01	– 12.03 ± 0.12	5.16 ± 0.25	81.0 ± 16.2	492	–	1
NGC 3729	SBa pec	12.45 ± 0.02	11.13 ± 0.02	8.30 ± 0.02	– 11.87 ± 0.09	15.4 ± 0.6	6.14 ± 1.23	264	296.3 ± 125.4	2
NGC 3893	SABc	11.29 ± 0.02	10.30 ± 0.02	7.47 ± 0.01	– 11.17 ± 0.10	35.1 ± 1.5	83.0 ± 16.6	317	540 ± 100	1
NGC 3949	SAbc	11.62 ± 0.02	10.73 ± 0.02	8.09 ± 0.01	– 11.29 ± 0.12	42.6 ± 1.8	43.7 ± 8.7	300	220 ± 40	1
UGC 06900	Im	15.23 ± 0.02	14.07 ± 0.02	11.82 ± 0.05	– 13.48 ± 0.10	5.22 ± 0.28	2.03 ± 0.41	107	–	3
UGC 06917	SBm	13.39 ± 0.03	12.38 ± 0.03	10.08 ± 0.03	– 12.39 ± 0.13	15.1 ± 0.9	27.0 ± 5.4	207	–	3
UGC 06930	SABd	12.92 ± 0.02	11.97 ± 0.02	9.61 ± 0.02	– 11.99 ± 0.09	25.9 ± 1.1	42.4 ± 8.5	145	...	...
UGC 06955	IBm	14.27 ± 0.02	13.39 ± 0.02	11.27 ± 0.04	– 12.82 ± 0.13	14.2 ± 0.9	34.0 ± 6.8[e]	168[e]	...	...
IC 0749	SABcd	13.00 ± 0.02	11.93 ± 0.02	9.38 ± 0.02	– 11.87 ± 0.11	34.9 ± 1.8	10.1 ± 2.0	223	–	4
UGC 06983	SBcd	13.36 ± 0.02	12.51 ± 0.02	10.26 ± 0.03	– 12.20 ± 0.15	27.1 ± 0.2	36.5 ± 7.3	193	...	...
NGC 4068	IAm	13.38 ± 0.02	12.65 ± 0.02	10.72 ± 0.03	– 12.12 ± 0.17	34.3 ± 2.3	42.6 ± 8.5	93	–	3
NGC 4088	SABbc	11.29 ± 0.02	10.09 ± 0.02	6.99 ± 0.01	– 11.11 ± 0.11	35.8 ± 1.6	88.3 ± 17.7	373	1130 ± 200	1
NGC 4096	SABc	11.58 ± 0.02	10.40 ± 0.02	7.49 ± 0.01	– 11.39 ± 0.10	25.0 ± 1.0	73.7 ± 14.7	345	450 ± 90	1
NGC 4102	SABb	12.06 ± 0.02	10.57 ± 0.02	7.32 ± 0.01	– 11.49 ± 0.10	22.2 ± 0.9	8.51 ± 1.70	348	660 ± 150	1
NGC 4151	SABab	11.42 ± 0.02	10.14 ± 0.02	6.58 ± 0.01	– 10.83 ± 0.09	69.4 ± 3.3	57.0 ± 11.4	178	390 ± 90	1
NGC 4214	IABm	10.36 ± 0.02	9.56 ± 0.02	7.31 ± 0.01	– 10.71 ± 0.19	57.9 ± 2.5	254 ± 51	105	30 ± 6	1
NGC 4242	SABdm	11.88 ± 0.02	10.90 ± 0.02	8.66 ± 0.02	– 11.81 ± 0.16	14.0 ± 0.9	42.9 ± 8.6	138	–	5
UGC 07577	Im	13.25 ± 0.02	12.40 ± 0.02	10.41 ± 0.03	– 12.21 ± 0.04	8.55 ± 0.23	25.7 ± 5.1	58.6	...	...
NGC 4485	IBm pec	12.38 ± 0.02	11.67 ± 0.02	9.55 ± 0.02	– 11.55 ± 0.21	57.3 ± 3.6	47.0 ± 9.4	190	–	1
NGC 4490	SBd pec	10.16 ± 0.02	9.38 ± 0.02	6.86 ± 0.01	– 10.61 ± 0.26	60.1 ± 3.5	191 ± 38	271	480 ± 100	1
NGC 4618	SBm	11.36 ± 0.02	10.49 ± 0.02	8.16 ± 0.01	– 11.28 ± 0.09	35.2 ± 1.6	76.3 ± 15.3	153	45.1 ± 7.4	3
NGC 4861	SBm	12.97 ± 0.02	12.38 ± 0.02	10.48 ± 0.03	– 11.36 ± 0.13	176 ± 11	38.1 ± 7.6	124	–	6,7
UGC 08303	IABm	13.89 ± 0.02	13.14 ± 0.02	11.01 ± 0.04	– 12.16 ± 0.14	53.6 ± 3.0	32.8 ± 6.6	109	–	3
UGC 08320	IBm	13.27 ± 0.02	12.58 ± 0.02	10.72 ± 0.03	– 12.31 ± 0.10	22.5 ± 1.1	70.0 ± 14.0[e]	87.0[e]	–	3
NGC 7793	SAd	9.73 ± 0.02	8.83 ± 0.02	6.40 ± 0.01	– 10.61 ± 0.07	28.4 ± 1.3	301 ± 60	197	159.3 ± 24.3	8

Note. The apparent magnitudes are measured values using the Vega system and are not corrected for extinction. The reported apparent magnitudes and log$_{10}$(H α flux) are measured within R_{25}.

[a] RC3; de Vaucouleurs et al. (1991).

[b] Defined as the velocity width measured at 20 per cent of the peak intensity values of the H I line emission flux profile.

[c] – not detected; ... not observed.

[d] CO flux references: (1) FCRAO (Young et al. 1995); (2) Boselli, Cortese & Boquien (2014); (3) Leroy et al. (2005); (4) Braine et al. (1993); (5) Böker, Lisenfeld & Schinnerer (2003); (6) Arnault et al. (1988); (7) Cormier et al. (2014); (8) Israel, Tacconi & Baas (1995).

[e] Integrated H I flux and W_{20} values from Broeils (1992).

Table B2. Distance and extinction corrected properties.

Galaxy	$V_{\rm flat}$ (km s^{-1})	Distance (Mpc)	Distance[a] reference	A_B[b]	M_B	$(B-R)_0$	$(B$-3.6$)_0$	$(R$-3.6$)_0$
NGC 3507	225.9	42.5	1	0.089	−21.32 ± 0.02	1.13 ± 0.03	3.74 ± 0.02	2.61 ± 0.02
UGC 06161	74.5	12.0	1	0.044	−16.35 ± 0.02	0.72 ± 0.03	2.69 ± 0.05	1.96 ± 0.05
NGC 3718	250.1	36.4	1	0.051	−21.42 ± 0.02	1.45 ± 0.03	4.33 ± 0.02	2.88 ± 0.02
NGC 3729	154.3	17.6	1	0.041	−18.90 ± 0.02	1.30 ± 0.03	4.11 ± 0.03	2.81 ± 0.03
NGC 3893	184.7	18.6	1	0.077	−20.26 ± 0.02	0.96 ± 0.03	3.74 ± 0.02	2.78 ± 0.02
NGC 3949	136.3	12.0	1	0.078	−18.91 ± 0.02	0.86 ± 0.03	3.45 ± 0.02	2.59 ± 0.02
UGC 06900	68.6	9.9	1	0.077	−15.21 ± 0.02	1.13 ± 0.03	3.33 ± 0.05	2.20 ± 0.05
UGC 06917	116.1	18.2	1	0.098	−18.31 ± 0.03	0.97 ± 0.04	3.21 ± 0.04	2.24 ± 0.04
UGC 06930	92.5	8.5	1	0.108	−17.12 ± 0.02	0.91 ± 0.03	3.20 ± 0.03	2.30 ± 0.03
UGC 06955	81.4	11.0	1	0.052	−16.61 ± 0.02	0.86 ± 0.03	2.95 ± 0.04	2.09 ± 0.04
IC 0749	156.5	29.6	1	0.076	−19.58 ± 0.02	1.04 ± 0.03	3.54 ± 0.03	2.51 ± 0.03
UGC 06983	113.3	18.2	1	0.096	−18.32 ± 0.02	0.81 ± 0.03	3.00 ± 0.04	2.19 ± 0.04
NGC 4068	31.3	4.3	2	0.078	−15.12 ± 0.02	0.70 ± 0.03	2.58 ± 0.04	1.88 ± 0.04
NGC 4088	168.1	12.3	1	0.071	−19.28 ± 0.02	1.17 ± 0.03	4.23 ± 0.02	3.06 ± 0.02
NGC 4096	147.6	11.0	1	0.066	−18.80 ± 0.02	1.15 ± 0.03	4.02 ± 0.02	2.87 ± 0.02
NGC 4102	179.0	16.6	1	0.073	−19.18 ± 0.02	1.46 ± 0.03	4.67 ± 0.02	3.21 ± 0.02
NGC 4151	165.2	9.3	1	0.098	−18.80 ± 0.02	1.24 ± 0.03	4.74 ± 0.02	3.50 ± 0.02
NGC 4214	105.7	2.7	3	0.079	−16.96 ± 0.02	0.77 ± 0.03	2.97 ± 0.02	2.20 ± 0.02
NGC 4242	85.0	4.3	1	0.044	−16.60 ± 0.02	0.96 ± 0.03	3.18 ± 0.03	2.21 ± 0.03

Table B2 *continued*

Galaxy	$V_{\rm flat}$ (km s^{-1})	Distance (Mpc)	Distance^{a} reference	A_B^{b}	M_B	$(B-R)_0$	$(B\text{-}3.6)_0$	$(R\text{-}3.6)_0$
UGC 07577	21.6	2.6	4	0.074	-14.33 ± 0.02	0.82 ± 0.03	2.77 ± 0.04	1.95 ± 0.04
NGC 4485	–	8.9	5	0.078	-17.58 ± 0.02	0.68 ± 0.03	2.75 ± 0.03	2.07 ± 0.03
NGC 4490	100.1	3.2	1	0.079	-17.52 ± 0.02	0.75 ± 0.03	3.22 ± 0.02	2.47 ± 0.02
NGC 4618	107.9	6.8	1	0.077	-17.94 ± 0.02	0.84 ± 0.03	3.12 ± 0.02	2.28 ± 0.02
NGC 4861	49.5	10.0	5	0.039	-17.29 ± 0.02	0.57 ± 0.03	2.45 ± 0.04	1.88 ± 0.04
UGC 08303	61.4	5.6	1	0.065	-15.18 ± 0.02	0.72 ± 0.03	2.82 ± 0.04	2.09 ± 0.04
UGC 08320	50.5	4.2	5	0.055	-15.29 ± 0.02	0.67 ± 0.03	2.49 ± 0.04	1.83 ± 0.02
NGC 7793	113.4	3.7	6	0.070	-18.27 ± 0.02	0.87 ± 0.03	3.26 ± 0.02	2.39 ± 0.02

Galaxy	SFR^{c} (M$_\odot$ yr^{-1})	$M_{\rm star}$^{d} (10^9 M$_\odot$)	$M_{\rm H\,I}$ (10^9 M$_\odot$)	$M_{\rm H_2}$ (10^9 M$_\odot$)	$M_{\rm dyn}$^{e} (10^9 M$_\odot$)
NGC 3507	2.0 ± 0.4	106 ± 21	5.70 ± 1.14	–	293 ± 13
UGC 06161	0.03 ± 0.01	0.45 ± 0.09	0.75 ± 0.15	–	11.5 ± 0.1
NGC 3718	0.80 ± 0.22	174 ± 35	25.3 ± 5.1	–	1440 ± 11
NGC 3729	0.27 ± 0.06	16.1 ± 3.2	0.45 ± 0.09	–	31.5 ± 0.4
NGC 3893	1.5 ± 0.3	39.1 ± 7.8	6.74 ± 1.35	1.46 ± 0.27	128 ± 2
NGC 3949	0.47 ± 0.13	8.76 ± 1.75	1.47 ± 0.29	0.25 ± 0.04	40.4 ± 0.4
UGC 06900	0.002 ± 0.001	0.30 ± 0.06	0.05 ± 0.01	–	3.15 ± 0.04
UGC 06917	0.09 ± 0.03	3.97 ± 0.79	2.11 ± 0.42	–	44.3 ± 0.3
UGC 06930	0.05 ± 0.01	1.30 ± 0.26	0.72 ± 0.14	–	17.2 ± 0.3
UGC 06955	0.01 ± 0.004	0.69 ± 0.14	0.96 ± 0.19	–	16.8 ± 0.2
IC 0749	0.76 ± 0.19	17.3 ± 3.5	2.08 ± 0.42	–	57.5 ± 1.1
UGC 06983	0.13 ± 0.05	3.52 ± 0.70	2.84 ± 0.57	–	38.6 ± 0.4
NGC 4068	0.01 ± 0.004	0.15 ± 0.03	0.19 ± 0.04	–	1.35 ± 0.01
NGC 4088	0.75 ± 0.19	24.6 ± 2.9	3.15 ± 0.63	1.34 ± 0.24	104 ± 0.2
NGC 4096	0.32 ± 0.07	13.0 ± 2.6	2.12 ± 0.42	0.43 ± 0.09	64.1 ± 0.1
NGC 4102	0.58 ± 0.13	33.5 ± 6.7	0.56 ± 0.11	1.43 ± 0.33	29.1 ± 0.2
NGC 4151	0.83 ± 0.17	22.6 ± 4.5	1.17 ± 0.23	0.27 ± 0.06	69.7 ± 7.4
NGC 4214	0.09 ± 0.04	0.92 ± 0.18	0.44 ± 0.09	0.002 ± 0.0003	12.4 ± 5.8
NGC 4242	0.02 ± 0.01	0.86 ± 0.17	0.19 ± 0.04	–	5.26 ± 0.06
UGC 07577	0.003 ± 0.001	0.09 ± 0.02	0.04 ± 0.008	–	9.34 ± 0.01
NGC 4485	0.14 ± 0.07	1.35 ± 0.27	0.88 ± 0.18	–	–
NGC 4490	0.16 ± 0.10	1.91 ± 0.38	0.47 ± 0.09	0.04 ± 0.01	7.09 ± 0.16
NGC 4618	0.16 ± 0.03	2.76 ± 0.55	0.83 ± 0.17	0.02 ± 0.003	0.29 ± 0.01
NGC 4861	0.28 ± 0.08	0.88 ± 0.18	0.90 ± 0.18	–	4.92 ± 0.07
UGC 08303	0.01 ± 0.005	0.17 ± 0.03	0.24 ± 0.05	–	3.29 ± 0.08
UGC 08320	0.006 ± 0.001	0.16 ± 0.03	0.29 ± 0.06	–	2.42 ± 0.03
NGC 7793	0.22 ± 0.04	4.01 ± 0.80	0.97 ± 0.19	0.02 ± 0.003	19.4 ± 0.3

Note. M_B and colours are extinction corrected. The extinction correction for the NIR is assumed to be negligible. The M_B value also includes a small correction based on an extrapolation of the observed stellar disc. Colours are measured within R_{25}.

[a] Distance references: (1) Distances determined using the LTFR at 3.6 μm from McGaugh & Schombert (2015): $\log_{10} L_{3.6} = (-0.28 \pm 0.36) + (4.93 \pm 0.17) \log_{10} V_{\rm flat}$;(2) TRGB (Karachentsev et al. 2006); (3) TRGB (Drozdovsky et al. 2002); (4) TRGB (Dalcanton et al. 2009); (5) TRGB (Tully et al. 2013); (6) TRGB (Radburn-Smith et al. 2011).

[b] As calculated by Schlafly & Finkbeiner (2011) using the Fitzpatrick (1999) reddening law with $R_V = 3.1$.

[c] Measured within R_{25} and calculated using the calibration given in Kennicutt & Evans (2012).

[d] Calculated using M/L$_{3.6}$ (M$_\odot$/L$_\odot$) = 0.5 ± 0.1.

[e] Calculated using the last measured rotation curve point.

Table B3. Radial properties.

Galaxy	$h_{\rm R}$[a]		D_{25}[b]		$D_{\rm H\,I}$[c]		C_{28}[d]	$\log_{10}$(EW) grad	$(B-R)$ grad
	(arcsec)	(kpc)	(arcsec)	(kpc)	(arcsec)	(kpc)		(arcmin^{-1})	(arcmin^{-1})
NGC 3507	24.5	5.05	187	38.6	240	49.4	2.7	– 0.30	– 0.01
UGC 06161	24.5	1.43	132	7.66	294	17.1	3.8	– 0.92	0.04
NGC 3718	72.4	12.8	426	75.3	870	154	5.5	0.05	– 0.12
NGC 3729	21.6	1.84	176	15.0	210	17.9	2.6	– 0.82	0.13
NGC 3893	36.2	3.26	224	20.2	330	29.7	3.3	– 0.05	– 0.08
NGC 3949	18.4	1.07	158	9.16	306	17.7	3.2	– 0.55	0.25
UGC 06900	23.6	1.13	89.8	4.30	107	5.13	2.5	0.89	– 0.15
UGC 06917	33.0	2.91	191	16.9	312	27.5	3.1	0.05	– 0.21
UGC 06930	30.5	1.26	188	7.76	390	16.1	2.9	0.36	– 0.30
UGC 06955	48.3	2.57	188	9.98	396	21.0	3.3	0.12	– 0.20
IC 0749	17.7	2.54	126	18.1	162	23.3	1.7	– 0.02	– 0.12
UGC 06983	35.3	3.11	195	17.2	354	31.2	2.6	0.12	– 0.29
NGC 4068	40.4	0.84	165	3.44	330	6.88	2.9	– 0.16	0.05
NGC 4088	31.2	1.86	323	19.3	510	30.4	2.4	0.18	– 0.20
NGC 4096	46.1	2.47	388	20.8	510	27.3	3.4	– 0.05	– 0.03
NGC 4102	23.6	1.90	171	13.8	120	9.68	4.5	– 0.58	0.07
NGC 4151	57.8	2.61	235	10.6	660	29.8	5.3	– 0.30	– 0.06
NGC 4214	45.2	0.59	410	5.37	870	11.4	2.8	– 0.55	0.02
NGC 4242	54.2	1.14	283	5.95	318	6.68	2.7	0.05	– 0.05
UGC 07577	58.6	0.74	209	2.64	420	5.29	2.5	– 0.22	0.19
NGC 4485	19.3	0.68	147	5.19	–	–	2.7	1.78	0.14
NGC 4490	38.2	0.60	393	6.15	516	8.07	2.7	– 0.12	– 0.06
NGC 4618	29.2	0.96	241	7.96	540	17.8	2.3	– 0.54	0.15
NGC 4861	40.7	1.97	188	9.11	396	19.2	1.9	0.77	0.01
UGC 08303	29.3	0.80	142	3.86	264	7.18	2.7	0.63	0.09
UGC 08320	52.2	1.06	202	4.12	432	8.80	2.0	– 0.26	0.17
NGC 7793	69.2	1.24	589	10.6	825	14.8	3.1	0.10	– 0.09

Notes. [a]Total average disc scale length measured at 3.6 μm.
[b]Measured at 25 mag arcsec^{-2} in *B*.
[c]Measured at 10^{20} atoms cm^{-2}.
[d]Calculated as 5 $\log_{10}(R_{80}/R_{20})$.

Table B4. H I Synthesis image parameters.

Galaxy	Telescope; array	Project[a] code	Time on source (h)	Image weighting	Chan. sep. (km s^{-1})	Beam size (arcsec)	Beam PA (deg)	Noise (mJy beam^{-1})	Pub.[b] ref.
NGC 3507	VLA; C	AD497	1.7	Low	10.4	20.0 × 16.7	4.3	0.59	–
UGC 06161	WSRT	WHISP	12	30 arcsec smooth	4.1	32.8 × 32.0	0.0	3.1	1
NGC 3718/3729	VLA; C	AV190	26	Low	5.2	19.0 × 17.4	65.2	0.50	2
NGC 3893	WSRT	WHISP	12	30 arcsec smooth	4.1	30.0 × 30.0	0.0	3.8	1
NGC 3949	WSRT	WHISP	12	30 arcsec smooth	41.	29.9 × 29.6	0.0	2.3	1
UGC 06900	VLA; B,CnB,C,D	AH927, AH918	15	Nat	2.6	12.6 × 12.5	46.8	0.45	3
UGC 06917/06930	VLA; D	AV237	1.1	Med	5.2	48.0 × 45.3	– 73.3	1.3	–
UGC 06955	WSRT	–	24	Low	8.3	13.0 × 21.0	0.0	0.77	4
IC 0749	WSRT	–	60	High	4.1	18.0 × 12.0	0.0	1.0	5
UGC 06983	WSRT	–	24	Med	4.1	30.0 × 30.0	0.0	2.7	5
NGC 4068	VLA; C	16A-013	6.8	Low	5.0	18.7 × 16.7	43.7	0.46	6
NGC 4088	WSRT	WHISP	12	30 arcsec smooth	4.1	29.7 × 29.7	0.0	3.8	1
NGC 4096	VLA; C	16A-013	7.4	Low	5.0	20.1 × 16.6	– 75.9	0.47	6
NGC 4102	VLA; C	16A-013	6.8	Low	5.0	18.8 × 16.8	44.3	0.45	6
NGC 4151	VLA; B,C	AP251, AP104	21[c]	Taper	20.6	19.8 × 16.2	– 76.4	0.33	7
NGC 4214	VLA; B,C,D	AM418	11	Low	5.2	21.7 × 19.4	– 23.7	0.65	8
NGC 4242	WSRT	WHISP	12	30 arcsec smooth	4.1	30.9 × 30.8	0.0	4.0	9
UGC 07577	VLA, D	AH540	0.7[c]	Low	5.2	60.6 × 55.5	81.2	1.5	10
NGC 4485/4490	VLA; C,D	AA181	7.0[c]	Low	20.6	30.5 × 27.6	– 5.6	0.35	11
NGC 4618	VLA; B,C,D	AW618, AO108, AO101	38	Taper	5.2	19.7 × 18.2	84.4	0.25	12
NGC 4861	VLA; C,D	AH453, AW368	4.3, 0.7	Low[d]	2.6	22.5 × 17.2	13.5	0.91	13

Table B4 – *continued*

Galaxy	Telescope; array	Project[a] code	Time on source (h)	Image weighting	Chan. sep. (km s^{-1})	Beam size (arcsec)	Beam PA (deg)	Noise (mJy beam^{-1})	Pub.[b] ref.
UGC 08303	WSRT	WHISP	12	30 arcsec smooth	4.1	44.9 × 30.9	0.0	0.96	1
UGC 08320	WSRT	–	48	Low	2.1	14.0 × 19.0	0.0	1.1	4
NGC 7793	VLA; BnA,CnB,DnC	AW605	9.5	Nat	2.6	15.6 × 10.9	10.7	0.92	8

Note. The imaging parameters provided in this table apply to the data cube from which the H I rotation curve was derived.

[a] New observations obtained for this project have project codes 13A-107 and 16A-013.

[b] Published data references: (1) van der Hulst et al. (2001); (2) Sparke et al. (2009); (3) LITTLE THINGS (Hunter et al. 2012); (4) Broeils (1992); (5) Verheijen & Sancisi (2001); (6) Richards et al. (this work); (7) B config.: Mundell & Shone (1999); Mundell et al. (1999), C config.: Pedlar et al. (1992); (8) THINGS (Walter et al. 2008); (9) Swaters et al. (2002); (10) Hunter et al. (1998); (11) Clemens et al. (1998); (12) AW618 C config.: Bush & Wilcots (2004), AW618 B,C config.: Kaczmarek & Wilcots (2012); (13) C config.: Thuan et al. (2004), D config.: Wilcots et al. (1996).

[c] Only one polarization.

[d] C configuration data, only.

APPENDIX C: ROTATION CURVES

Fig. C1 and Table C1 present results from the tilted ring kinematic analysis of the neutral and ionized gas in 23 of the remaining 27 galaxies for which rotation curves could be derived.

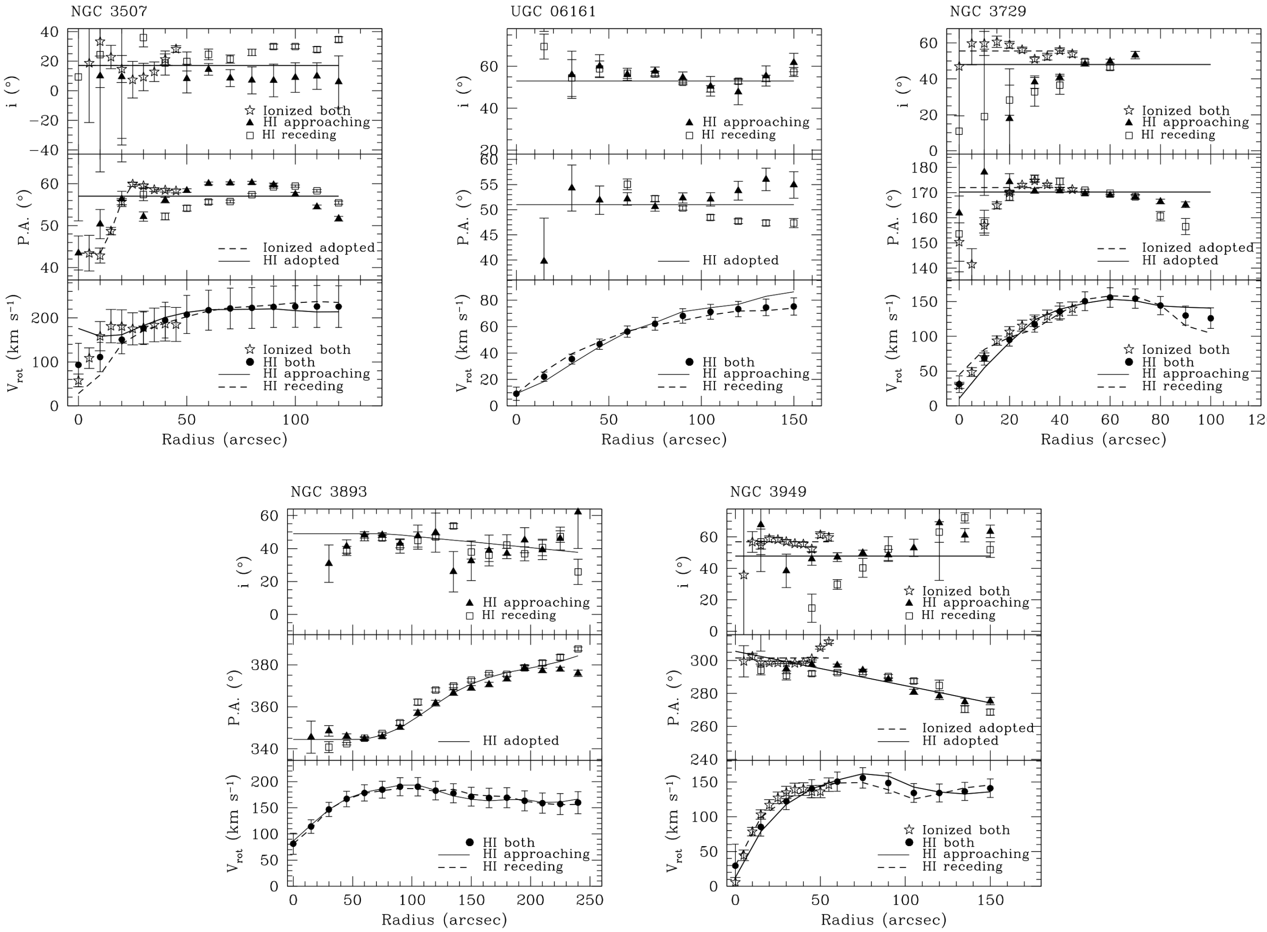

Figure C1. Neutral and ionized gas rotation curves derived from tilted rings using the GIPSY task ROTCUR. The panels for each galaxy include the inclination angle (i, top), position angle (PA, middle), and circular rotation velocity (V_{rot}, bottom). i and PA fits to the approaching (filled triangles) and receding (open squares) sides and the adopted fits to both sides (solid line) are derived from the H I velocity field. Both sides of the ionized gas velocity field are fit at the same time (open stars). The dashed line shows the adopted ionized gas fits. Circular rotational velocities for the H I (filled circles) and SparsePak ionized gas (open stars) are derived using the adopted i and PA at each radius. The solid and dashed lines show the separate circular rotational velocities derived for the approaching and receding sides of the H I velocity field, respectively, using the same adopted i and PA.

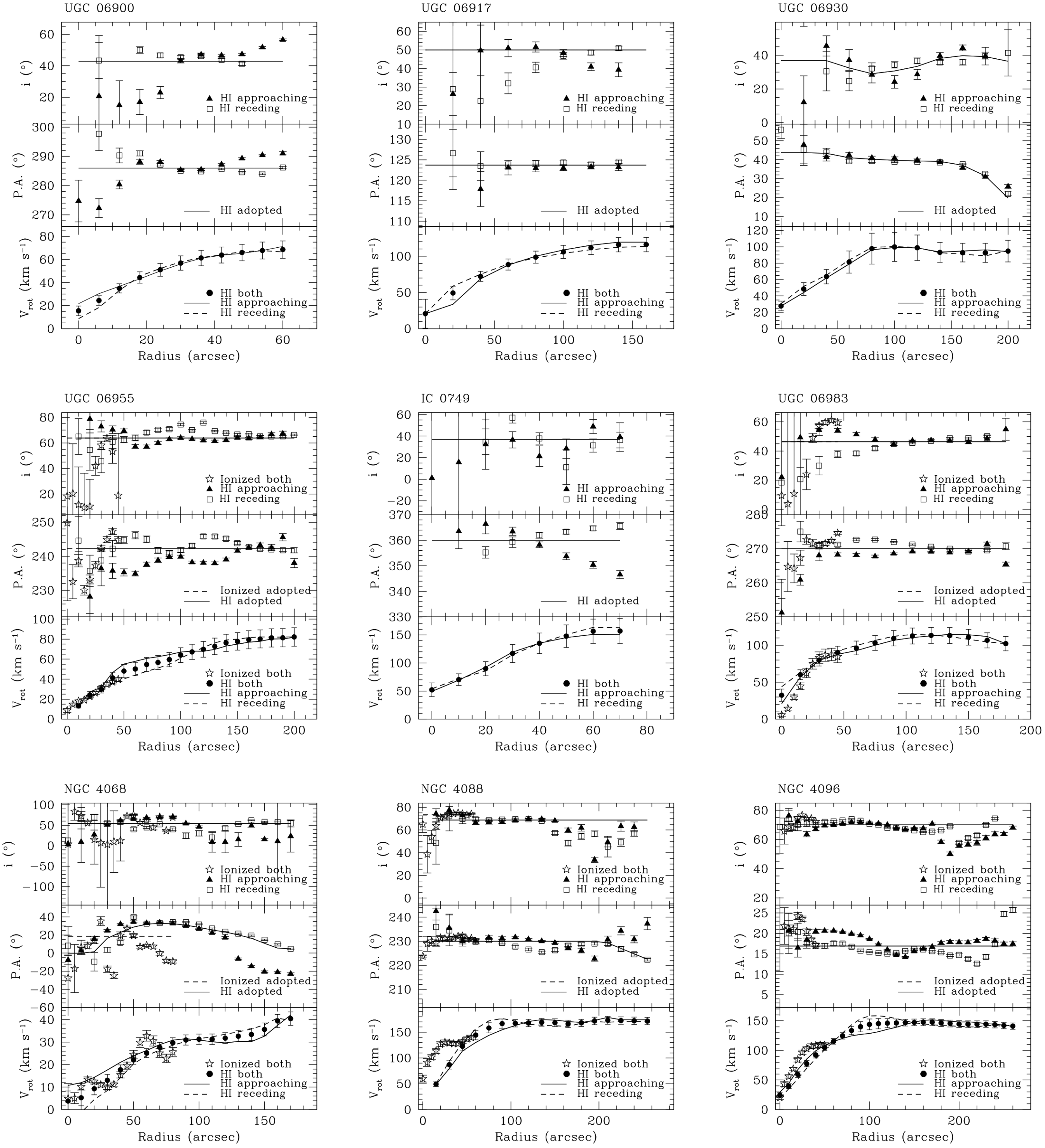

Figure C1 – *continued*

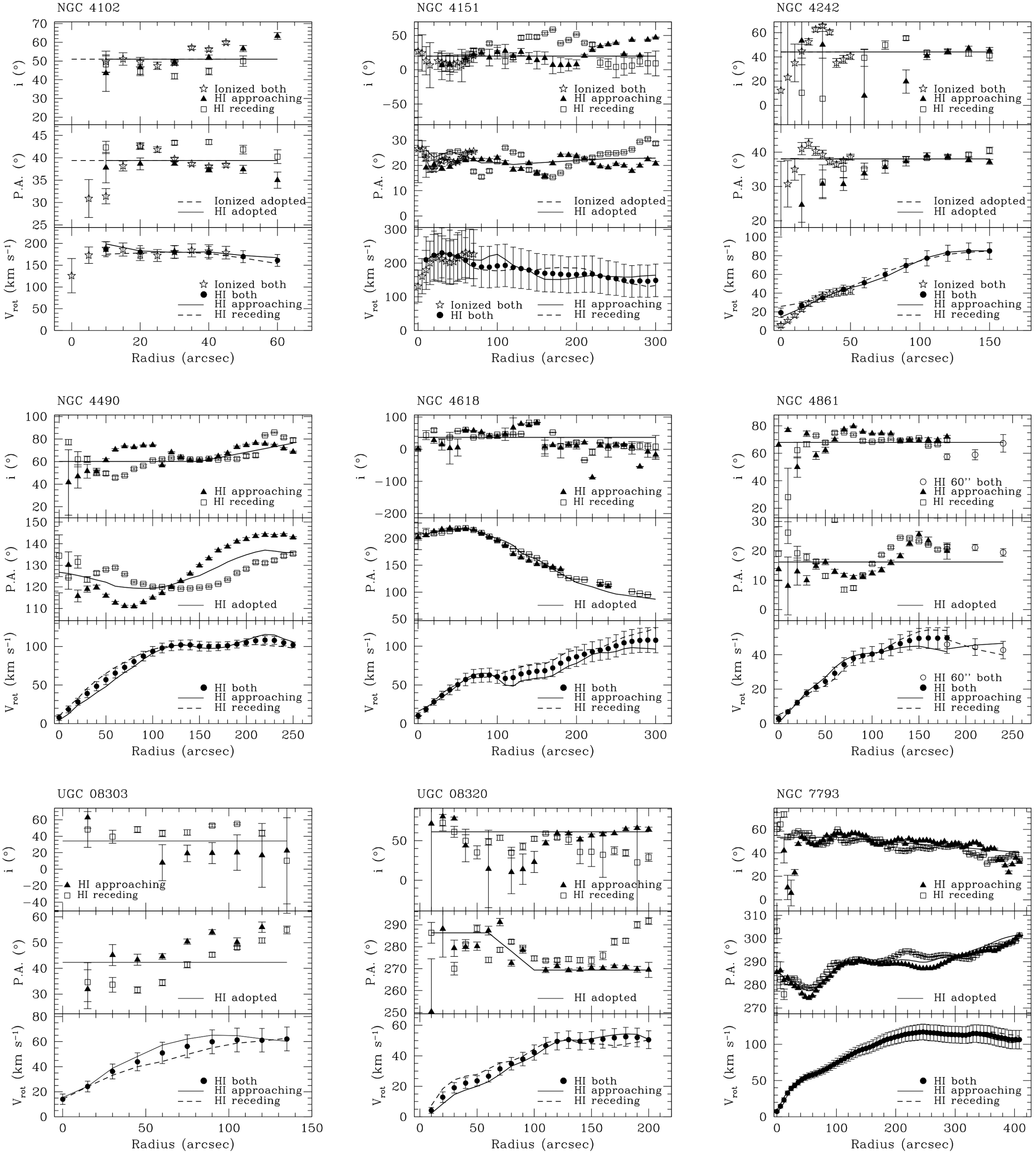

Figure C1 – *continued*

Table C1. Kinematic properties.

Galaxy	Kinematic centre RA (J2000)	Kinematic centre Dec. (J2000)	Systemic velocity (km s^{-1})	Adopted[a] PA (deg)	Adopted[a] i (deg)
NGC 3507	11:03:25.4	+18:08:08	975	57.0	17.0
UGC 06161	11:06:49.0	+43:43:24	755	51.0	53.0
NGC 3729	11:33:49.2	+53:07:35	1058	170	48.0
NGC 3893	11:48:38.1	+48:42:43	967	348[b]	48.4[b]
NGC 3949	11:53:40.8	+47:51:35	802	290	47.8
UGC 06900	11:55:39.3	+31:31:11	589	286	42.8
UGC 06917	11:56:28.7	+50:25:44	912	124	50.0
UGC 06930	11:57:17.2	+49:16:56	777	38.1	35.4
UGC 06955	11:58:29.3	+38:04:32	902	242	63.8
IC 0749	11:58:33.8	+42:44:00	810	360	37.0
UGC 06983	11:59:09.3	+52:42:27	1082	270	46.4
NGC 4068	12:04:03.2	+52:35:02	204	18.5	54.6
NGC 4088	12:05:34.5	+50:32:24	761	229	68.8
NGC 4096	12:06:01.2	+47:28:43	571	16.9	70.0
NGC 4102	12:06:23.1	+52:42:41	851	39.4	51.0
NGC 4151	12:10:32.6	+39:24:21	1001	22.4	20.0
NGC 4242	12:17:29.7	+45:37:14	518	38.0	44.0
NGC 4490	12:30:37.2	+41:39:08	582	127	63.6
NGC 4618	12:41:32.9	+41:08:49	535	212[c]	36.7
NGC 4861	12:59:01.4	+34:51:40	834	16.2	68.0
UGC 08303	13:13:17.6	+36:12:44	945	42.3	34.3
UGC 08320	13:14:27.1	+45:55:30	192	276	61.2
NGC 7793	23:57:49.7	−32:35:27	227	290	48.4

Notes. [a] Average value reported when adopted value varies with radius.
[b] Average values for radii <2 arcmin.
[c] Average PA for radii <100 arcsec.

APPENDIX D: POSITION–VELOCITY DIAGRAMS

Position–velocity diagrams have been created for every galaxy in the complete EDGES kinematic sample whose rotation curve could be decomposed, with the exception of UGC 06955, NGC 4138, and UGC 08320 for which we do not have a data cube. Slices were taken along the kinematic major axis so that the H I rotation curve may be overlaid (Fig. D1). The H I derived rotation curve points plotted here represent one resolution element, whereas the tilted ring analysis and decomposition figures utilize two points per resolution element to help guide the eye (see Section 2.4). All displayed rotation curve points have been derived from the tilted ring analysis on the H I velocity field.

The derived rotation curves adequately describe the bulk rotational motion of each galaxy. However, there are a handful of cases, most notably NGC 3507, NGC 5033, UGC 08303, and NGC 5608, where effects due to resolution limitations (i.e. beam smearing) tend to underestimate the circular rotational velocities, especially in the innermost radii where the rotation curve may be steeply rising. These inner radii where the rotation curves are the most uncertain do not heavily influence the decomposition results (Section 2.4). There are a few other cases (NGC 3992, NGC 3998, and NGC 4861) where effects due to warps or other non-circular motions present in the H I velocity fields may be influencing the derived rotation curves. Care is taken to ensure that the decomposition fits are not being altered significantly by the uncertain features in these rotation curves (i.e. the down-bending at outer radii in the rotation curve of NGC 3992 that appears to underestimate the H I emission). Finally, note that the H I emission shown for NGC 3953 is from the WHISP survey and is not the same data that was used to derive the overlaid H I rotation curve. Due to the low signal to noise of the WHISP data, the H I rotation curve was derived using the approaching side only from archival VLA data that did not have a bandpass wide enough to include the full velocity range of H I emission (see Richards et al. 2016 for details).

APPENDIX E: ROTATION CURVE DECOMPOSITION PLOTS

Results of the rotation curve decomposition analysis under a fixed M/L = 0.5 ± 0.1 assumption are provided in Fig. E1 and maximal disc/bulge assumption in Fig. E2. Results for NGC 3486 and NGC 3507 and a description of the plots are given in Figs 4 and 5.

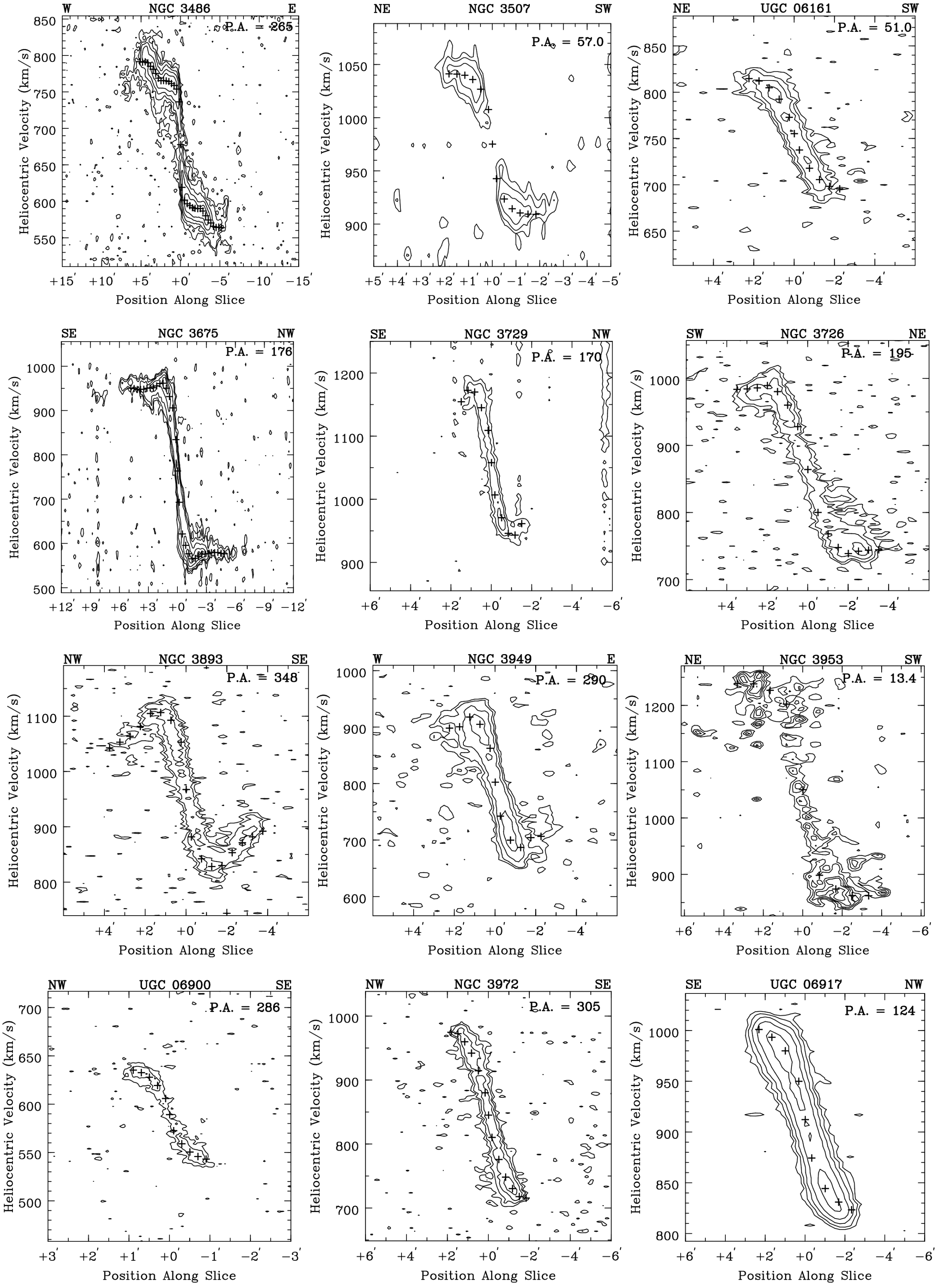

Figure D1. Position–velocity cuts along the kinematic major axis of each galaxy for which a rotation curve decomposition was carried out. H I circular rotational velocities are overlaid as crosses to verify that the derived rotation curves follow the bulk motion of the H I emission. Position–velocity diagrams were not created for UGC 06955, NGC 4138, and UGC 08320 as no data cubes were available for the data used in this analysis.

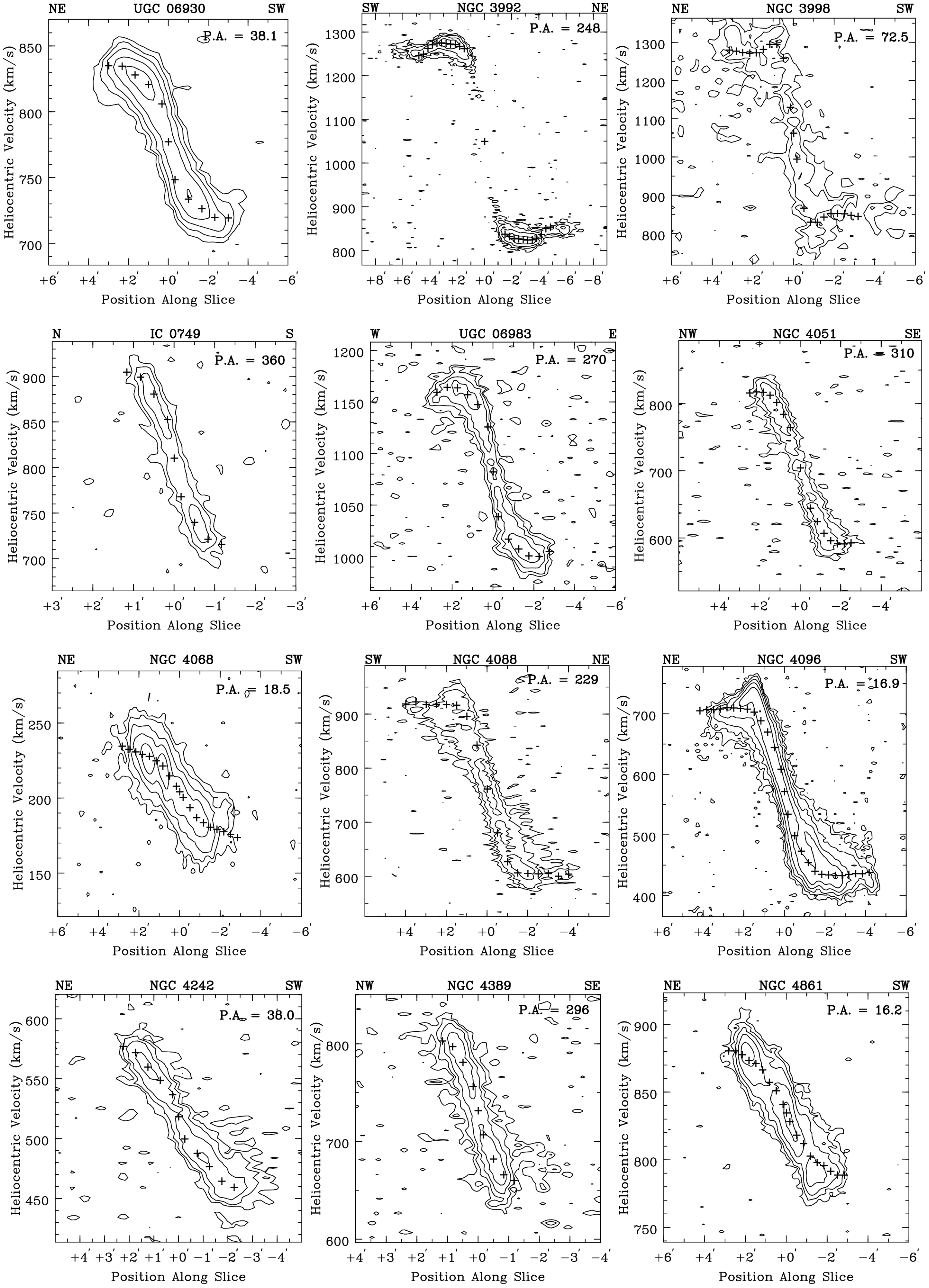

Figure D1 – *continued*

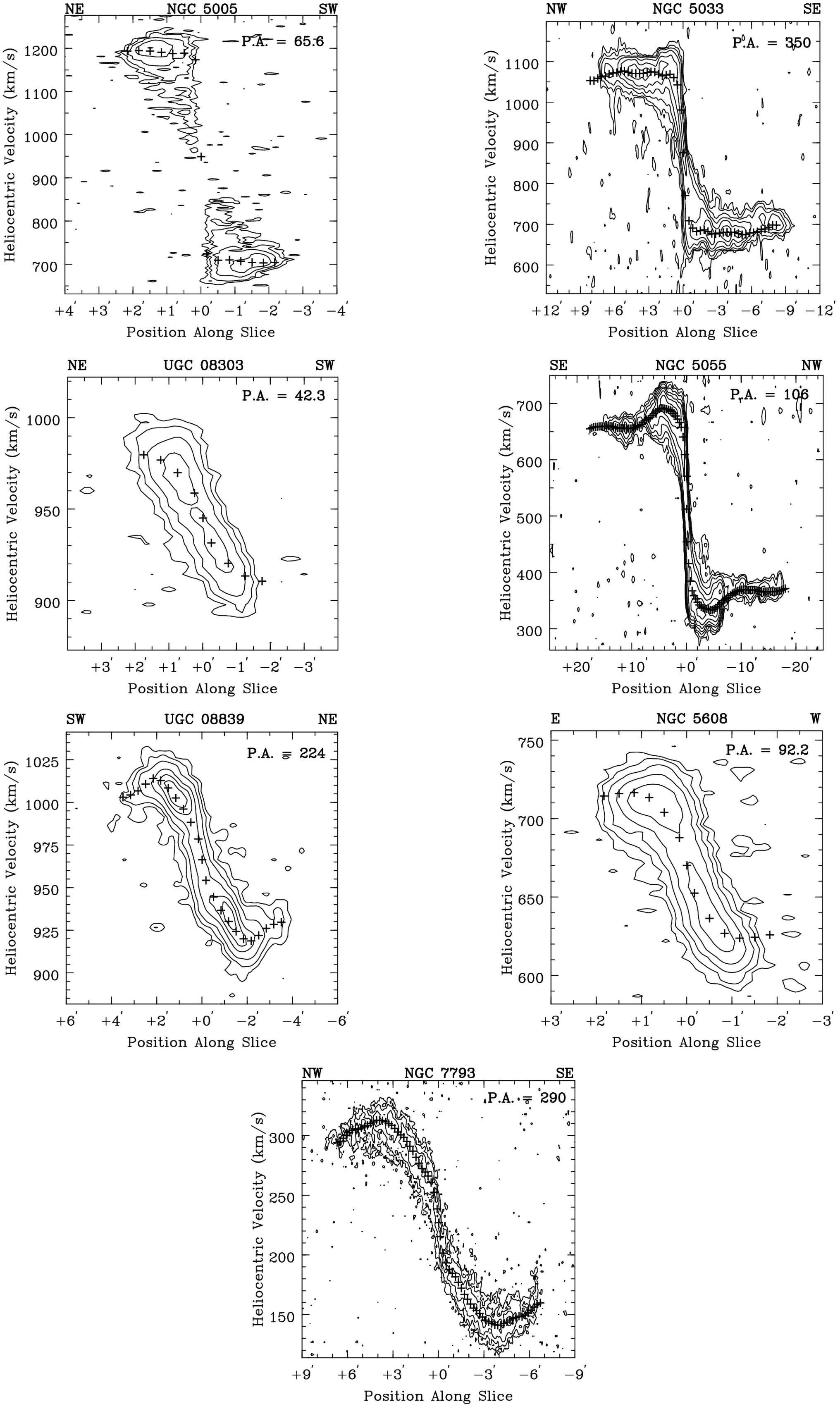

Figure D1 – *continued*

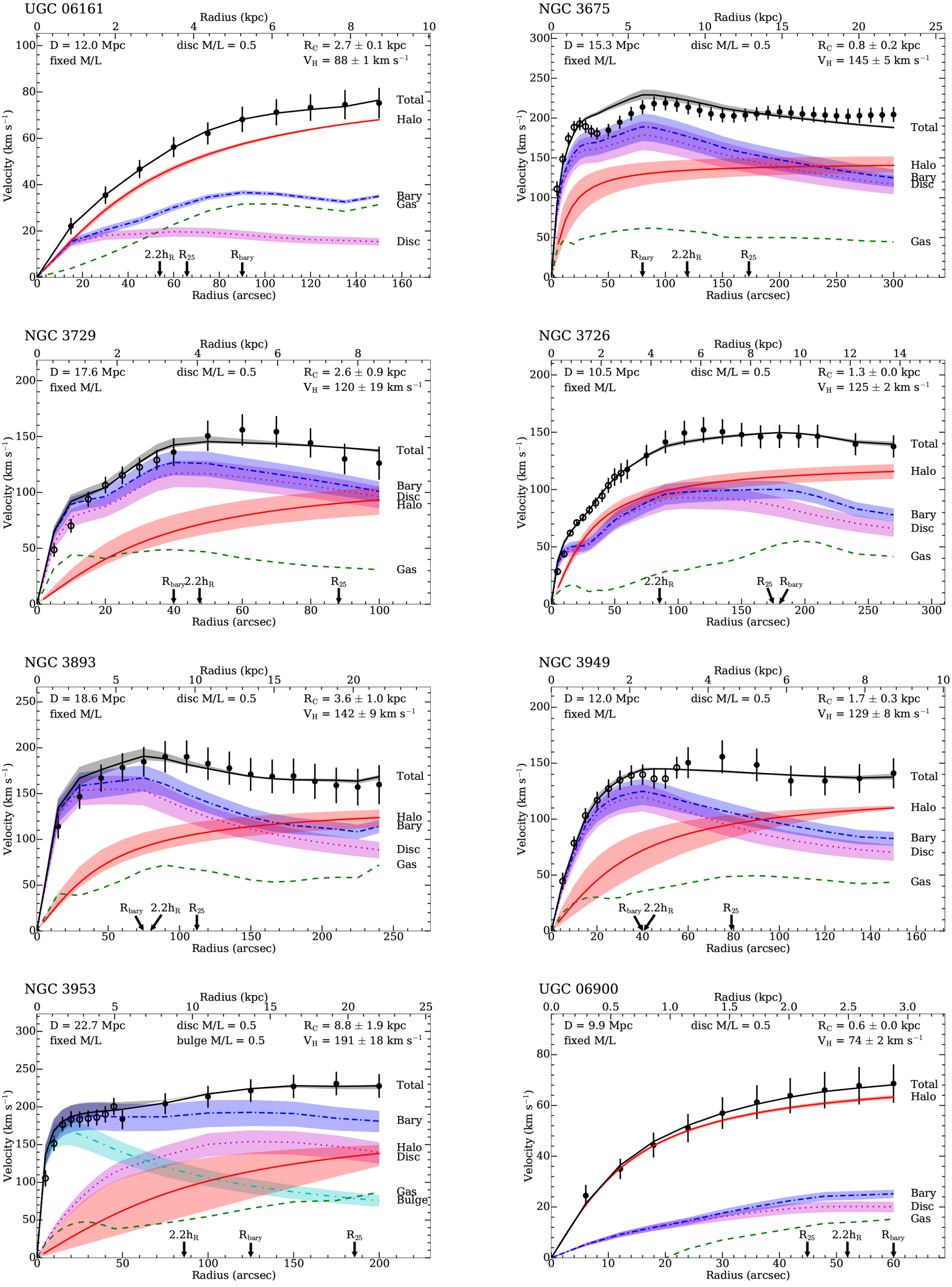

Figure E1. Rotation curve decompositions assuming a fixed stellar disc/bulge M/L = 0.5 ± 0.1 for each galaxy. See Fig. 4 for a description of plot symbols and colours.

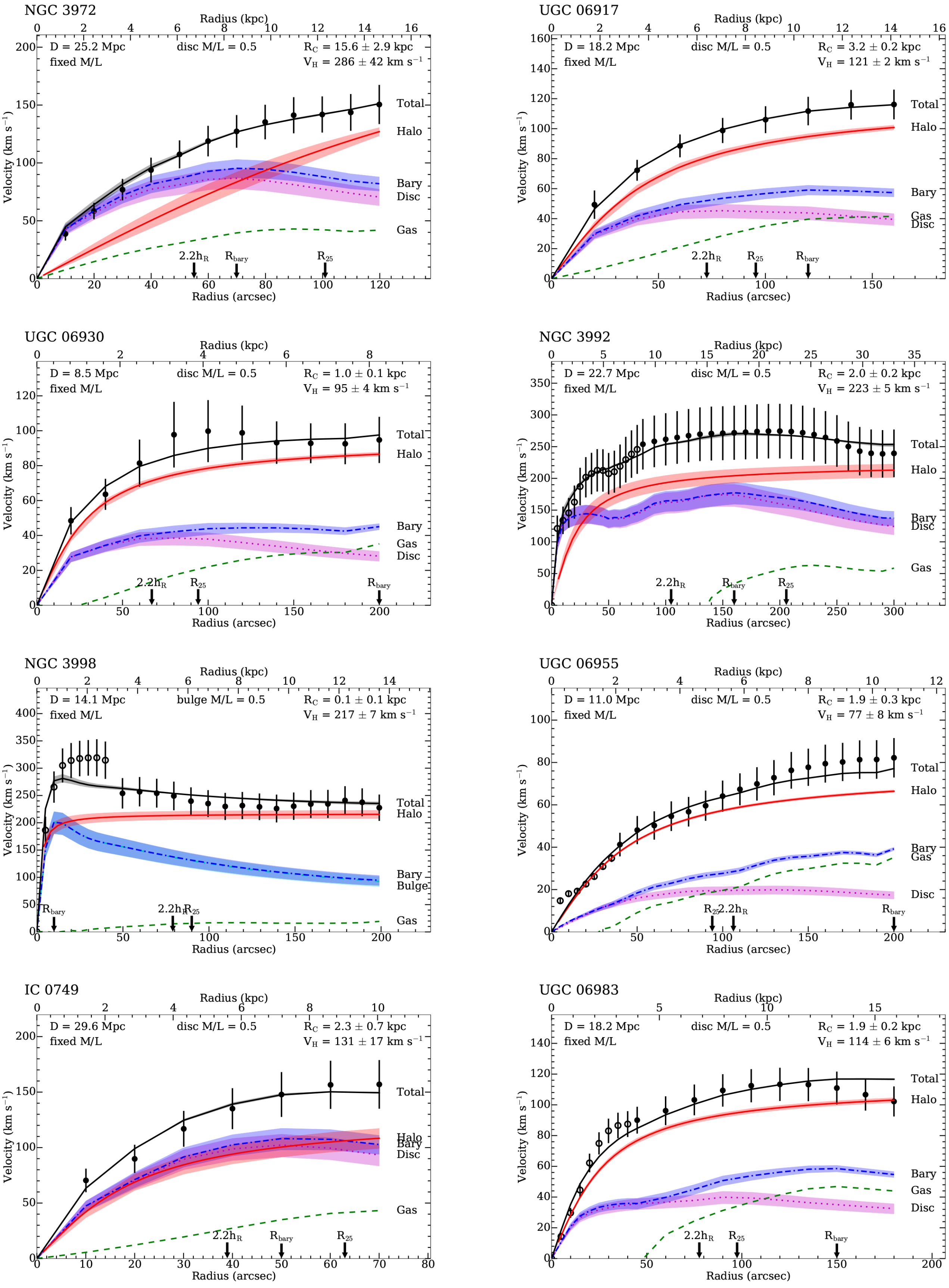

Figure E1 – *continued*

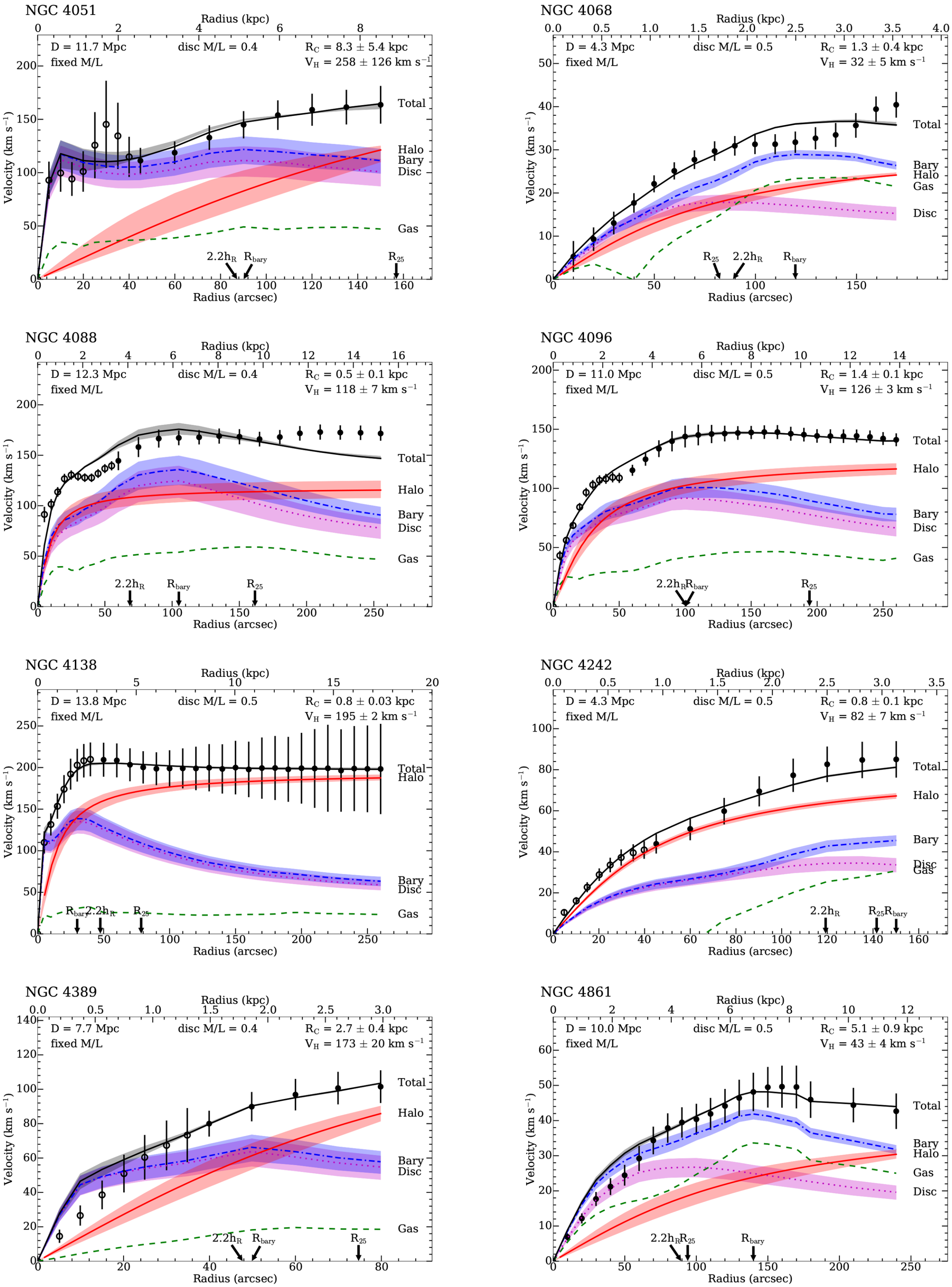

Figure E1 – *continued*

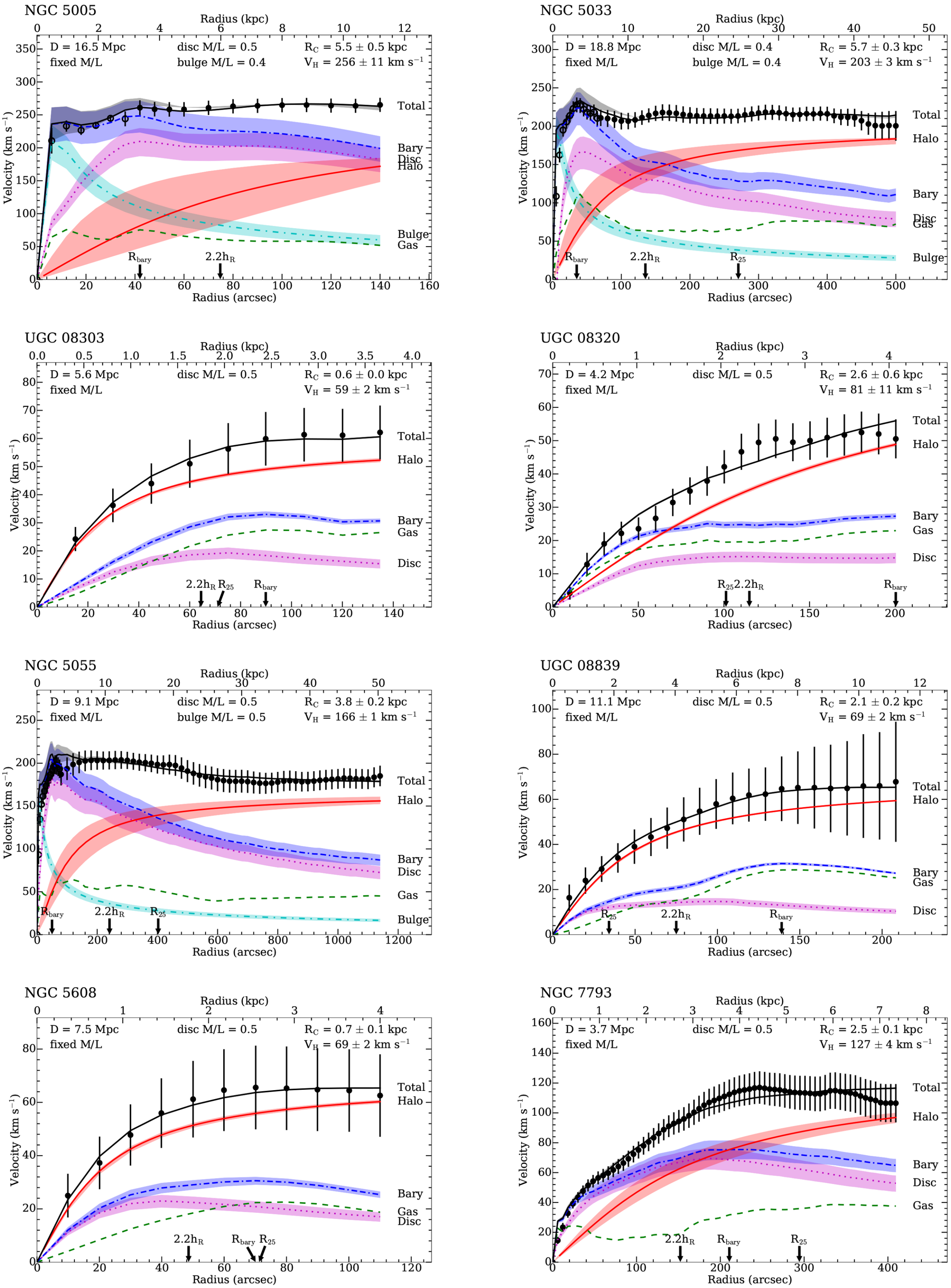

Figure E1 – *continued*

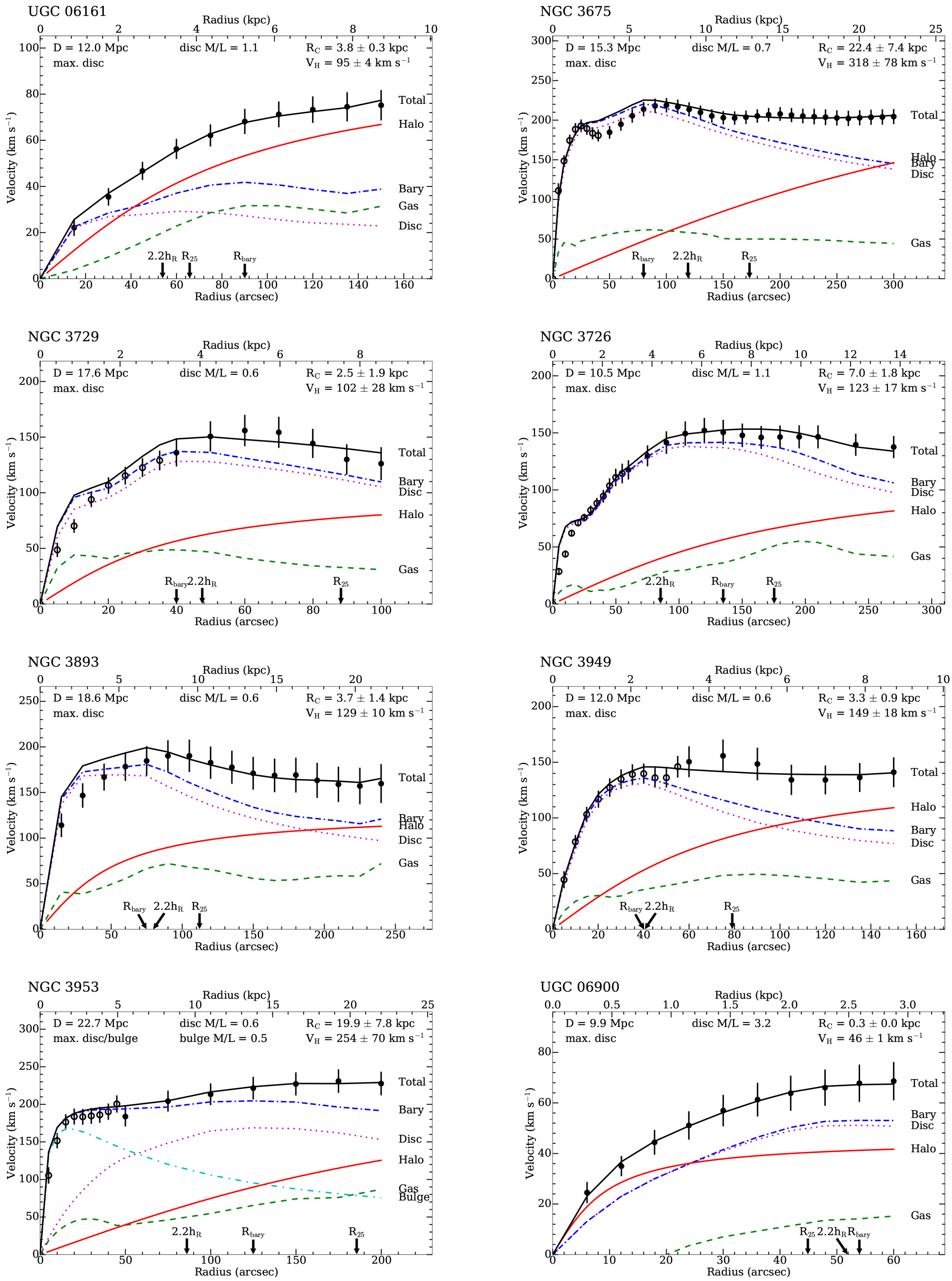

Figure E2. Rotation curve decompositions assuming the stellar disc/bulge contribute maximally to the observed inner dynamics. See Fig. 5 for a description of plot symbols and colours.

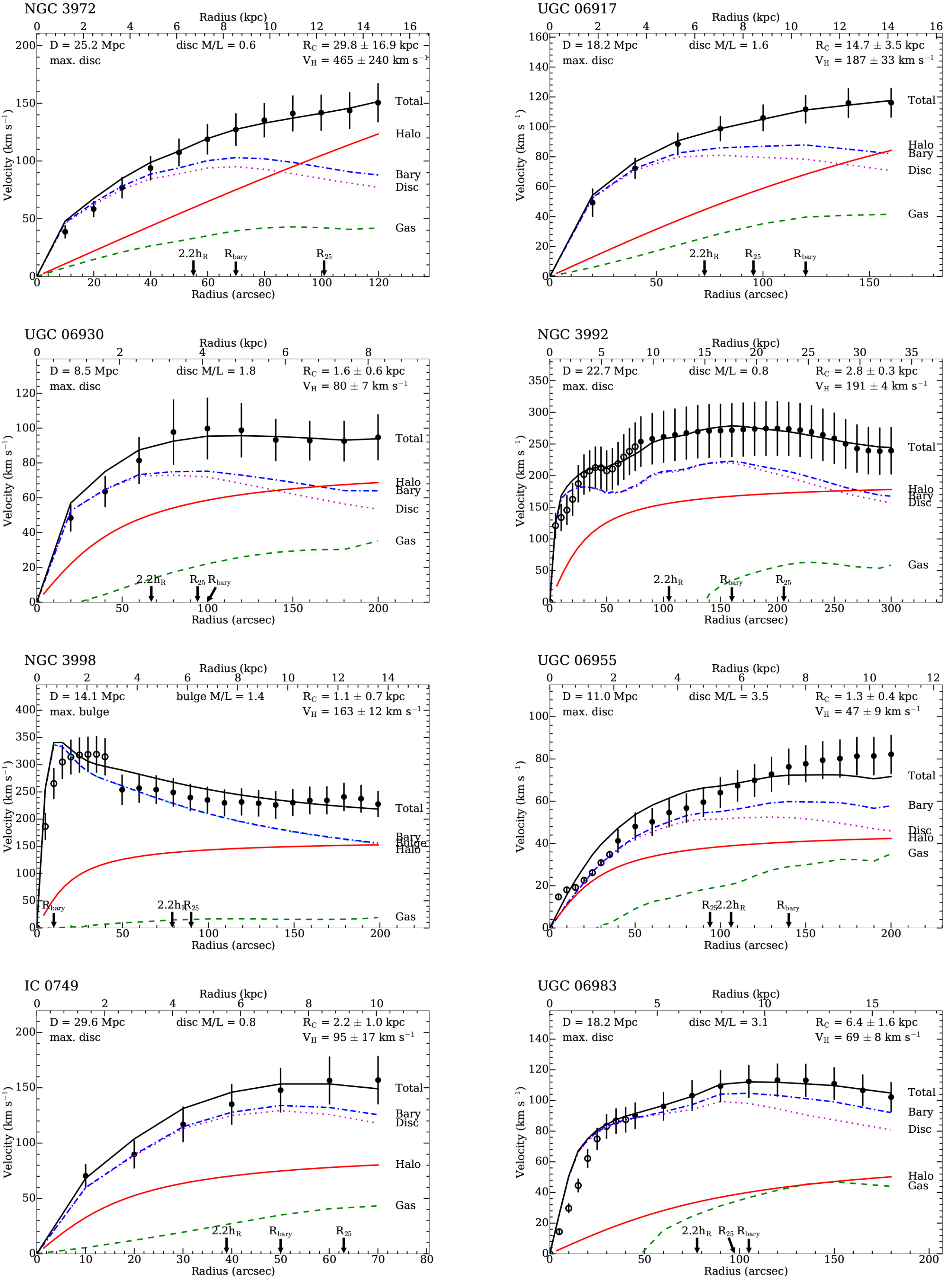

Figure E2 – *continued*

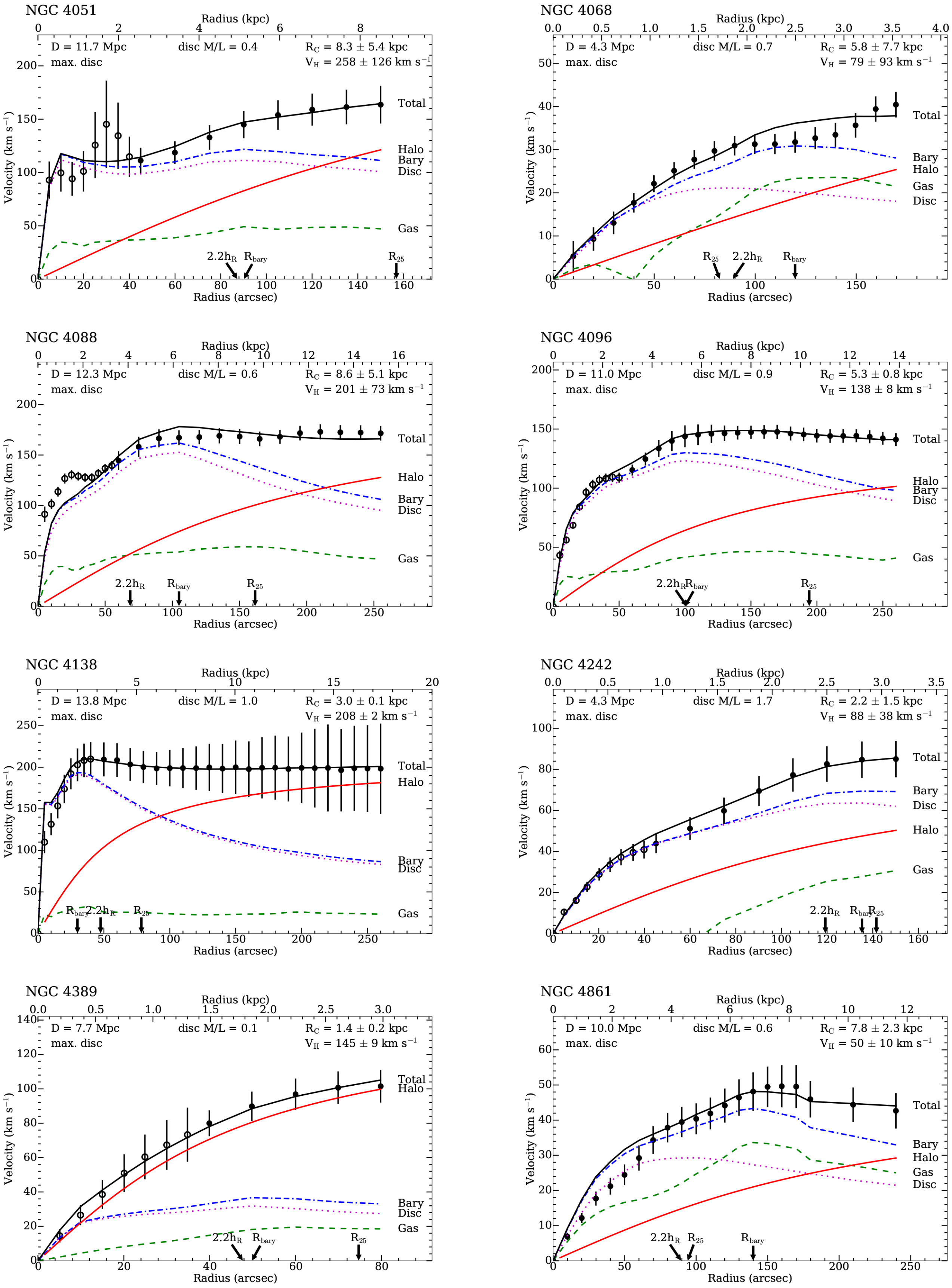

Figure E2 – *continued*

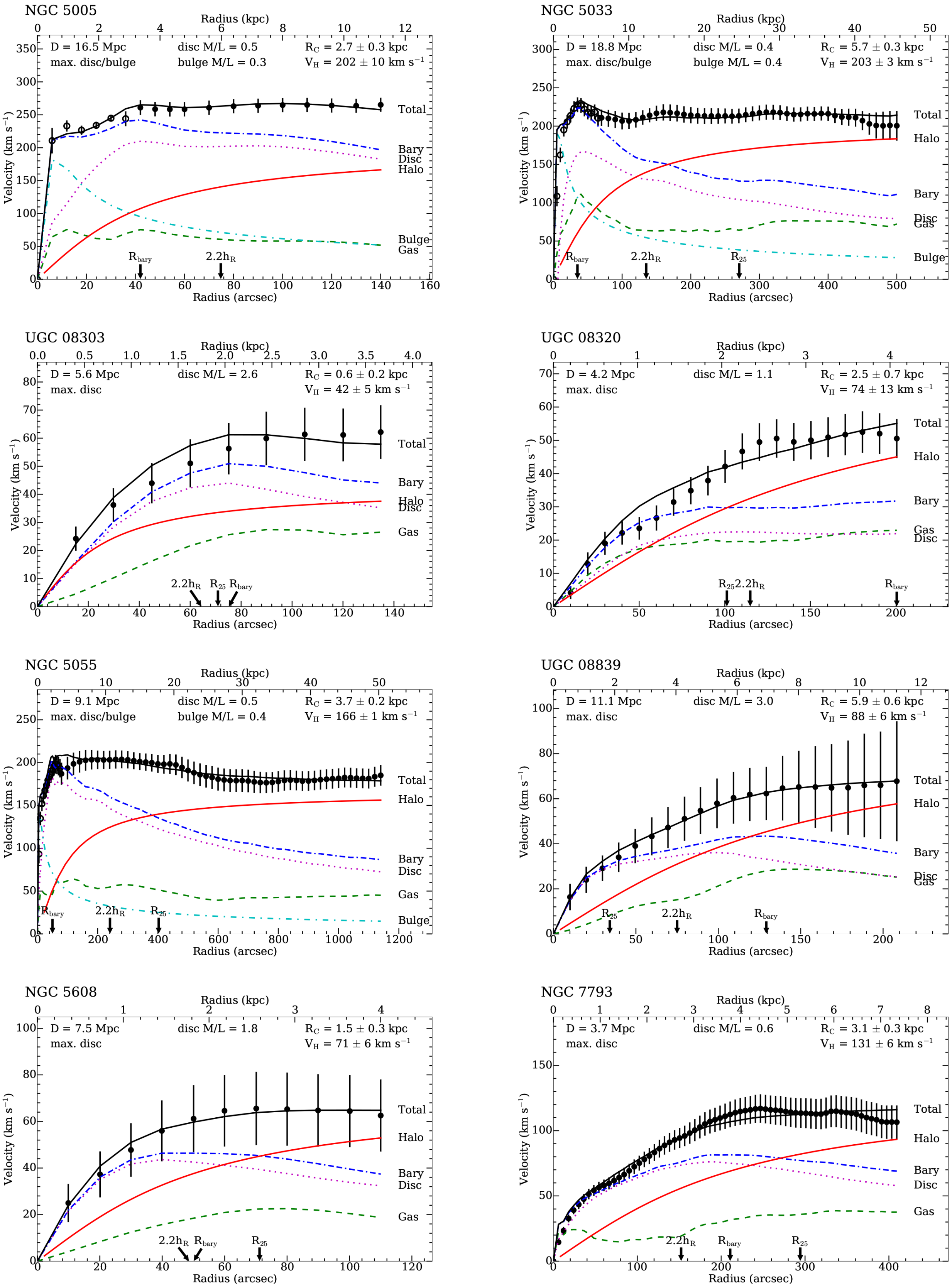

Figure E2 – *continued*

This paper has been typeset from a TEX/LATEX file prepared by the author.